

**Carnegie Mellon University**  
CARNEGIE INSTITUTE OF TECHNOLOGY

THESIS

Submitted in Partial Fulfillment of the Requirements  
for the Degree of Doctor of Philosophy

TITLE

**WATER FLOW AND THERMAL TRANSPORT  
THROUGH CARBON NANOTUBES**

PRESENTED BY

JOHN A. THOMAS

ACCEPTED BY THE DEPARTMENT OF MECHANICAL ENGINEERING

---

ADVISOR, MAJOR PROFESSOR

DATE

---

DEPARTMENT HEAD

DATE

APPROVED BY THE COLLEGE COUNCIL

---

DEAN

DATE



# **WATER FLOW AND THERMAL TRANSPORT THROUGH CARBON NANOTUBES**

Submitted in partial fulfillment  
of the requirements for the degree of

Doctor of Philosophy

in

Mechanical Engineering

by

John A. Thomas

M.S., Mechanical Engineering, Carnegie Mellon University, 2008  
B.S., Mechanical Engineering, Penn State University, 2005

Carnegie Mellon University  
Pittsburgh, Pennsylvania

May 2010



© John A. Thomas 2010  
All Rights Reserved



## ABSTRACT

WATER FLOW AND THERMAL TRANSPORT THROUGH CARBON NANOTUBES

by

John A. Thomas

Chair: Alan McGaughey

The atomic-level mechanisms of water flow and thermal transport through carbon nanotubes (CNTs) are examined using molecular dynamics (MD) simulation. To begin, the density and distribution of water molecules inside CNTs are examined using equilibrium MD simulation. For CNTs with diameters smaller than 10 nm, surface curvature effects are found to change the average density of the confined water and reduce the energetic coupling between the water and the carbon surface. Next, the relationship between water flow rate and pressure gradient for CNTs with diameters between 0.83 nm and 4.98 nm is examined using non-equilibrium MD simulation. The flow rate enhancement, defined as the ratio of the observed flow rate to that predicted from the no-slip Poiseuille relation, is calculated for each CNT. By calculating the variation of water viscosity and slip length as a function of CNT diameter, it is found that flow through CNTs with diameters greater than 1.4 nm can be understood in the context of continuum fluid mechanics. When the CNT diameter is less than 1.4

nm, however, water molecules assemble into long-range one-dimensional structures that have neither a well-defined slip length nor a well-defined viscosity. Within this subcontinuum regime, the Poiseuille relation is not applicable and transport is instead related to the CNT-dependent inter-molecular water structure.

The thermal conductivities of empty and water-filled CNTs are then predicted using (i) a direct application of the Fourier law and (ii) an application of the spectral energy density. By using the Fourier law approach, the transition from ballistic (subcontinuum) to fully-diffusive (continuum) phonon transport thermal conductivity is observed with increasing CNT length. The interactions with water molecules are found to scatter low-frequency phonon modes, causing a 20%-35% reduction in the fully-diffusive CNT thermal conductivities. A new procedure for calculating phonon properties directly from the velocity of the atoms in a crystal using the spectral energy density is then presented. This procedure, which can be applied to any periodic or non-periodic system, is used to predict the mode-by-mode contributions to the thermal conductivity of empty and water-filled CNTs. The thermal conductivity predicted using the spectral energy density is consistent with that predicted using the Fourier law approach. The number of atoms and simulation run-time required to calculate the spectral energy density, however, are both at least one order-of-magnitude smaller.

## **ACKNOWLEDGEMENTS**

I would like to thank Jeanna, my wife and best friend, for her encouragement and support. I am blessed to have someone who shows me constant and unconditional love. Words cannot describe the amount of joy and happiness she brings into my life.

Thanks to my family for their enthusiasm and interest in my work. I am fortunate to have a mother and sister who, having navigated through Ph.D. programs of their own, were able to provide unique support and feedback throughout my graduate experience. I also appreciate my father's unwaning interest in my research progress, conference trips, and teaching experiences.

I am very grateful for support from Professor Alan McGaughey and the members of the Nanoscale Transport Phenomena Laboratory. I cannot imagine having a more encouraging advisor or more positive working environment. Special thanks to Eric Landry for all the helpful discussions and to Joe Turney for help with deriving the expressions presented in Appendix C. I would also like to thank Shelley Anna, Nadine Aubry, and Mohammad Islam for serving on my thesis committee.

Finally, I would like to thank the National Science Foundation for funding this work through their Graduate Research Fellowship Program. I am also grateful to John and Claire Bertucci for funding provided through the CIT Bertucci Graduate Fellowship.

## TABLE OF CONTENTS

<b>ABSTRACT</b> . . . . .	ii
<b>ACKNOWLEDGEMENTS</b> . . . . .	iv
<b>LIST OF TABLES</b> . . . . .	vii
<b>LIST OF FIGURES</b> . . . . .	viii
<b>NOMENCLATURE</b> . . . . .	xiii
<b>CHAPTERS</b>	
<b>I. Introduction</b> . . . . .	1
1.1 Nanoscale engineering systems . . . . .	1
1.2 Transport relations . . . . .	2
1.3 Transport carriers and modeling frameworks . . . . .	4
1.4 Carbon nanotubes . . . . .	6
1.5 Thesis overview and scope . . . . .	9
<b>II. Molecular simulation of materials</b> . . . . .	12
2.1 Motivation and overview . . . . .	12
2.2 Choosing a modeling framework . . . . .	13
2.3 Potential functions in MD simulations . . . . .	15
2.4 Calculating atomic trajectories and thermophysical properties . . . . .	18
2.5 Simulation logistics . . . . .	22
<b>III. Water molecules inside and outside carbon nanotubes</b> . . . . .	26
3.1 Introduction and motivation . . . . .	26
3.2 Molecular dynamics simulations set-up . . . . .	28
3.3 Water density . . . . .	33
3.4 Water molecule distribution . . . . .	36
3.5 Water molecule orientation . . . . .	38
3.6 Summary and conclusion . . . . .	40
<b>IV. Continuum water flow in carbon nanotubes</b> . . . . .	42
4.1 Introduction . . . . .	42
4.2 Pressure-driven liquid flow . . . . .	43
4.3 Experimental measurements . . . . .	46
4.4 Data collection . . . . .	49
4.5 Viscosity and slip length predictions . . . . .	52

4.6 Comparisons to the Poiseuille relation . . . . .	58
4.7 Comparisons to experiment . . . . .	60
4.8 Conclusion and outlook . . . . .	63
<b>V. Subcontinuum water flow in carbon nanotubes . . . . .</b>	<b>65</b>
5.1 Introduction . . . . .	65
5.2 Background . . . . .	67
5.3 Simulation set-up . . . . .	68
5.4 Flow enhancement and liquid structure . . . . .	69
5.5 Correlation between structure and flow . . . . .	74
5.6 Conclusions . . . . .	77
<b>VI. Thermal conductivity of empty and water-filled carbon nanotubes . . . . .</b>	<b>79</b>
6.1 Introduction . . . . .	79
6.2 Simulation set-up . . . . .	82
6.3 Empty CNT thermal conductivity . . . . .	85
6.4 Water-filled CNT thermal conductivity . . . . .	88
6.5 Summary . . . . .	94
<b>VII. Predicting phonon properties from the spectral energy density . . . . .</b>	<b>96</b>
7.1 Introduction . . . . .	96
7.2 Calculating the spectral energy density . . . . .	98
7.3 Validating the spectral energy density . . . . .	102
7.4 Phonon transport in water-filled CNTs . . . . .	105
7.5 Discussion and conclusions . . . . .	107
<b>VIII. Contributions and future research directions . . . . .</b>	<b>108</b>
8.1 Summary of findings and contributions . . . . .	108
8.2 Future research directions . . . . .	111
8.3 Outlook and perspective . . . . .	115
<b>APPENDICES</b>	
<b>A. The REBO potential function . . . . .</b>	<b>118</b>
<b>B. Quaternions and molecular rotation . . . . .</b>	<b>123</b>
<b>C. Spectral energy density . . . . .</b>	<b>129</b>
<b>BIBLIOGRAPHY . . . . .</b>	<b>134</b>

## LIST OF TABLES

### Table

1.1	Heat, momentum, mass, and charge transport relationships. Each flux/conjugate gradient pair are coupled through a material-specific transport coefficient. . . . .	3
4.1	Experimentally measured flow enhancements and apparent water/carbon slip lengths. The flow enhancement factor is calculated using Eq. (4.4) and the apparent slip length is calculated using Eq. (4.5). . . . .	47
4.2	Regimes of water flow through CNTs, as predicted from MD simulation. . . . .	59

## LIST OF FIGURES

### Figure

<p>1.1 Comparisons between the system length scale, <math>L</math>, the differential element length scale, <math>dL</math>, and a representative liquid carrier mean-free path, <math>\lambda</math>. When the Knudsen number (<math>\text{Kn}=\lambda/L</math>) is less than 0.1, carrier transport is considered fully-diffusive and the notion of a differential element with well-defined thermophysical properties is valid. When this condition is not satisfied, fluxes must be analyzed using statistical mechanics-based transport models. . . . .</p> <p>1.2 (a) Scanning tunneling electron microscopy image of a single-walled (15,0) zig-zag CNT. (b) Tunnelling electron microscopy image of multiwalled CNTs produced by arc-evaporation (c) Single-walled CNT bundles. Attractions between tubes and bundles are governed by van der Waals interactions. (d) Scanning electron micrograph of a CNT forest grown on a glass substrate using chemical vapor deposition. Copyright 2009 Cambridge University Press . . . . .</p> <p>1.3 Graphene with atoms labeled using the CNT <math>(n, m)</math> chirality notation. Unit vectors of the 2D lattice are also shown. Mating point <math>A</math> with point <math>B</math> by rolling along the dashed line defines the structure of a (5,5) armchair CNT. . . . .</p> <p>2.1 Domains of dynamical equations used to predict the movement of particles within a computer simulation. Revivalistic effects must be considered for particles with characteristic velocities comparable to <math>c</math>, the speed of light. Quantum mechanical effects must be considered for particles with a characteristic mass comparable to one 1 atomic mass unit (a.m.u). The MD simulations used in this work are within the classical/non-relativistic regime (shaded grey). . . . .</p> <p>2.2 (a) Structure of a the TIP5P water model, which is commonly used to model condensed-phase water at room temperature. The relative positions of the oxygen and hydrogen atoms correspond to known molecular structure data. The location and number of massless charge sites are tuned to reproduce the electrostatic interactions between molecules. (b) Typical interaction potential functions between molecules. Charged interaction are typically modeled using a Coulomb potential and interactions between neutral atoms are typically modeled using a 12-6 LJ potential. . . . .</p> <p>2.3 Example of a two-dimensional periodic system. The simulation contains five particles and eight periodic replicas of the original simulation box are labeled A to H. Particles can enter and leave each box across each of the four edges. In a three dimensional system, the central box is surrounded by 26 nearest-neighbor replicas and particles can cross any of the six cubic faces. The truncation radius, <math>R_t</math>, for Particle 3 is illustrated. Only interactions with Particle 4, which is within the truncation radius of Particle 3, will be used to calculate <math>\mathbf{F}_3</math>. When using a nearest-image convention (see text), the truncation radius must be less than half of the simulation cell length, <math>L</math>. . . . .</p>	<p>5</p> <p>7</p> <p>8</p> <p>14</p> <p>17</p> <p>24</p>
--	--

3.1	Intermolecular force versus oxygen separation distance between two water molecules in an equilibrated simulation of 512 molecules at a temperature of 298 K and a pressure of 1 atm. The gray envelope represents the range of forces predicted at each separation distance. The solid line is the mean force at each distance. Inset: Force envelope and mean force at separation distances greater than 0.7 nm. At these separations, the force envelope decays as $1/(r_{\text{oo}})^4$ , characteristic of a permanent dipole-permanent dipole interaction. The mean effective force is related to the oxygen-oxygen LJ interactions and decays as $1/(r_{\text{oo}})^7$ . Copyright 2008 American Institute of Physics. . . . .	30
3.2	(a) Cropped axial snapshot of 2.8 nm CNT in water. Full simulation cell side length is 7.5 nm. The layering scheme used to analyze water near and within the CNT is also shown. Each layer has a thickness of 0.2 nm and is identified using the midpoint radial position, $r$ . (b) Cropped axial snapshot of 1.1 nm CNT in water. Full cubic simulation cell side length is 5 nm. Both images are to the same scale and all numbers are in nm. Copyright 2008 American Institute of Physics. . . . .	32
3.3	Water density inside and outside each CNT. The density profile in the unconfined water is invariant with CNT diameter and the same as that near a flat graphene sheet. The density profile in the confined water is a function of tube diameter. The inner-most layers for the 1.1 and 2.8 nm tubes are at $r=R_c-0.3$ nm and $r=R_c-1.3$ nm. Guidelines are added to highlight the minima and maxima. Copyright 2008 American Institute of Physics. . . . .	34
3.4	(a-c) Molecular distribution at $r=R_c+0.3$ nm, $r=R_c$ , and $r=R_c-0.3$ nm for the 6.9, 2.8, and 1.1 nm CNTs. The mass distribution at $r=R_c+0.3$ nm is similar for all tubes. For the 10.4 nm CNT, this same pattern is present at both $r=R_c-0.3$ nm and $r=R_c+0.3$ nm. The distribution at $r=R_c-0.3$ nm for the 6.9, 2.8, and 1.1 nm CNTs becomes more uniform with decreasing CNT diameter. In frame (c), the detailed view identifies the circumferentially-aligned (C) and axially-aligned carbon atoms (A and A') that form the six-atom carbon honeycomb. All dimensions are in nm. Copyright 2008 American Institute of Physics. . . . .	37
3.5	(a) Orientation distribution spheres at $r=R_c+0.3$ and $r=R_c-0.3$ nm for the 6.9 nm CNT. The projected length of the unit dipole moment vector, as printed in the figure, indicates the degree of rotation out of the plane of the page. Molecules are biased towards either an axially-aligned carbon atom (A) or a circumferentially-aligned carbon atom (C), as highlighted by the orientation distribution and the three water molecules beside the sphere. (b) Orientation distribution at $r=R_c-0.3$ nm near the 2.8 nm CNT. A single preferred orientation points normal to (in or out of) the page. (c) Distribution at $r=R_c-0.3$ nm near the 1.1 nm CNT. The water molecules form a pentagonal structure, resulting in two preferred orientations pointing away from the surface. A third preferred orientation points towards the CNT surface but is unbiased towards any particular axially or circumferentially-aligned carbon atom. Copyright 2008 American Institute of Physics. . . . .	39
4.1	No-slip Poiseuille flow ( $L_s = 0$ ) and slip Poiseuille flow with $L_s = 2R$ through a tube with radius $R$ . The thick vertical lines indicate the location of the tube wall. The slip coefficient for the slip system, $L_c$ , is $\sqrt{R^2 + 2RL_s} = \sqrt{5}R$ . The flow velocity is normalized by the mean velocity corresponding to no-slip flow. . . . .	45
4.2	Axial pressure gradient inside the 2.77 nm diameter CNT. The pressure within each sub-volume is predicted using the virial expansion method. Within the sampling region, the variation in liquid density with axial position is less than 1%. Copyright 2008 American Institute of Physics. . . . .	50

4.3	Volumetric flow rate in the CNTs versus pressure gradient. Over the pressure range investigated here, $Q$ is directly proportional to $\partial P/\partial z$ . Error bars, as shown for the 2.77 nm diameter CNT, are similar for all points and the chirality vector for each CNT is listed in the legend. Copyright 2008 American Institute of Physics. . . . .	52
4.4	Flow enhancement (calculated flow rate divided by $Q_N$ ) as predicted from MD simulations. Superimposed on the simulation data is the enhancement predicted from Eq. (4.5) with $L_s=30$ nm and $\mu(d) = \mu_\infty$ , and the enhancement predicted from Eq. (4.5) using a CNT-specific slip length and viscosity. The shading indicates our 15% uncertainty in the predicted viscosity and slip length data and the error bars indicate our 15% uncertainty in the calculated flow rates. The enhancement range reported for 1.6 nm CNTs is $560 < \varepsilon < 9600$ . A point corresponding to the reported flow enhancement through 7 nm diameter CNTs would have an $\varepsilon$ value of 50000, approximately 100 times greater than the maximum value on our plot. Copyright 2008 American Institute of Physics. . . . .	53
4.5	Variation of viscosity and slip length with CNT diameter. The MD viscosity was predicted from equilibrium simulation using Eq. (4.7). The highlighted annular regions on the CNT snapshots indicate the interface area used to evaluate Eq. (4.9). The MD slip length was evaluated from the velocity profile inside each CNT and Eq. (4.2). The variation in slip length with CNT diameter is fit using Eq. (4.10) with $C=352$ nm <sup>4</sup> . The dashed horizontal line identifies $L_{s,\infty}(=30$ nm). The uncertainty in the slip length is $\pm 1$ nm, making the error bars smaller than the data points. Copyright 2008 American Institute of Physics. . . . .	55
4.6	Radial velocity profile inside 2.77 nm diameter CNT fit using both unconstrained and constrained fitting procedure. The vertical dashed line at 1.38 nm represents the CNT surface. As discussed in the text, water molecules remain 0.2 nm from the CNT surface. The standard deviation for each point is approximately 2 m/s. Based on a $\chi^2$ goodness-of-fit test, we can state with a 90% confidence interval that the data used to generate this profile is consistent with our parabolic constrained fit. This confidence interval increases to 95% for the 2.22 nm CNT and to 99% for all the larger tubes. Copyright 2008 American Institute of Physics. . . . .	57
4.7	Comparison between the enhancement predicted from non-equilibrium MD simulation, the enhancement predicted using Eq. 4.6, and the enhancement measured during experiment.	61
5.1	Snapshot from a typical flow simulation for the 0.83 nm-diameter CNT. A pressure difference between the reservoirs is established using a reflecting particle membrane and periodic boundary conditions are imposed in the flow direction. The number of molecules inside the CNT ranges from $310 \pm 5$ for the 75 nm-long 0.83 nm-diameter CNT to $3676 \pm 20$ for the 150 nm-long 1.66 nm-diameter CNT. Copyright 2009 American Physical Society. . . . .	69
5.2	(a) Water structures inside the 0.83 nm- to 1.66 nm-diameter CNTs. Carbon atoms are removed for clarity and the chirality vector for each CNT is provided. (b) Axial distribution function (ADF), structure relaxation time $\tau$ , and extent of the ADF, $L_t$ , for each CNT. (c) Distribution of $P(n, t_c)$ , the probability that $n$ molecules cross the system midplane over the characteristic flow time $t_c$ . The CNT permeability, $\alpha$ , is shown for $\Delta P/L = 4 \times 10^{14}$ Pa/m. Copyright 2009 American Physical Society. . . . .	70

5.3	(a) Relationship between average flow velocity, $\bar{v}$ , and applied pressure gradient, $\Delta P/L$ , for the 75 nm-long CNTs. A similar relationship exists for the 150 nm-long CNTs. For each data point, the standard deviation in $\bar{v}$ and $\Delta P/L$ are 0.5 m/s and $2 \times 10^{13}$ Pa/m, leading to a $\pm 25\%$ uncertainty in $\varepsilon$ . Guidelines are added to highlight the trends. (b) Semi-log plot of the variation in flow enhancement factor, $\varepsilon$ , with CNT diameter, $D$ . The dashed line between $D = 1.25$ nm and $D = 1.39$ nm delineates continuum and subcontinuum flow regimes. The line in the continuum regime is a model we developed in Chapter IV. Copyright 2009 American Physical Society. . . . .	72
6.1	Simulation set-up used to predict graphene and CNT thermal conductivities. The dashed lines identify the cross-sectional area, $A_c$ . The heat flow is introduced by transferring energy from the carbon atoms in the cold reservoir to those in the hot reservoir. The differently-colored carbon atoms are used to distinguish the reservoirs from the sample. The reservoir length, $L_R$ , is 50 nm and the atoms at the ends of the systems are frozen to prevent sublimation. Periodic boundary conditions (PBC) are applied in the graphene $y$ direction. Copyright 2010 American Physical Society. . . . .	80
6.2	Typical temperature gradient obtained from MD simulation. The thermal conductivity is obtained using Eq. (6.2). The data here correspond to the 1.36 nm-diameter CNT. The temperature gradient in this trial was $29.5 \pm 1.12$ K/ $\mu\text{m}$ (i.e., 3.8% uncertainty) and the heat flow is 15 nW. The uncertainty represents the 95% confidence interval of the linear regression. Copyright 2010 American Physical Society. . . . .	83
6.3	Variation in thermal conductivity with length for empty CNTs, water-filled CNTs, and graphene. The diameter of each CNT is given in the legend and each data set is fit to Eq. (6.3). The error bars for $k_z$ are associated with uncertainty in specifying $dT/dz$ . For points without error bars, the uncertainty in the thermal conductivity is comparable to the size of the data point. Copyright 2010 American Physical Society. . . . .	85
6.4	Variation in (a) $k_{z,\infty}$ and (b) $L_{99}$ with the inverse of diameter for empty and water-filled CNTs. The chirality vectors for each CNT are used to label the data points. We also include $k_{z,\infty}$ for empty 1.63 nm-diameter ( $1/d=0.61$ nm $^{-1}$ ) and 2.17 nm-diameter ( $1/d=0.46$ nm $^{-1}$ ) CNTs, which are predicted using a 600 nm-long CNT sample. The horizontal long-dashed lines indicate $k_{z,\infty}$ and $L_{99}$ for the flat graphene sheet ( $1/d=0$ ). The horizontal short-dashed lines indicate our estimated values for $k_{z,\infty}$ and $L_{99}$ for water/graphene systems based on analysis of the CNT density of states (see Sec. 6.4). The error bars indicate the standard error calculated from a regression analysis of Eq. (6.3). Copyright 2010 American Physical Society. . . . .	87
6.5	(a) Density of states (DOS) for the 1.10 nm-diameter empty CNT. The DOS for 0.83 nm- and 1.36 nm-diameter CNTs have similar features. (b) Vibrational spectra of water molecules inside 1.36 nm-, 1.10 nm-, and 0.83 nm-diameter CNTs. The spectra inside the 1.36 nm- and 1.10 nm-diameter CNTs are similar to what we predict for bulk water. (c) Low-frequency DOS for the carbon atoms in the empty and water-filled 1.10 nm-diameter CNT. As the magnitude of the water molecule spectrum decreases with increasing frequency, the DOS for carbon atoms in the empty and water-filled CNTs converge. Copyright 2010 American Physical Society. . . . .	92
7.1	Carbon nanotube fragment used when evaluating the phonon spectral energy density. The dashed lines identify the 32 atom unit cell used in Eq. (7.4). The chirality vector for the CNT is (8,8) and the zero-temperature nearest-neighbor atomic spacing is 1.42 Å. . . . .	99

7.2	(a) Spectral energy density for the 1.10 nm diameter CNT at $T=298$ K. The color shading indicates the magnitude of the spectral energy density for each combination of $\kappa_z$ and $\omega$ corresponding to an integration time of 1 ns. (b) Phonon dispersion relationships and mode-by-mode contributions to the empty CNT total thermal conductivity. The acoustic branches are presented as thick lines for clarity. The dashed line at 30 THz separates high-frequency optical modes from the low-frequency optical modes (see text). . . . .	100
7.3	(a) Evolution of the spectral energy density for the empty CNT at $\kappa = 0$ and $\omega = 0.564$ THz with increasing integration time. (b) Evolution of the phonon lifetime at $\kappa = 0$ and $\omega = 0.564$ THz with increasing integration time. . . . .	101
7.4	(a) Semi-log plot of the empty CNT spectral energy density along $\kappa_z=0$ for frequencies below 5 THz at $T=298$ K. The lifetime of each mode is determined by fitting each peak to Eq. (7.5). Sample fits, shown as solid red lines, and the corresponding phonon lifetimes are presented for each peak. The normal mode frequencies calculated from harmonic lattice dynamics calculations are shown as vertical dashed lines and the phonon lifetimes obtained from third-order anharmonic lattice dynamics calculations are given in parentheses. (b) Water-filled CNT spectral energy density along $\kappa_z=0$ . Interactions with water molecules decrease the phonon lifetime and introduce a small frequency shift for modes with frequencies less than 2 THz. . . . .	104
8.1	Comparison between conventional engineering design-space and nano-engineering design-space. Both design-spaces have design-constraints, which are related to the desired system functionality and cost. Within nanoscale engineering systems, the properties of materials and transport systems become geometry-dependent. This behavior increases both the dimensionality of the design-space and number of candidate materials that will satisfy the design-constraints. . . . .	115
A.1	Atomic indices and angles used in the REBO potential. . . . .	119
B.1	Local basis set (defined by $X^l$ , $Y^l$ , and $Z^l$ ) positioned within a global basis set (defined by $X^g$ , $Y^g$ , and $Z^g$ ). A transformation matrix is required to convert vectors defined in the global basis to the local basis. . . . .	124
B.2	Definition of the Euler angles. The rotation sequence is noncommutative. . . . .	126

## NOMENCLATURE

$a$	molecular index, effective molecular diameter, axial distribution function
$\mathbf{a}$	acceleration
$a_l$	length of unit cell in $l$ -direction
$\mathbf{a}_1, \mathbf{a}_2$	graphene unit cell vectors
$A, A'$	axially-aligned carbon atoms
$A_c, A_i$	total cross-sectional area, interface cross-sectional area
$b$	atomic/molecular index, sample thickness
$B$	total number of atoms in unit cell
$c$	speed of light
$c_i$	concentration of species $i$
$c_{ph}$	phonon specific heat
$C$	circumferentially-aligned carbon atom
$\mathbf{C}$	chirality vector
$d, D$	diameter
$dL$	differential element length
$\mathbf{D}, \mathbf{D}_z$	diffusion coefficient, z-component of diffusion coefficient
$e$	component of phonon polarization vector
$E$	electric potential

$f_{ij}$	force between particles $i$ and $j$
$\mathbf{F}_i$	total force on particle $i$
$\hbar$	Planck constant divided by $2\pi$
$i$	integer counter
$I$	intensity
$j$	integer counter
$\mathbf{J}_i$	mass flux
$\mathbf{J}_q$	charge flux
$k_B$	Boltzmann constant
$\mathbf{k}, k_l, k$	thermal conductivity tensor, $l$ th component of $\mathbf{k}$ , interaction constant
$l$	direction, charge-site position, atomic index
$L$	length
$L_c$	slip coefficient, fit length
$L_l$	long sample
$L_R$	reservoir length
$L_s$	slip length, short sample
$L_t$	correlation length
$L_{99}$	length required to observe fully-diffusive phonon transport
$m$	mass, chirality index
$n$	chirality index, integer counter, unit cell
$N$	total number of particles in system, total number of unit-cells in a system
$N_t$	total number of particles within sub-volume
$N_T, N_l$	total number of unit cells, number of unit-cells in the $l$ -direction
$p$	reflection probability

$P$ ,	pressure, flux probability
$\mathbf{p}$	momentum
$\Delta P, \Delta P_m$	total pressure drop, minor-loss pressure drop
$\Delta P_l, \Delta P_s$	long-sample pressure drop, short-sample pressure drop
$P_r$	mass distribution function at radius $r$
$q$	charge, heat flow, normal mode
$\mathbf{q}''$	heat flux
$Q$	actual (measured) volumetric flow rate
$Q_N$	volumetric flow rate with no-slip boundary condition
$Q_S$	volumetric flow rate with slip boundary condition
$r$	separation distance, radial position
$\mathbf{r}$	position vector
$\mathbf{r}_{ij}$	separation vectors [ $\mathbf{r}_{ij} = \mathbf{r}_i - \mathbf{r}_j$ ]
$R$	radius
$R_c$	radial position of carbon nanotube wall
$P$	pressure, mass distribution function
$t, \delta t$	time, time step
$t_c$	correlation time
$T, \bar{T}, \Delta T$	temperature, average temperature, temperature drop
$\mathbf{v}, \bar{\mathbf{v}}, v_l$	velocity vector, average velocity, $l$ th component of $\mathbf{v}$
$v_g, v_{g,z}$	phonon group velocity, $z$ -component of $v_g$
$V$	volume
$w$	sample width

## Greek symbols

$\alpha$	angle, permeability, direction
$\gamma$	hydraulic conductivity, fit phonon half-width at half-maximum
$\epsilon$	energy scale, flow enhancement factor
$\epsilon_o$	permittivity of free space
$\eta$	thermostat constant
$\theta$	angle
$\kappa, \kappa_l$	phonon wave vector, $l$ th component of $\kappa$
$\lambda$	transport carrier mean-free path
$\mu$	viscosity
$\mu_i$	viscosity in interface region
$\nu$	phonon polarization
$\rho$	density, phonon reflection coefficient
$\sigma$	electrical conductivity, length scale
$\tau$	relaxation time
$\tau_o$	integration time
$\tau_{xy}$	shear stress on $x$ face in the $y$ direction
$\phi$	potential energy function
$\Phi$	spectral energy density
$\omega$	phonon frequency
$\omega_c$	fit phonon frequency

## Subscripts

<i>co</i>	carbon-oxygen
<i>oo</i>	oxygen-oxygen
<i>res</i>	reservoir
$\infty$	bulk property or flat-sheet limit

## Abbreviations

ADF	axial distribution function
a.m.u.	atomic mass unit
BTE	Boltzmann transport equation
CNT	carbon nanotube
DFT	density functional theory
DOS	density of states
DPP	distributed polarizable potential
LD	lattice dynamics
LJ	Lennard-Jones
MD	molecular dynamics
NVT	constant number of particles, volume, and energy
NVT	constant number of particles, volume, and temperature
REBO	reactive empirical bond order
RPM	reflecting particle membrane
TIP	transferable intermolecular potential
SPC, SPC/E	simple point charge, simple point charge with Ewald sum

## CHAPTER I

### Introduction

#### 1.1 Nanoscale engineering systems

Advanced micro- and nanoscale fabrication processes, such as molecular beam epitaxy [1–3], molecular sputtering [4–6], and chemical vapor deposition [7–9], have accelerated the development of high-performance power storage, energy generation, and chemical sequestration devices [10–12]. For example, new techniques for growing silicon nanowires on battery electrodes have increased the storage capacity of lithium-ion batteries by 75% [13]. Better control over plasma sputtering and deposition processes have reduced the thickness of photo-voltaic solar cells, improving their conversion efficiency and reducing their fabrication costs [14]. New methods for growing carbon nanotube (CNT) forests and CNT membranes have led to the development of high-efficiency and high-selectivity desalination, gas storage, and chemical sequestering devices [15].

Despite these advances in fabrication technologies, robust models for predicting the flux of heat, momentum, mass, and charge through nanoscale engineering materials are not available. Continuum-based transport relations (e.g., Fourier law of heat conduction, Newton law of viscosity, etc.) can fail when applied to systems with sub-micron features [16, 17], while statistical mechanics-based models (e.g., kinetic

theory, the Debye model for solids, etc.) provide only order-of-magnitude estimates of the system behavior [18, 19]. New tools for accurately predicting and modeling nanoscale transport phenomena are therefore needed to further advance the design and performance of nanoscale engineering systems [18].

## 1.2 Transport relations

In both macroscopic and nanoscale engineering devices, transport phenomena arise because systems in a non-equilibrium state try to approach an equilibrium state [20,21]. As the name suggests, some quantity must be transported within the system to make these properties position-independent [22]. For example, if the temperature of an isolated system varies spatially, heat will flow from higher-temperature regions to lower temperature regions to establish a uniform temperature. Similarly, if the species concentrations in an isolated system are non-uniform, molecules will diffuse such that the concentrations become identical at all positions. In each of these processes, the approach towards equilibrium is spontaneous, irreversible, and can be motivated by the second law of thermodynamics [20, 23, 24].

The mathematical relations typically used to quantify heat, mass, momentum, and charge transport phenomena are presented in Table (1.1). The magnitude and direction of each flux is directly proportional to its corresponding conjugate gradient via a material-specific transport coefficient. The similarity between these transport relations means that analytical solutions and correlations developed for one form of transport can be directly applied to other forms. For example, the relations used to describe steady-state heat flux through a one-dimensional solid is analogous to those used to describe steady-state mass flux through stagnant one-dimensional fluids, and shear stress flux through liquid films.

Table 1.1: Heat, momentum, mass, and charge transport relationships. Each flux/conjugate gradient pair are coupled through a material-specific transport coefficient.

<i>Flux</i>	<i>Conjugate Gradient</i>	<i>Transport Coefficient</i>	<i>Transport Relationship</i>
Heat, $\mathbf{q}$	Temperature, $T$	Thermal conductivity, $\mathbf{k}$	$\mathbf{q} = -\mathbf{k}\nabla T$ (Fourier's Law)
Shear stress, $\tau_{xy}$	Velocity, $\mathbf{v}$	Shear viscosity, $\mu$	$\tau_{xy} = -\mu \left( \frac{\partial v_x}{\partial y} \right)$ (Newton's Law)
Mass, $\mathbf{J}_i$	Concentration, $c_i$	Diffusion coefficient, $\mathbf{D}$	$\mathbf{J}_i = -\mathbf{D}\nabla c_i$ (Fick's Law)
Charge, $\mathbf{J}_q$	Electric potential, $E$	Electrical conductivity, $\sigma$	$\mathbf{J}_q = -\sigma\nabla E$ (Ohm's Law)

The transport relationships presented in Table (1.1) are phenomenological expressions based on experimental observations. They are not derived from first-principles and do not describe the molecular mechanisms responsible for transport. Consequently, the applicability of these expressions is limited to (i) defining material- or system-level transport coefficients using measured fluxes and gradients, or (ii) using a pre-specified transport coefficient and a known gradient to predict a transport flux. Only when combined with other theoretical frameworks, such as kinetic theory, linear response theory, or finite difference techniques, do these empirical expressions become useful tools for predicting transport behavior prior to measurement and understanding the underlying transport physics. Developing such predictive tools and understanding the physical mechanisms of transport through liquids and solids is the focus of this work.

### 1.3 Transport carriers and modeling frameworks

Predicting and describing transport physics requires insight into the movement and scattering of transport carriers. Transport carriers include fluid molecules, electrons, and phonons (quantized lattice vibrations) [19]. These carriers are what move in response to spatial gradients and give rise to mass, momentum, charge, and thermal energy fluxes through a system. The carriers available for transport are directly related to the chemical composition and thermodynamic phase of the host material. For example, heat flux through crystalline solids is realized by phonons (in an electrically insulating crystal) or electrons (in an electrically conducting crystal). In an ideal gas, heat flux is realized by elastic collisions between atoms and molecules.

A key non-dimensional metric used to characterize the general nature of carrier transport is the Knudsen number [25]. The Knudsen number, as illustrated in Fig. 1.1, is defined as the ratio of the carrier mean-free path (the distance a carrier travels between scattering events) to a representative system length scale. When the Knudsen number is less than 0.1, spatial variations in mass density are negligible and carrier flux in response to spatial gradients is governed by stochastic scattering interactions with other carriers. Such fully-diffusive transport systems can therefore be treated as a *continuum* and assigned a well-defined set of thermophysical properties. Within this continuum regime, differential calculus [combined with the transport relations presented in Table (1.1)] can be used to derive the continuum-based Navier-Stokes, energy balance equations, and mass-transport equations [26, 27].

When the Knudsen number is larger than 0.1, transport becomes partially ballistic as some carriers travel directly (unimpeded) through the system without scattering with other carriers. With increasing Knudsen number, the continuum assumption

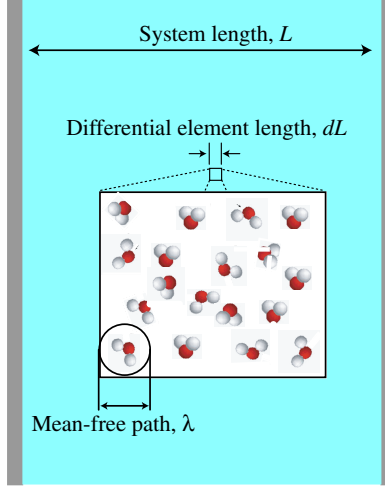


Figure 1.1: Comparisons between the system length scale,  $L$ , the differential element length scale,  $dL$ , and a representative liquid carrier mean-free path,  $\lambda$ . When the Knudsen number ( $\text{Kn} = \lambda/L$ ) is less than 0.1, carrier transport is considered fully-diffusive and the notion of a differential element with well-defined thermophysical properties is valid. When this condition is not satisfied, fluxes must be analyzed using statistical mechanics-based transport models.

becomes less valid and the role of boundary scattering on carrier transport becomes increasingly important [28]. Predictions from the continuum-based Navier-Stokes, energy balance, and mass-transport equations become less reliable and fluxes must instead be analyzed at the carrier-level using statistical mechanics-based transport models [19, 29]. Such models, which are usually based on the Boltzmann transport equation, describe fluxes in terms of non-equilibrium carrier populations and velocity distribution functions [21]. The rate at which these distributions advance towards an equilibrium state is then related to the available carrier scattering mechanisms through the Liouville theorem [30].

Since not all carriers have the same mean-free path, different carriers experience a transition from diffusive to ballistic transport at different length scales. For example, the mean-free path of water molecules in a condensed-phase liquid state is around 0.2 nm (which is comparable to the effective molecular diameter). This value suggests that a continuum description of liquid water will be valid in systems with a wetted-

diameter larger than 2 nm [31]. In smaller systems, where the Knudsen number is greater than 0.1, the effective water viscosity becomes correlated to the confined liquid structure and a subcontinuum description of transport becomes necessary [32,33]. In crystalline silicon, where the longest phonon mean-free path at room temperature is around  $1\mu\text{m}$ , a continuum-based description is valid only in samples thicker than  $10\mu\text{m}$  [34]. With decreasing system length, the role of ballistic transport and phonon scattering due to interactions with the system boundaries becomes increasingly important and the thermal conductivity becomes size dependent. Understanding the transition to ballistic transport with decreasing system-size and the nature of carrier scattering within the ballistic regime are key to predicting the transport behavior of nanoscale engineering materials.

## 1.4 Carbon nanotubes

One new class of nanoscale engineering materials that exhibit both continuum and subcontinuum transport properties are carbon nanotubes (CNTs). Carbon nanotubes, as shown in Fig. 1.2, are crystalline allotropes of carbon [35]. They can be single-walled, having a structure equivalent to that of a rolled-up graphene sheet, or multiwalled, formed from a coaxial assembly of aligned single-walled CNTs [36]. The length of a CNT typically ranges from tens of nanometers to several micrometers, although new techniques for growing CNT forests with lengths on the order of a centimeter have been developed [37]. The diameter of single-walled CNTs ranges from 1 nm to 2 nm, while the outer diameter of multiwalled CNTs is on the order of 10 nm [38].

Carbon nanotubes have a unique combination of mechanical and transport properties that make them useful in nanoscale engineering and biological systems. For

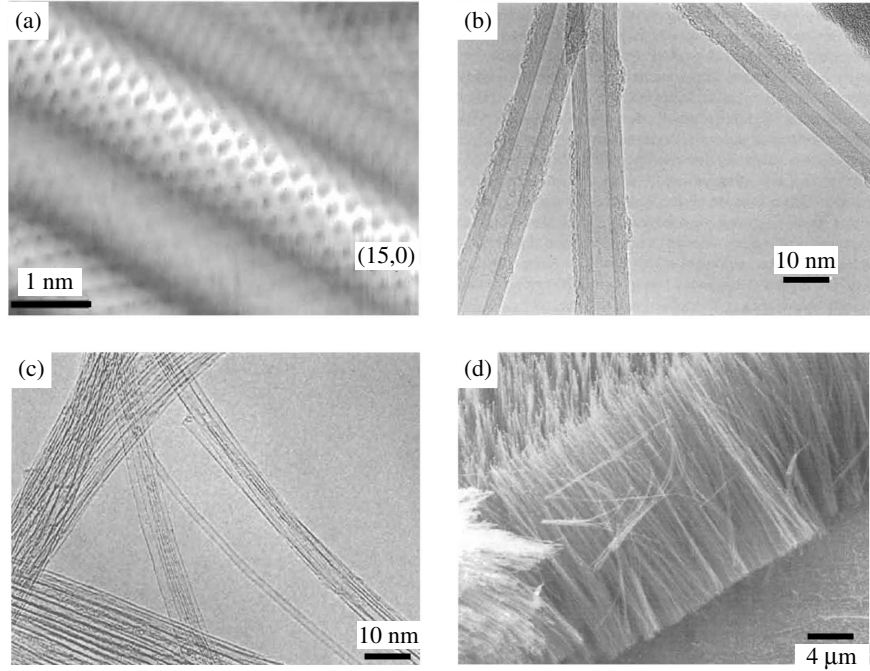


Figure 1.2: (a) Scanning tunneling microscopy image of a single-walled (15,0) zig-zag CNT. (b) Tunnelling electron microscopy image of multiwalled CNTs produced by arc-evaporation (c) Single-walled CNT bundles. Attractions between tubes and bundles are governed by van der Waals interactions. (d) Scanning electron micrograph of a CNT forest grown on a glass substrate using chemical vapor deposition. Copyright 2009 Cambridge University Press

example, open-ended CNT membranes, which are formed by filling the interstitial region of a CNT forest with non-porous matrix materials, have been proposed as next-generation desalination [39–41], gas separation [15], and gas storage devices [42]. Owing to liquid slip at the solid/liquid boundary, which arises from the non-wetting nature of the CNT surface, the measured flow rates through such CNT membranes are larger than those through other nanoporous materials with comparable flow diameters [43]. In addition to these nanofluidic applications, experimental measurements indicate that CNTs possess tunable thermal [44, 45] and electrical transport [46, 47] properties. As a result, CNT-based composites are being tested as lightweight thermal management materials [48, 49], high figure-of-merit thermoelectric devices [50, 51], and high-speed electrical connects [52, 53]. Because the dimensions (both diameter

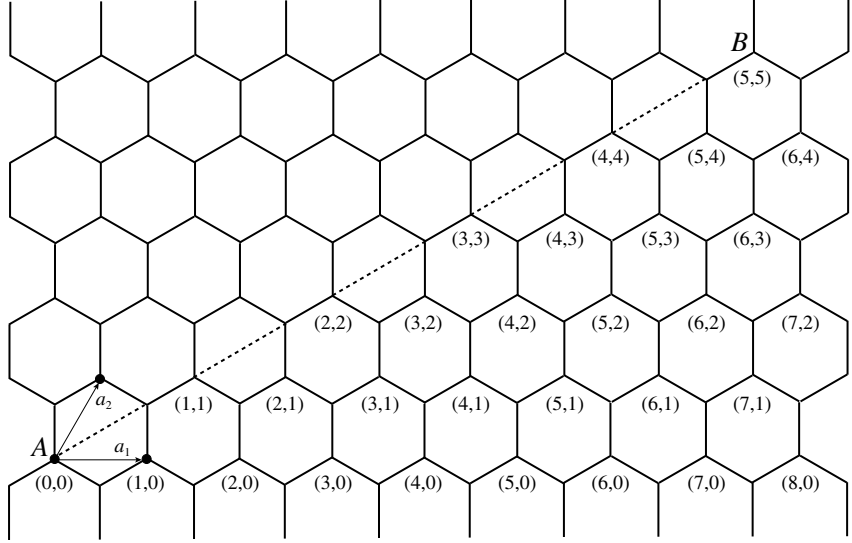


Figure 1.3: Graphene with atoms labeled using the CNT  $(n, m)$  chirality notation. Unit vectors of the 2D lattice are also shown. Mating point  $A$  with point  $B$  by rolling along the dashed line defines the structure of a  $(5,5)$  armchair CNT.

and length) of CNTs are comparable to typical carrier mean-free paths, however, the transition from diffusive to ballistic carrier flux must be considered when designing CNT-based transport systems. Moreover, due to their large surface area-to-volume ratio, the role of boundary interactions on carrier flux and scattering must be considered explicitly when predicting the transport properties of CNTs embedded within composite materials or in a fluid environment [54].

The unique continuum and subcontinuum transport properties of CNTs are related to their graphene-like structures. As shown in Fig. 1.3, the atomic structure of a single-walled CNT can be described using a chirality vector,  $\mathbf{C}$ , defined by [55]

$$\mathbf{C} = n\mathbf{a}_1 + m\mathbf{a}_2, \quad (1.1)$$

where  $\mathbf{a}_1$  and  $\mathbf{a}_2$  are the graphene unit cell vectors, and  $n$  and  $m$  are integers that define the CNT's structure. The chirality vector describes the direction that the edge of an “unrolled” single-walled CNT would map onto a flat graphene sheet. If  $m = 0$ , the CNT is classified as “zig-zag” and is electrically semi-conducting. If

$n = m$ , the CNT is classified as “armchair” and is electrically metallic (i.e., it has no electronic band gap). All other CNTs are classified as “chiral” and can be either semi-conducting or insulating depending on the combination of  $n$  and  $m$  [38]. Since the carbon atom bonding orbitals are all  $sp^2$  hybridized, the CNT structure is rigid, the phonons have large group velocities (up to 10,000 m/s), and thermal transport is dominated by lattice vibrations [56]. The uniform bond hybridization also ensures that all atoms in a defect-free CNT have zero net-charge and that the carbon surface is chemically inert [57].

Beyond CNTs, a desire to exploit the relationship between geometry and transport properties is a common theme among nanoscale engineering materials. For example, when designing nanoporous crystals for gas storage [58], high figure-of-merit nanostructured thermoelectric materials [59], and high-efficiency thin-film light-emitting diodes [60], the role of boundary interactions on carrier scattering and changes in the material-specific transport coefficients with atomic configuration must be considered. Although these systems are disparate in their form and function, new insight into subcontinuum transport phenomena in one class of materials will assist in the design and optimization of other nanoscale engineering systems.

## 1.5 Thesis overview and scope

The objectives of this work are to examine the nature of water flow and thermal transport through CNTs, and to develop a set of continuum and subcontinuum transport formulations that can be used to design and optimize CNT-based engineering devices. The primary tool used is molecular dynamics (MD) simulation, a computer simulation technique that predicts the time-evolution of the position- and momentum-space trajectories of the atoms in a system using Newtonian laws of mo-

tion. The simulation results are presented in terms of experimentally measurable transport coefficients, measurable thermophysical properties, and compared directly to existing experimental data. Although focused on transport through CNTs, the findings are generalizable to other nanoscale fluid and thermal transport systems, where boundary interactions and ballistic transport effects must be considered in device design.

This thesis is organized as follows: Chapter II begins with an introduction to atomistic modeling and MD simulation. The interatomic and intermolecular potential functions used to model the water/CNT system and the relevant simulation logistics are discussed [61]. In Chapter III, the density, distribution, and orientation of water molecules inside and outside CNTs are investigated using MD simulation [62]. As discussed in later chapters, the interaction of these water molecules with the carbon atoms has a direct effect on the nature of water flow through CNTs and thermal transport through water/CNT composite systems.

In Chapter IV, pressure-driven water flow through CNTs with diameters ranging from 1.66 nm to 4.99 nm is examined using MD simulation [63, 64]. The flow rate enhancement, defined as the ratio of the observed flow rate to that predicted from the no-slip Poiseuille relation, is calculated for each CNT. By calculating the variation of water viscosity and slip length as a function of CNT diameter, it is found that changes in the enhancement with diameter can be fully explained in the context of continuum fluid mechanics. In Chapter V, the structure and flow of water inside 75 nm- and 150 nm-long CNTs with diameters ranging from 0.83 nm to 1.66 nm are examined [65]. The transition to subcontinuum transport with decreasing diameter is identified, and the corresponding relationship between the intermolecular water structure and water flow is quantified.

In Chapter VI, the thermal conductivities of empty and water-filled single-walled CNTs with diameters between 0.83 nm and 1.36 nm are predicted in a MD simulation using a direct application of the Fourier law [66]. By examining the empty and water-filled CNT density of states, the effects of interfacial interactions on thermal transport through water/CNT composites are identified. Chapter VII continues the discussion of thermal transport and introduces a technique for predicting phonon dispersion relations and lifetimes directly from the atomic velocities in a crystal using the spectral energy density [67].

Conclusions and future research directions are presented in Chapter VIII

## CHAPTER II

### Molecular simulation of materials

#### 2.1 Motivation and overview

The very small length and time scales associated with nanoscale transport phenomena make experimental measurements of fluid flow and thermal transport through CNTs challenging. Computer-based atomic and molecular simulations, which can access these scales, have thus emerged as a complimentary tool for predicting and understanding carrier fluxes through CNTs and other nano-structured materials. [68, 69]. Within the context of investigating transport, the objectives of a computer simulation are similar to those of an experiment: (i) predict the material- or system-specific transport coefficients, (ii) validate/develop predictive transport models, and (iii) identify a transition from continuum to subcontinuum transport with decreasing system size. Although simulations can provide direct access to the underlying molecular transport mechanisms, careful consideration is required when choosing an appropriate simulation framework and validating/interperting the results. Such logistical and technical considerations are the focus of this chapter.

We begin in Sec. 2.2 with an overview of computer simulation and molecular modeling techniques. Next, in Secs. 2.3 and 2.4, we (i) introduce the intermolecular potential functions commonly used in MD simulations of water/CNT systems and (ii)

introduce techniques for integrating the molecular equations of motion. We conclude in Sec. 2.5 by discussing several technical issues related to implementing, running, and extracting data from a MD simulation.

## 2.2 Choosing a modeling framework

Three issues must be addressed prior to setting-up, running, and interpreting data from a computer simulation [70]:

1. What are the particles used to build the model system?
2. How do these particles interact and move through space?
3. What are the required number of particles and simulation runtimes?

The particles used to construct the computer model determine which types of transport carriers resolved during the simulation. For example, if atomic nuclei and electrons are used as the simulation building blocks, the dynamical behavior of molecules, phonons, and electrons can be described, but not that of protons, neutrons, or other smaller particles inside the nucleus. If atoms are chosen as the simulation building blocks, the transport behavior of molecules and phonons can be described, but not that of the electrons. If macromolecules, such as amino acids or entire CNTs are chosen as the building blocks, the overall structure and transport of whole proteins or large CNT bundles can be described, but not that of the constituent atoms, phonons, or electrons. Since fluid flow and thermal transport through CNTs are realized by fluid molecules and phonons, the models in this work must be built using atomic and/or subatomic building blocks.

The mathematical functions that describe the time-evolution of the simulation, as illustrated in Fig. 2.1, are related to the types of particles used to build the model.

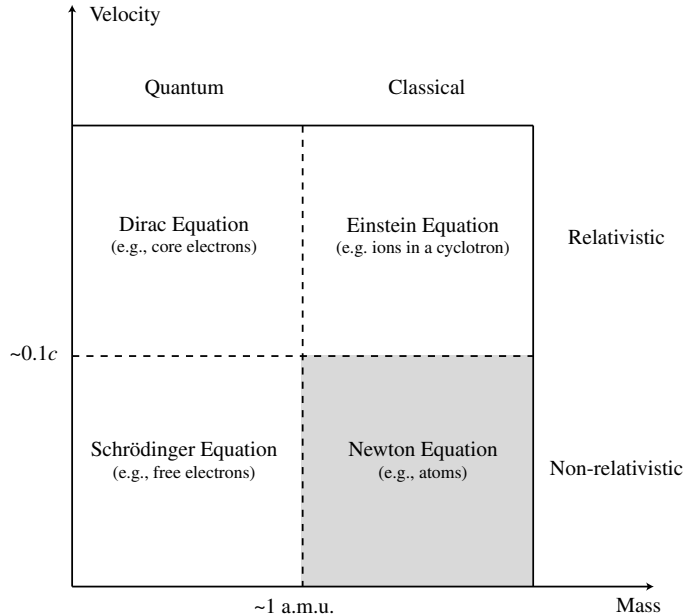


Figure 2.1: Domains of dynamical equations used to predict the movement of particles within a computer simulation. Relativistic effects must be considered for particles with characteristic velocities comparable to  $c$ , the speed of light. Quantum mechanical effects must be considered for particles with a characteristic mass comparable to one atomic mass unit (a.m.u.). The MD simulations used in this work are within the classical/non-relativistic regime (shaded grey).

For systems with subatomic building blocks, the particles are best described in terms of quantum mechanical wave functions. The corresponding interactions and dynamics must be modeled with the Dirac and Schrödinger equations, which can be used to predict the probability of a particle existing in a certain place at a certain time. For systems built with atoms or macromolecules, particle trajectories can be predicted using classical mechanics and the effective interactions between particles can be modeled using algebraic potential functions (tailored to reproduce the underlying quantum mechanical interactions).

In principle, the simulation size and run-time required to accurately predict transport phenomena from computer simulation must be sufficient to observe a statistically meaningful number of carrier scattering events. In practice, however, the simulation size and runtime are limited by the choice of building blocks and the available computational architecture. For example, using a subatomic model to investigate a

1,000 atom water/CNT system over a 10 ps tracking period requires around 10,000 processor-hours of computer time. Although these calculations are tractable within a massively-parallel computing environment, running larger and longer simulations that are more representative of bulk-like systems is computationally unfeasible. Conversely, using an atomic model to investigate the same 1,000 atom water/CNT system (over the same 10 ps tracking period) requires only one processor-hour of computer time. Thus, even on a single desktop computer, MD simulations can readily access the simulation sizes ( $\approx$ 100,000 atoms) and run-times ( $\approx$ 1 ns) required to predict carrier transport in both continuum and subcontinuum systems.

In light of the three issues itemized above, classical MD simulations is the most logical framework for investigating continuum and subcontinuum water flow and thermal transport through CNTs.

### 2.3 Potential functions in MD simulations

Within MD simulation, the correctness of the predicted transport properties is governed primarily by the accuracy with which the selected potential functions reproduce the actual quantum-mechanical interactions between atoms/molecules. Although very accurate interparticle potential functions are available in the literature, reasonable compromises between speed and accuracy must be considered when building the model. For example, the 72-parameter anisotropic site potential (ASP) water model developed by Goldman et al. [71] captures 95%-99% of the total water-water interaction energies predicted from high-level quantum mechanical calculations [72]. Although this model is suitable for investigating small water clusters (< 20 molecules), simulations of bulk-like water are computational prohibitive [73, 74]. In contrast, a very simple two-parameter Lennard-Jones (LJ) water model has been presented by

Hirschfelder et al. [75]. Although this model is applicable to simulations of high-temperature and low-density water vapors, it does not correctly predict the transport coefficients of condensed-phase water (where electrostatic interactions are important).

Most models suitable for simulating bulk-like liquid water, as shown in Fig. 2.2(a) and 2.2(b), describe interactions between molecules using a linear superposition of pairwise additive potential functions. The oxygen and hydrogen atoms are typically arranged in a bent molecular geometry with relative positions corresponding to the known gas-phase molecular structure. Various numbers of charged but massless interaction sites are then placed around the atoms to reproduce the electrostatic multipoles of the molecule. The positions of the charged interactions sites, the form of the inter-particle potential functions, and the degrees of freedom accessible to the atoms are then tuned to reproduce the underlying quantum mechanical interactions and measurable properties [76, 77]. The accuracy of these models, in terms of reproducing the quantum mechanical interaction energy at a temperature of 298 K, is usually around 90% [78]. In simple water models such as TIP3P [79], TIP4P [80], TIP5P [76], and SPC [81], the positions of the atoms and the charge sites are fixed and the molecules interact as rigid objects. This approximation is justified for simulation of liquid water at temperatures below 350 K, where the intra-atomic vibrational modes are not active. More sophisticated water models, such as Dang-Chang [82] and DPP [78], account for intra-molecular polarization through movement of the individual atoms and charge-sites. Although these models are valid over a larger range of temperatures, a computationally-intensive and iterative self-consistent field procedure must be used to evaluate the induced dipoles for each molecular configuration [82].

In water simulations containing CNTs, interactions between the water molecules and the carbon surface are typically modeled using a LJ potential function. The

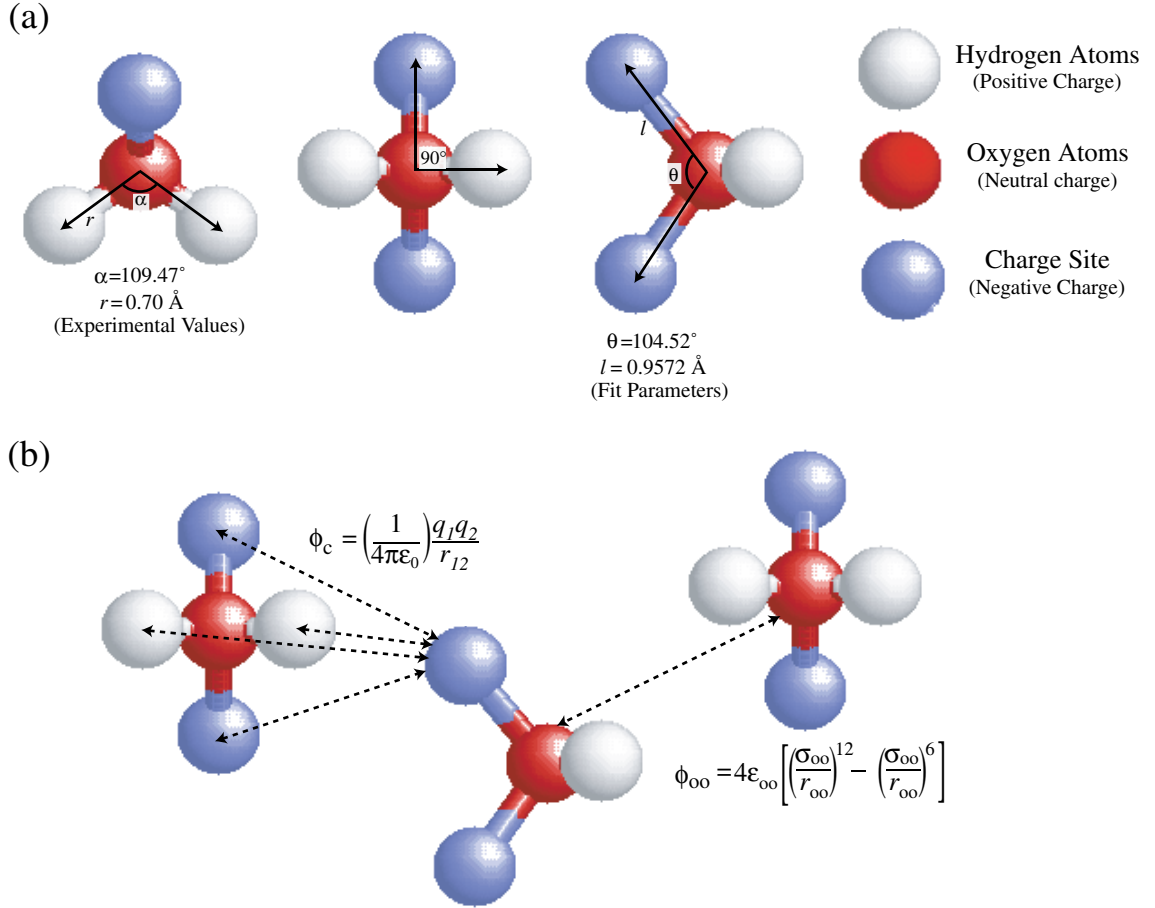


Figure 2.2: (a) Structure of the TIP5P water model, which is commonly used to model condensed-phase water at room temperature. The relative positions of the oxygen and hydrogen atoms correspond to known molecular structure data. The location and number of massless charge sites are tuned to reproduce the electrostatic interactions between molecules. (b) Typical interaction potential functions between molecules. Charged interaction are typically modeled using a Coulomb potential and interactions between neutral atoms are typically modeled using a 12-6 LJ potential.

LJ potential captures the short-range electron exchange repulsion and long-range attractive dispersion interactions between the atoms. Currently available LJ potential functions have been tuned to reproduce the experimentally-observed water/graphene contact angle [83] or data from electronic structure calculations [84]. Although the LJ potential function is sufficient to resolve the basic features of the water-carbon interaction, more sophisticated potential functions that account for (i) the polarization of the carbon atoms, and (ii) electrostatic interactions between the water molecule and the carbon atom quadrupole moment are being developed [85].

The interactions between the carbon atoms in a CNT can be modeled using a Tersoff [86] or Brenner potential function [87]. These models are multi-body functions that are tuned to reproduce the bond energies, bond lengths, and force constants of carbon-based molecules (measured from experiment or predicted from electronic structure calculations). To reduce computational costs, the carbon atoms in the majority of MD simulations of water flow through CNTs are fixed in space and a potential function is not implemented. This approximation is justified due to the high vibrational frequencies of carbon atoms in a CNT compared to those in liquid water [88]. When investigating thermal transport in empty CNTs and water/CNT composite systems, however, the dynamics of the carbon atoms must be considered [89,90].

In this work, water-water interactions are simulated using rigid and non-polarizable water models [76] and water-carbon interactions are modeled using an LJ potential [83]. In simulations of water-flow through CNTs, the carbon atoms are fixed in space and a potential function is not implemented. For investigations into thermal transport through CNTs, the interactions between carbon atoms are modeled using the Brenner REBO potential (see Appendix A) [87]. Additional information concerning the selected potential functions will be introduced as-needed throughout the text.

## 2.4 Calculating atomic trajectories and thermophysical properties

### 2.4.1 Equations of motion

Once a suitable set of MD potential functions has been specified, the inter-particle forces can be calculated and the atomic/molecular trajectories are advanced through space and time. Using Newton's laws of motion, the total force vector  $\mathbf{F}$  on particle

$i$  due to a pair potential is given by

$$\mathbf{F}_i = \sum_{j \neq i}^N \mathbf{f}_{ij} = - \sum_{j \neq i}^N \frac{\partial \phi_{ij}}{\partial \mathbf{r}_{ij}}, \quad (2.1)$$

where  $N$  is the total number of particles in the system,  $\mathbf{f}_{ij}$  is the force vector between two particles,  $\phi$  is the inter-particle potential energy function, and  $\mathbf{r}_{ij}(= \mathbf{r}_i - \mathbf{r}_j)$  is the particle separation vector. The total force on each particle is directly related to the time-derivative of the particle momentum vector,  $\mathbf{p}_i$ ,

$$\mathbf{F}_i = \frac{d\mathbf{p}_i}{dt}, \quad (2.2)$$

where  $t$  is time. If the particle mass is constant, the time derivative of the particle momentum can be written as:

$$\mathbf{F}_i = \frac{d\mathbf{p}_i}{dt} = m_i \frac{d\mathbf{v}_i}{dt} = m_i \mathbf{a}_i, \quad (2.3)$$

where  $m_i$  is the particle mass and  $\mathbf{a}_i$  is the acceleration vector. Combining Eq. (2.1) with Eq. (2.3) gives the governing equation of motion [91]:

$$-\sum_{j \neq i}^N \frac{\partial \phi_{ij}}{\partial \mathbf{r}_{ij}} = m_i \frac{\partial^2 \mathbf{r}_i}{\partial t^2}. \quad (2.4)$$

This expression, coupled with an appropriate set of initial conditions, can be used to predict the kinematic trajectories of the particles at any future time.

Equation (2.4) is typically solved using finite-difference techniques, where the molecular positions, velocities, and forces at time  $t$  are used to predict the positions and velocities at some future time  $t + \delta t$ . A large variety of finite-difference schemes, each with varying degrees of accuracy and computational speed, are available in the literature [92, 93]. In terms of MD simulation, the most attractive algorithms are those that require little read/write memory, satisfy the known conservation laws, and allow

for a large timestep. Two schemes that satisfy these conditions are the “velocity Verlet” and “Verlet leap-frog” algorithms [68]. The velocity Verlet algorithm, which is used primarily in this work, advances the trajectories from  $t$  to  $t + \delta t$  using a velocity half-step procedure:

$$\begin{aligned}\mathbf{v}_i(t + \delta t/2) &= \mathbf{v}_i(t) + \frac{\mathbf{F}_i(t)\delta t/2}{m_i} \\ \mathbf{r}_i(t + \delta t) &= \mathbf{r}_i(t) + \mathbf{v}_i(t + \delta t/2)\delta t \\ \mathbf{v}_i(t + \delta t) &= \mathbf{v}_i(t + \delta t/2) + \frac{\mathbf{F}_i(t + \delta t)\delta t/2}{m_i},\end{aligned}\quad (2.5)$$

where the forces used to advance the velocities from  $t + \delta t/2$  to  $t + \delta t$  are evaluated using the positions at  $t + \delta t$ . The Verlet algorithms are reversible in time and exhibit excellent energy conserving properties [94, 95]. Furthermore, since only the position, velocity, and force vectors need to be saved at each time step, the read/write memory requirements are quite small ( $72N$  bytes). A similar finite-difference procedure, as detailed in Appendix B, can be implemented to advance the orientations and rotational velocities of molecules in response to a net torque.

Extending the time step  $\delta t$  increases the rate at which the computer simulation advances through phase-space. An excessively large time step, however, will cause the atoms and molecules to overstep high-frequency vibrations and introduce unacceptable errors into the integrations scheme. As a general rule, the maximum time step used in the Verlet algorithms should be 10 to 20 times smaller than the lowest-period vibrations accessible to the simulation [96]. For water/CNT systems, where the highest-energy phonons have frequencies around 50 THz, this rule suggests a maximum time step of 1 fs.

### 2.4.2 Thermophysical properties

Information concerning the thermophysical properties of the system and the corresponding transport carrier scattering phenomena are obtained directly from the dynamics of the atoms and molecules within the simulation. For example, the average temperature of a collection of atoms is defined by:

$$T = \frac{1}{(3N - 3)k_B} \sum_{i=1}^N \langle m_i \mathbf{v}_i \cdot \mathbf{v}_i \rangle, \quad (2.6)$$

where  $k_B$  is the Boltzmann constant. This definition of temperature is directly related to the equipartition principle, which assigns an average energy of  $k_B T/2$  to each translational degree of freedom. The angled brackets in Eq. (2.6) denote an ensemble average, meaning the simulation temperature should be evaluated only as a time-averaged quantity for a collection atoms. The system pressure, which is also related to the particle trajectories and interactions, is defined by:

$$P = \frac{Nk_B T}{V} - \frac{1}{3V} \left\langle \sum_i^N \sum_{i>j}^N \mathbf{r}_{ij} \cdot \mathbf{f}_{ij} \right\rangle. \quad (2.7)$$

The second term in Eq. (2.7) is the virial coefficient, which accounts for non-ideal (i.e., non-elastic) interactions between atoms and molecules. Temperature and pressure, although relevant to investigations of heat transfer and fluid flow, are not the only thermophysical properties that can be extracted from the particle trajectories. Books that are replete with statistical mechanics-based and linear-response formulations for extracting thermophysical properties and transport coefficients from the dynamical characteristics of the atoms/molecules are available in the literature [35, 68, 69, 97, 98]. These procedures will be introduced in later chapters.

## 2.5 Simulation logistics

Although the basic idea of running an MD simulation and obtaining data from the atomic trajectories is straightforward, additional details concerning simulation set-up and implementation must be discussed prior to presenting simulation results. In this section, which may be ignored by readers already familiar with MD, three such logistical issues are introduced: running in different thermodynamic ensembles, incorporating a truncation radius, and applying periodic boundary conditions. Although additional implementation details will be introduced as-needed in later chapters, the ideas presented in this section provide the necessary foundation for understanding the inner-workings of the MD simulations used in this work.

- *Running in a constant-temperature ensemble*

If the total number of atoms and the volume of the simulation cell both remain constant, the atomic trajectories predicted from the Verlet algorithms will sample phase-space within the *NVE* ensemble (constant number of particles, volume, and energy). In this ensemble, the total system energy remains constant while the instantaneous system temperature fluctuates about an equilibrium value. Most experimental systems, however, are performed within the *NVT* ensemble (constant number of particles, volume, and temperature), where the system temperature remains constant and the total system energy fluctuates. Statistics within the *NVT* ensemble can be reproduced in an MD simulation by introducing a velocity damping constant,  $\eta$ , into Newton's law of motion:

$$\mathbf{F}_i = m_i \mathbf{a}_i - \eta \mathbf{v}_i. \quad (2.8)$$

The equations of motion can then be written as [68]:

$$\begin{aligned}
\mathbf{v}_i(t + \delta t/2) &= \mathbf{v}_i(t) + \frac{\{\mathbf{F}_i(t) - [\eta(t)]\} \delta t/2}{m_i} \\
\mathbf{r}_i(t + \delta t) &= \left[ 1 + \eta(t) \delta t + \frac{[\eta(t) \delta t]^2}{2} \right] \mathbf{r}_i(t) + \mathbf{v}_i(t + \delta t/2) \delta t + \frac{\mathbf{v}_i \eta(t) (\delta t)^2}{2} \\
\eta(t + \delta t) &= \eta(t) + \frac{\delta t}{\tau_{\text{res}}} \left[ \frac{T(t)}{T_{\text{res}}} \right] \\
\mathbf{v}_i(t + \delta t) &= \mathbf{v}_i(t + \delta t/2) + \frac{\mathbf{F}_i(t + \delta t) \delta t/2}{m_i [1 + \eta(t + \delta t)] \delta t/2}, 
\end{aligned} \tag{2.9}$$

where  $T_{\text{res}}$  is the desired simulation temperature,  $\tau_{\text{res}}$  is a relaxation time, and  $T(t)$  is the instantaneous system temperature. The damping constant couples the atoms and molecules in the system to a virtual constant-temperature reservoir. The temperature of this virtual reservoir is  $T_{\text{res}}$  and the strength of the coupling is related to the thermostat relaxation time. When  $\eta$  is equal to zero, meaning atoms do not interact with the reservoir, the  $NVE$  equations of motion presented in Eq. (2.5) are recovered. In an  $NVT$  ensemble, the relative root-mean-square fluctuation in total energy decreases with increasing number of particles (as  $1/\sqrt{N}$ ) [21]. Consequently, for the systems considered in this work, we find that the thermophysical properties obtained from simulations within the  $NVT$  ensemble match those obtained from simulations within the  $NVE$  ensemble.

- *Implementing a truncation radius*

Not all inter-particle interactions need to be considered when predicting the forces on each particle and integrating the equations of motion. Instead, since the magnitude of the inter-particle forces tend to decrease with increasing separation distance,  $\mathbf{F}_i$  is governed primarily by interactions with nearest neighbor particles. The weaker long-distance interactions can therefore be discounted from the force summation [Eq. (2.1)] by introducing a interaction truncation radius. As illustrated in Fig. 2.3, the truncation radius  $R$  is the radius at which the interaction force drops to zero. This radius is typically chosen to be approximately 2-3 times the size of the particles being simulated.

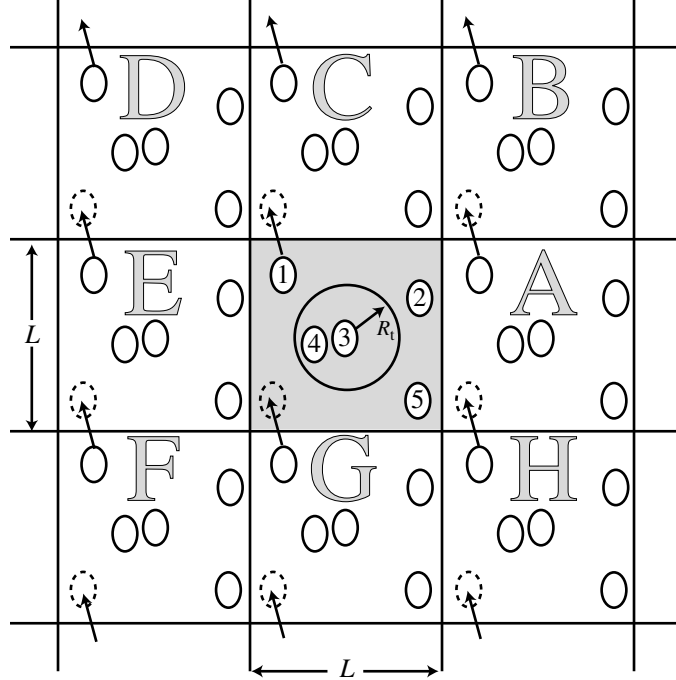


Figure 2.3: Example of a two-dimensional periodic system. The simulation contains five particles and eight periodic replicas of the original simulation box are labeled A to H. Particles can enter and leave each box across each of the four edges. In a three dimensional system, the central box is surrounded by 26 nearest-neighbor replicas and particles can cross any of the six cubic faces. The truncation radius,  $R_t$ , for Particle 3 is illustrated. Only interactions with Particle 4, which is within the truncation radius of Particle 3, will be used to calculate  $\mathbf{F}_3$ . When using a nearest-image convention (see text), the truncation radius must be less than half of the simulation cell length,  $L$ .

tion radius ensures that only molecules positioned within a pre-specified interaction sphere are included in the intermolecular energy and force calculations. Reducing the truncation radius increases the speed of the simulation, since fewer terms must be calculated in the force sum. Choosing too small of a truncation radius, however, will make the interactions non-physical. For most potentials, a cut-off radius around 9 Å is sufficient to maintain the accuracy of the potential while achieving a meaningful increase in computational speed [68, 99].

- *Applying periodic boundary conditions*

When using MD simulation to investigate bulk-like water or infinite CNTs, surfaces and boundaries can be eliminated from the system by introducing periodic boundary

conditions. As illustrated in Fig. 2.3, periodic boundary conditions are imposed by replicating the simulation box through space to form a periodic lattice. As molecules move about the original box, the periodic images in all other boxes move in the exact same way. When a molecule exits the original box, its periodic image enters through the opposite face such that the total number of atoms and molecules in the original box remains constant. To make the simulations computationally tractable, a cut-off radius must be implemented and molecules made to interact with only the “nearest-image” of the other  $N - 1$  particles within the simulation.

Having introduced these simulation protocols, we can now discuss the thermophysical behavior of water/CNT composite systems.

## CHAPTER III

### Water molecules inside and outside carbon nanotubes

#### 3.1 Introduction and motivation

As discussed in Chapter I, advances in CNT fabrication techniques and new experimental and theoretical investigations into fluid flow through ultra-confined geometries have generated interest in CNT-based nanofluidic devices [100]. Yun et al. recently fabricated stable and axially-aligned CNT arrays with an unprecedented length of 1 cm [37]. Li et al. built CNT networks containing well-aligned and uniform CNT Y-junctions with controllable branch and spur dimensions [101]. Skouidas et al. [102] and Holt et al. [43, 103] both report anomalously high mass flow rates through CNT membranes, while Shim et al. functionalized CNT surfaces to be biocompatible and capable of recognizing proteins [104].

The thermophysical and mass transport properties of such liquid-CNT systems — information necessary for device design and optimization — are related to the liquid-carbon intermolecular interactions and the associated surface wettability. These wetting characteristics can be implicitly incorporated into continuum-based analysis techniques by selecting appropriate boundary conditions for the mass, momentum, and energy transfer equations. For transport analysis at the nanoscale, however, where continuum assumptions break down [33, 105, 106], explicit modeling of individual

molecules is necessary to predict system performance.

Predictions from MD simulations have indicated that the behavior of liquid water both inside and outside of CNTs is strongly influenced by interactions with the carbon atoms [107–110]. Walther et al. predicted a spatially-varying density profile and non-uniform molecular orientation distribution in molecules adjacent to a 12.5 nm single-walled CNT [107]. Similar variations in water density were predicted by Choudhury for water-C<sub>60</sub> suspensions [108]. In investigating flow through single-walled CNTs, Kotsalis et al. predicted enhanced liquid ordering near the interior carbon surface and low liquid densities across the channel centerline [109]. Non-uniform interior water density profiles that vary as a function of CNT diameter were also reported by Hanasaki and Nakatani [110].

To compliment these investigations and assist in the design of future nanofluidic devices, we use MD simulations in this chapter to systematically investigate the effect of CNT diameter on the density, distribution, and orientation of water molecules inside and outside single-walled 1.1, 2.8, 6.9, and 10.4 nm diameter armchair CNTs [with chirality vectors of (8,8), (20,20), (50,50), and (75,75)]. We go beyond previously reported simulation results by elucidating the specific molecular interactions responsible for the spatially varying liquid properties. We also identify how, in addition to liquid water density, tube diameter can passively tune the distribution and orientation of confined water molecules. Such information, as discussed in later chapters, is necessary in understanding how water flows through and around CNTs, and how heat is transferred between a CNT and a surrounding liquid.

We begin by discussing the water-water and water-carbon intermolecular potential functions and the MD simulation techniques used to analyze the CNT-water system. Next, we study the effect of CNT diameter on liquid density both inside and outside

the CNT. We then identify the effect of CNT diameter on the distribution of water molecules near the CNT surface, and correlate these results to previously reported experimental measurements. Finally, we identify the molecular orientation distribution of water molecules both inside and outside the CNT, and discuss how the orientation is affected by tube diameter.

### 3.2 Molecular dynamics simulations set-up

#### 3.2.1 Water potential

We model water-water interactions using the TIP5P potential [76]. In TIP5P, each water molecule consists of one electrostatically-neutral oxygen atom, two positively-charged hydrogen atoms, and two negatively-charged but massless interaction sites. As discussed in Chapter II, the relative positions of the oxygen and hydrogen atoms correspond to known molecular structure data, while the positions of the charged interaction sites were tuned to reproduce the experimentally-observed properties of bulk water [76]. The three atoms and two interaction sites are fixed with respect to a local basis set and each molecule has zero net-charge.

The interaction between two water molecules,  $a$  and  $b$ , is a combination of one LJ interaction between the oxygen atoms, and sixteen electrostatic interactions between the two hydrogen atoms and two charge sites on each molecule:

$$\phi_{ab} = 4\epsilon_{oo} \left[ \left( \frac{\sigma_{oo}}{r_{oo}} \right)^{12} - \left( \frac{\sigma_{oo}}{r_{oo}} \right)^6 \right] + \sum_{i=1}^4 \sum_{j=1}^4 \frac{1}{4\pi\epsilon_o} \frac{q_i q_j}{r_{ij}}. \quad (3.1)$$

In Eq. (3.1),  $\epsilon_{oo}$  and  $\sigma_{oo}$  are the LJ parameters for the oxygen-oxygen interaction,  $r_{oo}$  is the oxygen-oxygen separation distance,  $q_i$  is the charge on site  $i$  of molecule  $a$ ,  $q_j$  is the charge on site  $j$  of molecule  $b$ ,  $\epsilon_o$  is the permittivity of free space, and  $r_{ij}$  is the charge site separation distance. We use the potential parameters and charges recommended by the potential developers [76].

As recommended in the original TIP5P implementation, we subject all molecular interactions to a 9 Å oxygen-oxygen cutoff radius at which interactions are truncated. It has been asserted that applying a spherical cut-off to a water model with long-range electrostatic interactions adversely effects system energetics and density [111]. To address this point, in Fig. 3.1 we show the net intermolecular force versus oxygen separation distance between two TIP5P water molecules in an equilibrated simulation of 512 molecules at a temperature of 298 K and a pressure of 1 atm. A range of forces (illustrated by the shaded envelope on the plot) are measured at each separation distance, and are related to the variety of relative orientations accessible to the molecules. The mean effective intermolecular force at each distance is also shown. For two molecules separated by more than 0.7 nm, the force envelope decays as  $1/(r_{oo})^4$ , characteristic of the interaction between two permanent dipoles [112]. The mean effective force at such separation distances (solid line) decays as  $1/(r_{oo})^7$ , consistent with the oxygen-oxygen LJ interaction. Consequently, the total force between two molecules, which is used to integrate the equations of motion, decays much more rapidly than the individual Columbic forces [which decay as  $1/(r_{oo})^2$ ]. This rapid decay is why, even with truncating the individual long-range Coulomb interactions, the TIP5P model can accurately reproduce water statistics [113]. Along with the domination of nearest neighbor interactions on overall dynamics, this trend also explains why others have been able to successfully model water using even smaller truncation spheres [114]. Such a rapid decay in intermolecular forces will not be present in ionic systems where individual molecules have a non-zero charge.

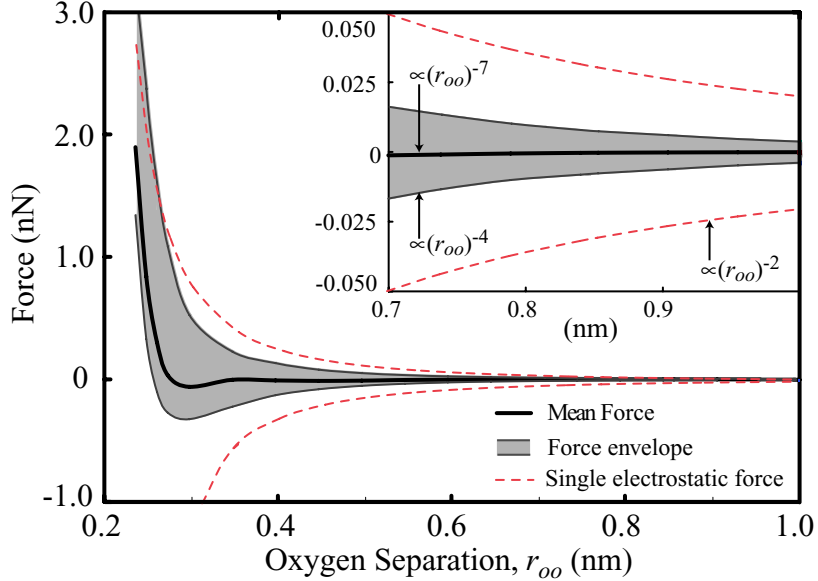


Figure 3.1: Intermolecular force versus oxygen separation distance between two water molecules in an equilibrated simulation of 512 molecules at a temperature of 298 K and a pressure of 1 atm. The gray envelope represents the range of forces predicted at each separation distance. The solid line is the mean force at each distance. Inset: Force envelope and mean force at separation distances greater than 0.7 nm. At these separations, the force envelope decays as  $1/(r_{\text{oo}})^4$ , characteristic of a permanent dipole-permanent dipole interaction. The mean effective force is related to the oxygen-oxygen LJ interactions and decays as  $1/(r_{\text{oo}})^7$ . Copyright 2008 American Institute of Physics.

### 3.2.2 Carbon-water potential

We model carbon-water interactions using the LJ potential recommended by Werder et al.:

$$\phi_{\text{co}} = 4\epsilon_{\text{co}} \left[ \left( \frac{\sigma_{\text{co}}}{r_{\text{co}}} \right)^{12} - \left( \frac{\sigma_{\text{co}}}{r_{\text{co}}} \right)^6 \right], \quad (3.2)$$

where  $r_{\text{co}}$  is the carbon-oxygen separation distance,  $\epsilon_{\text{co}} (= 1.11 \times 10^{-21} \text{ J})$  is the depth of the LJ energy well, and  $\sigma_{\text{co}} (= 0.319 \text{ nm})$  is the LJ length scale [83]. A 9 Å cutoff is applied to the carbon-oxygen interactions. Although the CNT-water contact angle is not well-defined from experiment [115], the recommended parameters accurately reproduce the observed wetting behavior of water on graphite.

The LJ potential is a model of atomic repulsion due to overlapping electron orbitals and atomic attraction due to atomic dipole dispersion (i.e., van der Waals forces). As discussed in Chapter II, the carbon atoms in a CNT are  $sp^2$  hybridized, meaning that

each carbon has one delocalized  $\pi$ -electron. Thus, in addition to carbon-oxygen LJ interactions and possible carbon-hydrogen interactions [116], water molecules may also interact with this delocalized electron. Previous MD simulations have demonstrated that the electrostatic interactions between a CNT and water are negligible compared to the van der Waals interactions, suggesting that electron-water interactions may be unimportant [117]. However, as discussed in Chapter II, additional ab initio potential development and more research into the CNT-water contact angle will determine if more sophisticated intermolecular potentials are necessary.

For computational efficiency, the carbon atoms within each simulation cell are fixed. In an extension of our previously reported work on monatomic LJ solid-fluid interfaces [61], we found that fixing the solid atoms had no detectable effect on the density, distribution, and diffusion characteristics of the interfacial liquid. Others have reported that fixing the carbon atoms has little effect on the dynamics of adjacent water [83].

Although stable single-walled nanotubes with diameters greater than 1.5 nm are difficult to fabricate, we have found that molecular behavior near multiwalled nanotubes is indistinguishable from that near single-walled CNTs due to the short range of the carbon-water interactions. Thus, the results from our single-walled nanotube simulations can be applied to multiwalled nanotubes with similar interior or exterior dimensions.

### 3.2.3 Simulation implementation and data collection

Our simulations are performed in the *NVT* ensemble. The rotational dynamics of the water molecules are modeled using the quaternion method and translational dynamics are integrated using the Verlet leapfrog scheme with a 0.5 fs timestep [68].

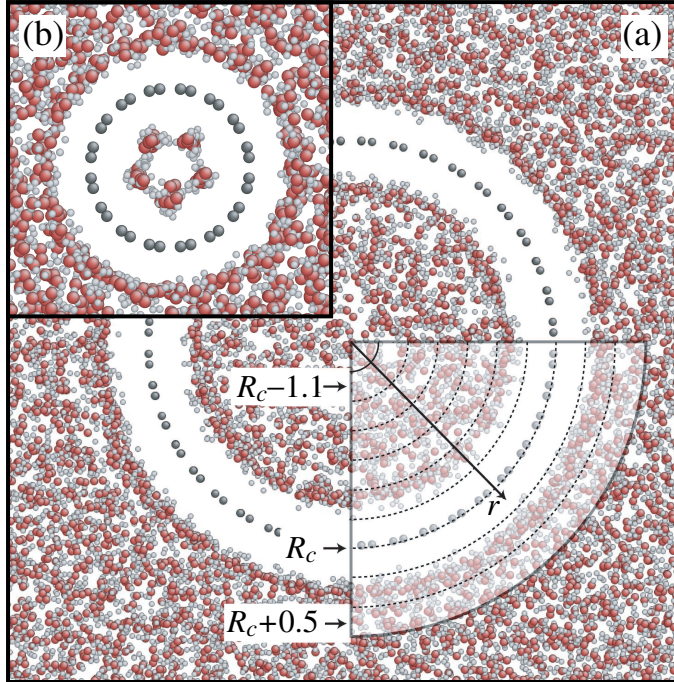


Figure 3.2: (a) Cropped axial snapshot of 2.8 nm CNT in water. Full simulation cell side length is 7.5 nm. The layering scheme used to analyze water near and within the CNT is also shown. Each layer has a thickness of 0.2 nm and is identified using the midpoint radial position,  $r$ . (b) Cropped axial snapshot of 1.1 nm CNT in water. Full cubic simulation cell side length is 5 nm. Both images are to the same scale and all numbers are in nm. Copyright 2008 American Institute of Physics.

The temperature is maintained at 298 K and the volume of the simulation cell is tuned to recover a water density of  $1000 \text{ kg/m}^3$  in regions outside the CNT far from the carbon surface. Periodic boundary conditions are imposed in all three directions.

To predict the equilibrium water density inside the 1.1, 2.8, and 6.9 nm CNTs, we simulated an open-ended sample of each nanotube in a large water bath at a temperature and pressure of 298 K and 1 atm. The bath density away from the tube was maintained at  $1000 \text{ kg/m}^3$  and water molecules were able to freely diffuse across the open ends of the tube. After 250 ps, the number of molecules enclosed inside the tube became steady in time, allowing us to determine the equilibrium density. The CNTs used to generate all of the subsequently reported data span the entire simulation cell (thereby isolating the confined and unconfined fluids) and were initially filled with the number of molecules corresponding to this equilibrium density.

Simulating the 10.4 nm CNT in a large water bath is computationally impractical. As such, we determined the equilibrium internal water density by predicting the pressure inside a  $64\text{ nm}^3$  cube centered within a nanotube of this size that spans the simulation cell. The number of molecules inside the CNT was tuned to recover a pressure of 1 atm within the cube. Applying this same technique to the 6.9 nm CNT generated an equilibrium water density within 1% of that predicted using the water-bath method.

In Fig. 3.2(a) we present a snapshot of the 2.8 nm CNT. We virtually partition the water into a sequence of shells concentric to the carbon surface. The thickness of each shell is 0.2 nm, which can sufficiently resolve spatial variations in the system while enclosing a statistically meaningful sample of water molecules. We identify each shell using its midpoint radial position,  $r$ , relative to the radial location of the CNT surface,  $R_c$ . We sort molecules based on the oxygen atom location, and position the shells such that the CNT surface is aligned with the shell boundary at  $r = R_c$ . The implementation of this layering scheme has no influence on the system dynamics. The shell-specific data presented throughout this report were then obtained by averaging the statistics of each shell over five data sets, with each set consisting of a 200 ps equilibration period followed by 250 ps of data collection.

### 3.3 Water density

Although the water molecules are continually moving, the time-averaged number of molecules within each liquid layer is well-defined. Far from the CNT, the average number of molecules in each layer is spatially uniform and corresponds to the bulk density of  $1000\text{ kg/m}^3$ . Closer to the CNT surface, as shown in Fig. 3.3, the unconfined water density is maximized at  $r=R_c+0.3\text{ nm}$ , minimized at  $r=R_c+0.5\text{ nm}$ , and slightly enhanced at  $r=R_c+0.7\text{ nm}$ . The density profiles within the unconfined water

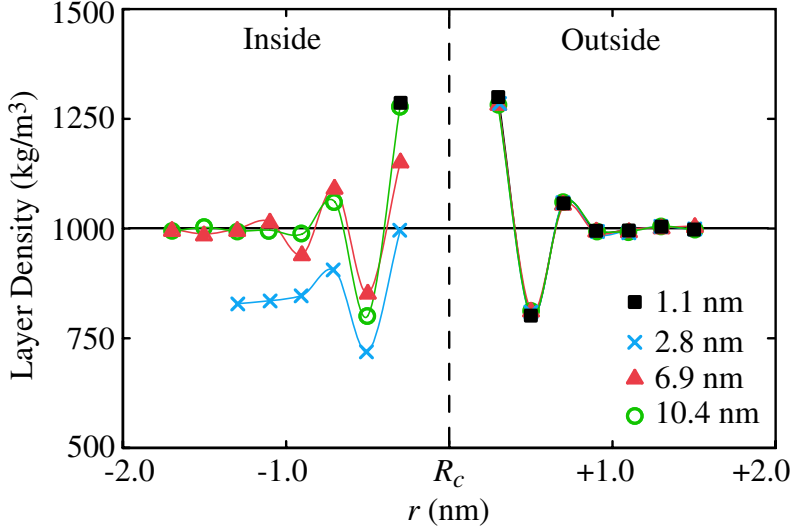


Figure 3.3: Water density inside and outside each CNT. The density profile in the unconfined water is invariant with CNT diameter and the same as that near a flat graphene sheet. The density profile in the confined water is a function of tube diameter. The inner-most layers for the 1.1 and 2.8 nm tubes are at  $r=R_c-0.3$  nm and  $r=R_c+1.3$  nm. Guidelines are added to highlight the minima and maxima. Copyright 2008 American Institute of Physics.

near each CNT are indistinguishable from what we found near a flat graphene sheet, implying that surface curvature has no effect on the radial density profile outside the CNT. In agreement with our predictions, scanning tunneling microscopy measurements of water on graphite reveal a distinct and dense water layer beginning 0.25 nm from the carbon surface [118]. Our findings also agree with electronic structure calculations of water molecules near a flat graphite surface, which predict a water/graphite equilibrium separation distance of 0.32 nm [119].

Similar density variations have been experimentally observed near the krypton-graphite interface [120] and predicted from MD simulation of liquid argon in a nanochannel [61]. This consistency suggests that although the current system includes electrostatic interactions between water molecules, the density variations in the interfacial region are caused by the carbon-oxygen and oxygen-oxygen van der Waals interactions. At  $r=R_c+0.3$  nm, the calculated carbon-oxygen potential energy due to LJ interactions is minimized, suggesting that the density maximum is indeed caused by

oxygen atoms (and the associated water molecules) being drawn into an energetically favorable region near the carbon surface. At distances greater than  $r=R_c+0.3$  nm, the carbon-oxygen LJ energy monotonically increases to zero and becomes too weak to directly influence water dynamics. Yet, the dense assembly of water molecules at  $r=R_c+0.3$  nm extends the influence of the solid. At  $r=R_c+0.5$  nm, which is 0.2 nm (one shell) beyond the water layer at  $r=R_c+0.3$  nm, the calculated oxygen-oxygen interaction energy between water molecules is maximized. Thus, the dense layer at  $r=R_c+0.3$  nm repels the molecules at  $r=R_c+0.5$  nm, making the region energetically unfavorable and generating the density minimum seen in Fig. 3.3. The density enhancement at  $r=R_c+0.7$  nm is then caused by attractive LJ interactions with the dense water layer at  $r=R_c+0.3$  nm. This explanation seems reasonable given that the individual oxygen-oxygen LJ equilibrium separation distance,  $2^{1/6}\sigma_{oo}$ , is 0.36 nm.

Also presented in Fig. 3.3 is the density profile of the water confined inside each CNT. Unlike the exterior density profiles, the radial distribution of confined fluid molecules is strongly related to tube diameter. Water confined within the 10.4 nm CNT behaves much like the outside water, with similar density oscillations and a bulk-like density of 1000 kg/m<sup>3</sup> recovered 1.0 nm from the solid surface. Inside the 6.9 nm tube, a bulk-like water density of 1000 kg/m<sup>3</sup> is also recovered at the tube centerline. The density variations penetrate further into the liquid than those in the exterior interface, however, suggesting that surface curvature influences molecular behavior within the confined region as the CNT diameter decreases below 10 nm.

Inside the 2.8 nm CNT, the equilibrium water density at the tube centerline is 840 kg/m<sup>3</sup> — significantly lower than the unconfined bulk density. Unlike in the larger tubes, where the 1 nm extent of surface effects is small compared to the tube diameter, the interface region within the 2.8 nm CNT is comparable to the tube

diameter. The tube is too small to fully attenuate the influence of the solid and the confined water does not recover bulk properties. Thus, the behavior of water confined in a CNT becomes geometry dependent as the CNT diameter is decreased below 10 nm, consistent with the MD predictions of Koga and Tanaka [106]. The water molecules inside the 1.1 nm CNT [see Fig. 3.2(b)] form a pentagon at  $r=R_c-0.3$  nm with a density equivalent to that of the first exterior layer. Although some molecules diffuse across the CNT centerline, the time-averaged number of particles outside this monolayer is very close to zero.

### 3.4 Water molecule distribution

In addition to radial density variations, the distribution of water molecules around the CNT surface and along the tube axis varies with position. The water position probability distributions,  $P_r(\theta, z)$ , at  $r=R_c+0.3$  nm and  $r=R_c-0.3$  nm for the 6.9, 2.8, and 1.1 nm CNTs are shown in Figs. 3.4(a)-3.4(c). The surface shading indicates mass distribution. The carbon structure of each CNT at  $r=R_c$  is also shown.

For all four nanotubes, water molecules at  $r=R_c+0.3$  nm assume a pattered mass distribution which follows the hexagonal structure of the carbon surface. This non-uniform mass distribution agrees with the dynamic force microscopy measurements of Ashino et al. [121], who found that the attractive forces within the carbon honeycomb for a singled-walled CNT were 45% greater than those near the individual carbon atoms. They demonstrated that the strong interactions form a potential well centered within the carbon honeycomb structure shaped much like the circular distribution profiles presented in Fig. 3.4. Their measured well-minimum is located 0.37 nm from the carbon surface, very close to the location of our predicted density maximum.

In the confined region,  $P_r(\theta, z)$  at  $r=R_c-0.3$  nm becomes more uniform with de-

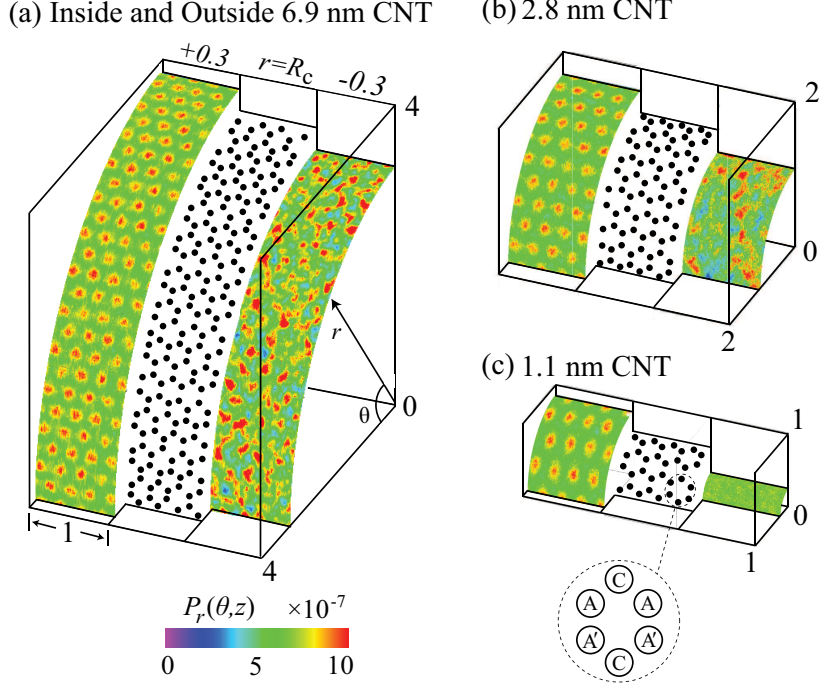


Figure 3.4: (a-c) Molecular distribution at  $r=R_c+0.3$  nm,  $r=R_c$ , and  $r=R_c-0.3$  nm for the 6.9, 2.8, and 1.1 nm CNTs. The mass distribution at  $r=R_c+0.3$  nm is similar for all tubes. For the 10.4 nm CNT, this same pattern is present at both  $r=R_c-0.3$  nm and  $r=R_c+0.3$  nm. The distribution at  $r=R_c-0.3$  nm for the 6.9, 2.8, and 1.1 nm CNTs becomes more uniform with decreasing CNT diameter. In frame (c), the detailed view identifies the circumferentially-aligned (C) and axially-aligned carbon atoms (A and A') that form the six-atom carbon honeycomb. All dimensions are in nm. Copyright 2008 American Institute of Physics.

creasing CNT diameter. Inside the 10.4 nm CNT (not shown), molecules assume a distribution indistinguishable from that near the exterior interface, confirming that curvature effects within such large CNTs are negligible. Within the 6.9 nm CNT, the mass distribution likewise assumes a honeycomb structure following the CNT surface. Compared to the 10.4 nm CNT, however, the patterning in the 6.9 nm CNT is less prominent. Inside the 2.8 nm CNT, density enhancements are present near and within some carbon honeycombs while other potential wells remain unfilled. Finally, within the 1.1 nm CNT, the molecular positions are completely uncorrelated to the carbon structure.

These trends suggest that reducing the CNT diameter pinches the interior potential wells centered within the carbon honeycombs, thereby squeezing molecules out of

the honeycomb structure and towards the CNT centerline. Unable to settle within the pinched potential well, the molecules at  $r=R_c-0.3$  nm become more uniformly distributed with decreasing CNT diameter. This pinching mechanism also explains why the 10.4 nm and 6.9 nm CNTs, which both recover a bulk-like  $1000 \text{ kg/m}^3$  density across the tube centerline, have different interior water density profiles: since fewer water molecules fill the pinched potential wells inside the 6.9 nm CNT honeycombs, the radial density at  $r=R_c-0.3$  nm is lower than that inside the 10.4 nm CNT. Squeezed further from the solid surface, however, the influence of the molecules at  $r=R_c-0.3$  nm near the 6.9 nm CNTs penetrates deeper into the confined fluid and extends the influence of the solid. Consistent with this idea, we have also found that with decreasing CNT diameter, the first peak of the carbon-oxygen radial distribution function inside the tube is located further from the carbon surface.

### 3.5 Water molecule orientation

To predict the influence of solid-liquid interactions on water molecule orientation, we calculate the unit dipole moment vector of all molecules with respect to the CNT surface normal. The vectors for all atoms in a given layer are then mapped onto a single unit sphere to form a layer-specific orientation distribution. In layers far from the surface, where interactions with the solid are fully attenuated, the molecular orientation distribution is uniform. At  $r=R_c+0.3$  nm and  $r=R_c-0.3$  nm, however, the molecules take on preferred orientations.

The orientation distribution map of water molecules at  $r=R_c+0.3$  nm for the 6.9 nm CNT is shown in Fig. 3.5(a). Similar behavior is observed outside all four CNTs. Although all orientations are accessible to molecules in this layer, the molecules are most likely to point in one of three preferred directions. To understand

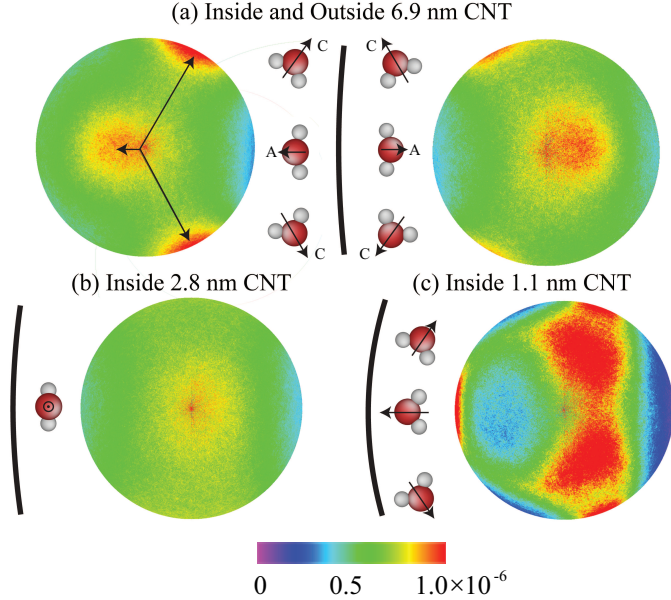


Figure 3.5: (a) Orientation distribution spheres at  $r=R_c+0.3$  and  $r=R_c-0.3$  nm for the 6.9 nm CNT. The projected length of the unit dipole moment vector, as printed in the figure, indicates the degree of rotation out of the plane of the page. Molecules are biased towards either an axially-aligned carbon atom (A) or a circumferentially-aligned carbon atom (C), as highlighted by the orientation distribution and the three water molecules beside the sphere. (b) Orientation distribution at  $r=R_c-0.3$  nm near the 2.8 nm CNT. A single preferred orientation points normal to (in or out of) the page. (c) Distribution at  $r=R_c-0.3$  nm near the 1.1 nm CNT. The water molecules form a pentagonal structure, resulting in two preferred orientations pointing away from the surface. A third preferred orientation points towards the CNT surface but is unbiased towards any particular axially or circumferentially-aligned carbon atom. Copyright 2008 American Institute of Physics.

this behavior, recall from Fig. 3.4 that water molecules are likely to reside in the potential well formed by the six-atom carbon honeycomb structure. As shown in Fig. 3.4(c), one pair of carbon atoms are axially-aligned and two pairs of carbon atoms are circumferentially-aligned. Although this symmetric arrangement generates a near circular potential well, water molecules within the potential well tend to point towards either a circumferentially-aligned carbon atom (C) or an axially-aligned carbon atom (A or A').

The orientation distribution maps of water molecules at  $r=R_c-0.3$  nm for the 6.9, 2.8, and 1.1 nm CNT are shown in Figs. 3.5(a)- 3.5(c). Although not presented here, we note that the molecules at  $r=R_c-0.3$  nm for the 10.4 nm nanotube orient like those at  $r=R_c+0.3$  nm but mirrored towards the CNT surface. At  $r=R_c-0.3$

nm for the 6.9 nm CNT, the water molecules are still likely to align with the CNT centerline axis but, compared to the 10.4 nm CNT, less likely to point towards a specific circumferentially-aligned carbon atom. This trend continues in the 2.8 nm CNT, where water molecules at  $r=R_c-0.3$  nm remain aligned with the CNT centerline axis, but have no affinity towards any particular circumferentially-aligned carbon atom. These correlations between orientation distribution and CNT diameter support the squeezing mechanism discussed earlier. As an increasing fraction of water molecules are squeezed out of the carbon honeycomb potential well, distinct interactions with the circumferentially-aligned carbon pair become less pronounced. Thus, with decreasing CNT diameter, interactions between water and specific circumferentially-aligned carbon atoms are less distinct and water molecules are instead spread over an increasing range of orientations. A preferred orientation remains in the direction of the axially-aligned carbon atoms, however, since these atomic positions are unaffected by surface curvature. For the 1.1 nm CNT, the molecules are fully squeezed from the surface potential wells and two preferred orientations point away from the carbon surface. The orientation distribution is now governed by water-water interactions, forming the pentagonal arrangement illustrated in Fig. 3.2(b) and manifested in the orientation distribution.

### 3.6 Summary and conclusion

We have investigated the effect of tube diameter on the density, molecular distribution, and molecular orientation of water inside and outside single-walled CNTs. As presented in Figs. 3.3 and 3.4, the density of unconfined water molecules is enhanced and the molecular distribution is non-uniform near the carbon surface. This behavior is caused by water molecules moving to low-energy potential wells formed near the

hexagonal carbon surface. The behavior of unconfined water molecules is invariant with CNT diameter. Inside the tube, however, curvature effects influence the molecular density and distribution near the CNT wall. The curved surface pinches the low-energy potential wells, thereby squeezing water molecules away from the carbon surface and decreasing the liquid density.

In addition to density and molecular distribution, interactions with the CNT influence the orientation of water molecules near the carbon surface. As presented in Fig. 3.5, the unconfined water molecules close to a CNT of any diameter are likely to point towards either a circumferentially or axially-aligned carbon atom. Water molecules confined within the 10.4 and 6.9 nm CNT orient much like unconfined water molecules. Inside the 2.8 nm CNT, where surface curvature effects are more relevant, water molecules are only likely to point towards axially-aligned carbon atoms. Inside the 1.1 nm CNT, the molecular orientation is governed by water-water interactions and molecules have no affinity towards any particular carbon atom.

As discussed in Chapters IV and V, the reduced influence of solid-water interactions on molecular orientation and distribution as the tube diameter gets smaller has important effects on the nature of water flow through CNTs. This behavior, as will be discussed in Chapters VI and VII, also affects phonon transport through water-filled CNTs.

## CHAPTER IV

### Continuum water flow in carbon nanotubes

#### 4.1 Introduction

Reports of new techniques for growing straight and axially-aligned CNTs and carbon nanopipes with controllable lengths and diameters have generated interest in nanofluidic devices [37, 43, 122–126]. As introduced in Chapter I, open-ended CNT membranes, which are formed by filling the interstitial region between 1-10 nm diameter CNTs with a non-porous matrix material, have been proposed as next-generation desalination [39, 40], gas separation [15], and gas storage devices [42]. Carbon nanopipe bundles, which are formed by depositing carbon on the pore walls of a removable molding template, are currently being tested as hypodermic drug-delivery needles [125] and cellular probes [127]. Despite these advances in fabrication capabilities and new insight into the mechanism of gas transport through CNTs [128], the nature of pressure-driven liquid flow through CNTs and carbon nanopipes is not clear [129].

The measured flow rates of glycerine and water through carbon nanopipes with diameters larger than 200 nm are consistent with predictions from the no-slip Poiseuille relation [126]. For 44 nm diameter carbon nanopipes, 7 nm diameter CNTs, and 1.6 nm diameter CNTs, the experimentally measured water flow rates exceed predictions

from the no-slip Poiseuille relation by up to several orders of magnitude [43, 122, 123]. Results from MD simulations suggest that flow enhancement in CNTs is caused by liquid slip at the water/carbon boundary and confinement-related changes in the liquid viscosity [63, 88, 109, 130]. The precise magnitude of this enhancement, however, is unknown and the variations in viscosity and slip length with diameter are not fully understood.

In this chapter, we use MD simulation to investigate pressure-driven water flow through seven armchair CNTs with diameters between 1.66 nm and 4.99 nm. We begin by using non-equilibrium simulation to (i) identify the relationship between pressure gradient and volumetric flow rate and (ii) measure the radial velocity profile. Next, we use equilibrium simulation to predict the viscosity of water inside in each tube. Finally, from the calculated viscosity, pressure gradient, and velocity profile, we predict the slip length inside each CNT. We use this data to demonstrate that, even in CNTs with diameters as small as 1.66 nm, water flow is accurately described by the slip-modified Poiseuille relation.

## 4.2 Pressure-driven liquid flow

When subjected to an axial pressure gradient,  $\partial P/\partial z$ , the radial velocity profile,  $v_z(r)$ , of an incompressible liquid with a slip-boundary condition creeping steadily through a tube of radius  $R$  is

$$v_z(r) = \frac{R^2}{4\mu} \left[ 1 - \frac{r^2}{R^2} + \frac{2L_s}{R} \right] \frac{\partial P}{\partial z}, \quad (4.1)$$

where  $\mu$  is the liquid viscosity and  $L_s$  is the slip length at the liquid/solid boundary. The slip length, which describes the velocity discontinuity between the liquid and the

solid, is typically defined as [131, 132]

$$L_s \equiv \left. \frac{v_z(r)}{dv_z/dr} \right|_{r=R}. \quad (4.2)$$

Predictions from MD simulation indicate that Eq. (4.1) (the Poiseuille parabola) is valid when the characteristic flow diameter is 5-10 times larger than the characteristic molecular diameter ( $\approx 0.17$  nm for water) [31, 133]. In smaller systems, where the continuum approximation is invalid, molecular transport is governed by the liquid structure and collective molecular motion [33, 65, 78].

In Fig. 4.1, we show how liquid slip at the solid/liquid boundary affects the velocity profile inside the tube. When  $L_s = 0$ , the liquid velocity at the wall is zero and the maximum velocity (at the tube centerline) is twice the mean flow velocity. With increasing slip length, the mean flow velocity increases, the relative difference between the maximum and minimum velocities decreases, and the velocity profile becomes more plug-like [17]. The velocity of the liquid at the solid surface can also be quantified using the slip coefficient,  $L_c$ . As shown in Fig. 4.1, the slip coefficient is the difference between the radial position at which the velocity profile would become zero and the radial position of the solid surface [134]. For linear velocity profiles, (e.g., boundary-driven Couette flow), the slip length and slip coefficient are equal. These values are different for Poiseuille flow.

The volumetric flow rate with slip,  $Q_S$ , is found by integrating the velocity profile over the tube cross-section [25]:

$$Q_S = \int_0^R v_z(r) 2\pi r dr = \frac{\pi \left[ (d/2)^4 + 4(d/2)^3 L_s \right]}{8\mu} \frac{\partial P}{\partial z}, \quad (4.3)$$

where  $d (= 2R)$  is the tube diameter. Equation (4.3) is the slip-modified Poiseuille flow rate; the no-slip Poiseuille flow rate,  $Q_N$ , is found by setting  $L_s$  equal to zero.

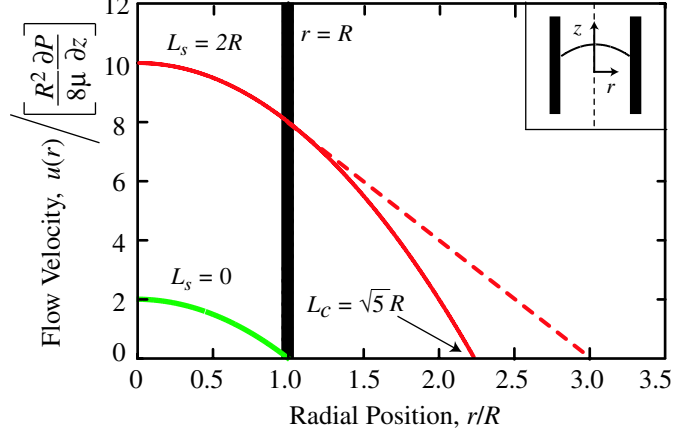


Figure 4.1: No-slip Poiseuille flow ( $L_s = 0$ ) and slip Poiseuille flow with  $L_s = 2R$  through a tube with radius  $R$ . The thick vertical lines indicate the location of the tube wall. The slip coefficient for the slip system,  $L_c$ , is  $\sqrt{R^2 + 2RL_s} = \sqrt{5}R$ . The flow velocity is normalized by the mean velocity corresponding to no-slip flow.

The flow rate enhancement,  $\varepsilon$ , is defined as the ratio of the actual flow rate,  $Q$ , to  $Q_N$ :

$$\varepsilon \equiv \frac{Q}{Q_N}. \quad (4.4)$$

If the actual flow is modeled using Eq. (4.3), such that  $Q = Q_S$ , the enhancement factor is:

$$\varepsilon = \left[ 1 + 8 \frac{L_s(d)}{d} \right], \quad (4.5)$$

where  $L_s(d)$  is the diameter-dependent slip length. In addition to liquid slip, however, diameter-related changes in the fluid viscosity may affect the flow [135, 136]. If  $Q_N$  is calculated using the bulk liquid viscosity,  $\mu_\infty$ , then the diameter-specific fluid viscosity,  $\mu(d)$ , can be incorporated into Eq. (4.5) such that

$$\varepsilon = \left[ 1 + 8 \frac{L_s(d)}{d} \right] \frac{\mu_\infty}{\mu(d)}. \quad (4.6)$$

## 4.3 Experimental measurements

### 4.3.1 Water flow through carbon nanopipes

Measurements of liquid flow through single carbon nanopipes were first reported by Sinha et al., who fabricated 200-300 nm diameter carbon nanopipes in a porous alumina template using chemical vapor deposition [126]. The walls of the carbon nanopipes, although initially amorphous, were “graphitized” into structures that resembled multiwalled CNTs using a high-temperature annealing procedure. The average diameter of each carbon nanopipe, which varies by 10 to 20 percent along its axis, was measured using an environmental scanning electron microscope. Liquid flow through a carbon nanopipe was established by placing two liquid droplets with different diameters at opposite ends of it. The pressure gradient was calculated from the difference in the droplet diameters and the flow rate was evaluated by measuring the variation of the droplet diameters with time. The flow rates of glycerine through both amorphous and graphitized carbon nanopipes were consistent with predictions from the no-slip Poiseuille relation (i.e.,  $\varepsilon \approx 1$ ). Subsequent measurements by Ray et al., who used a syringe pump to drive water through 300-500 nm diameter carbon nanopipes fabricated using a similar procedure, are also consistent with the no-slip Poiseuille relation [137].

Whitby et al. measured water flow rates through an array of aligned carbon nanopipes with an average diameter of 44 nm [122]. The carbon nanopipe array was formed by coating the porous surface of an aluminium oxide template with layers of carbon via chemical vapor deposition. Unlike the carbon nanopipes of Sinha et al., the carbon nanopipes fabricated by Whitby et al. were not annealed and the carbon surface remained amorphous. The average inner diameter of the carbon nanopipes, which is controlled by the template pore size, was measured using transmission elec-

Table 4.1: Experimentally measured flow enhancements and apparent water/carbon slip lengths. The flow enhancement factor is calculated using Eq. (4.4) and the apparent slip length is calculated using Eq. (4.5).

	Diameter (nm)	Enhancement	Slip Length, $L_s$ (nm)	
Carbon Nanopipes	300-500	$\approx 1$	0	Ref. [43]
	44	22-34	113-177	Ref. [123]
Carbon Nanotubes	7	$10^4\text{-}10^5$	3900-6800	Ref. [137]
	1.6	560-9600	140-1400	Ref. [122]

tron microscopy (TEM). A hydrostatic pressure difference was applied using a syringe pump and the flow rate was determined by periodically weighing the water that exited the array. The water flow rate exceeded predictions from the no-slip Poiseuille relation with an enhancement factor of 22 and 34. From this enhancement data, as summarized in Table (4.1), Whitby et al. used Eq. (4.5) to calculate a slip length of 113 nm to 177 nm.

#### 4.3.2 Water flow through carbon nanotubes

Experimental measurements of water flow through CNTs were first reported by Majumder et al., who examined pressure-driven flow through a membrane of open-ended and axially-aligned CNTs in a non-porous polymer matrix [123]. The CNT membrane was fabricated by spin-coating an aligned array of CNTs with a solution of polystyrene and toluene, followed by drying in a controlled environment to form a CNT/polystyrene composite system. Next, an H<sub>2</sub>O plasma-enhanced oxidation process was used to remove a thin layer of polystyrene from the membrane, opening the closed tips of the CNTs. The CNT density, based on analysis of scanning electron microscopy images, was estimated to be  $6 \times 10^{10}$  tubes/cm<sup>2</sup> and the mean flow diameter of the CNTs was estimated to be 7 nm by measuring the ion permeability of the membrane [123, 138]. The reported flow enhancement factor for the membrane, as summarized in Table (4.1), is between  $10^4$  and  $10^5$ . The apparent slip length, calcu-

lated by solving Eq. (4.5) for  $L_s$  using the measured enhancement factor, is between 3900 nm and 6800 nm. This slip length is much larger than the 10-100 nm slip length typically measured for hydrophobic surfaces and the 14-63 nm water/graphene slip length predicted from MD simulations [139].

Holt et al. report on measurements of water flow through a CNT membrane with a mean CNT diameter of 1.6 nm [43]. The membrane was formed by encapsulating an array of aligned CNTs in a hard silicon nitride matrix using low-pressure chemical vapor deposition. Excess silicon nitride was then removed from the membrane surface by ion milling and the ends of the CNTs were opened using reactive ion etching. The average CNT diameter was estimated using size-exclusion measurements and TEM image inspection. The pore density, also calculated from the TEM images, was  $2.5 \times 10^{11}$  tubes/cm<sup>2</sup>. As shown in Table (4.1), the calculated flow enhancement factor for water is between 560 and 9600 and the apparent slip length, calculated using Eq. (4.5), is 140 nm to 1400 nm.

#### 4.3.3 Discussion

Although the data from the experimental investigations suggest that liquid flow through sub-100 nm diameter carbon nanopipes and CNTs is enhanced, the magnitude of the enhancement and its variation with diameter—especially in CNTs with diameters smaller than 10 nm—is not clear. Surprisingly, the results of Majumder et al. compared to those of Holt et al. suggest that the flow enhancement increases by a factor of 10-100 as the mean CNT diameter is increased from 1.6 nm to 7 nm. The opposite trend is observed in larger carbon nanopipes, where the enhancement decreases with increasing diameter. Curvature-induced changes to the slip length, differences in CNT and carbon nanopipe internal surface structures, and changes in

the liquid viscosity with CNT diameter have been suggested as mechanisms to explain the differences between the experimental reports [129]. Using MD simulation, we can examine the variation in flow enhancement with diameter systematically and investigate each of these mechanisms independently.

#### 4.4 Data collection

We use MD simulation to examine pressure-driven water flow through 1.66, 2.22, 2.77, 3.33, 3.88, 4.44, and 4.99 nm diameter single-walled armchair CNTs. A snapshot of a typical water/CNT system is presented in Fig. 4.2 and the chirality vector for each CNT is listed in Fig. 4.3. Interactions between water molecules are modeled using the TIP5P potential [76] and interactions between water molecules and carbon atoms are modeled using the LJ potential of Werder et al. [83]. Simulations are performed in the *NVT* ensemble at a temperature of 298 K.

For computational efficiency, we simulate water flow through single-walled CNTs with fixed carbon atoms [88, 130]. Although stable single-walled nanotubes with diameters greater than 1.5 nm are difficult to fabricate, we have found that molecular behavior near multiwalled nanotubes is indistinguishable from that near single-walled CNTs due to the short range of the carbon-water interaction. Thus, the results from our single-walled nanotube simulations can be applied to multiwalled nanotubes with similar interior or exterior diameters.

To predict the equilibrium water density inside the CNTs, we simulated an open-ended sample of each nanotube in a large water bath at a temperature and pressure of 298 K and 1 atm [62]. Using the procedure introduced in Chapter III, the bath density away from the tube was maintained at 1000 kg/m<sup>3</sup> and water molecules were able to freely diffuse across the open ends of the tube. After 250 ps, the number of

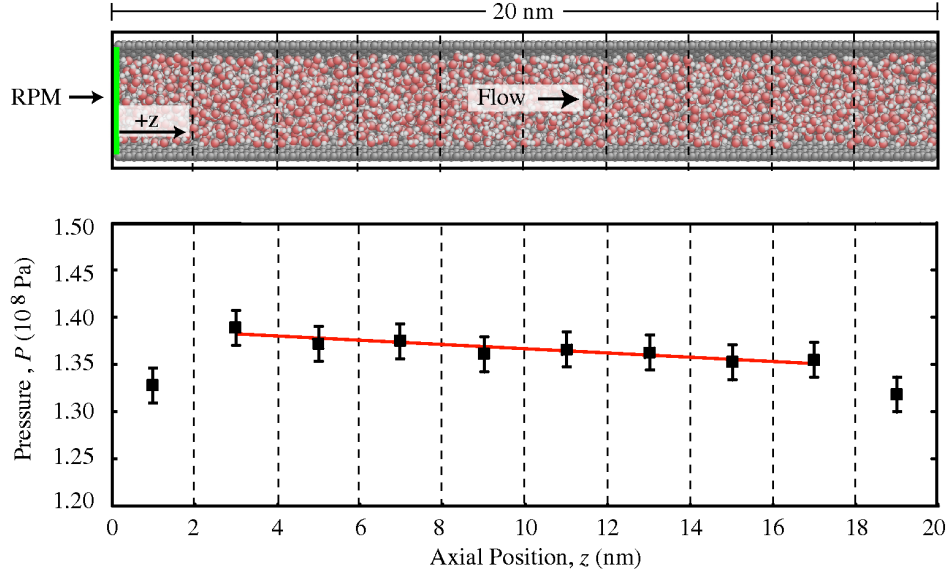


Figure 4.2: Axial pressure gradient inside the 2.77 nm diameter CNT. The pressure within each sub-volume is predicted using the virial expansion method. Within the sampling region, the variation in liquid density with axial position is less than 1%. Copyright 2008 American Institute of Physics.

molecules enclosed inside the tube became steady in time, allowing us to determine the equilibrium density. The CNTs used in this study were filled with the number of molecules corresponding to this equilibrium density. Each CNT contains between 3100 and 6769 water molecules, corresponding to tube lengths that vary from 80 nm (for the 1.66 nm diameter CNT) to 12 nm (for the 4.99 nm diameter CNT). The water density inside each CNT is consistent with the densities reported by others [88, 110]

A pressure gradient and flow field are established inside the tube by placing a reflecting particle membrane (RPM) [133] at  $z=0$  (periodic boundary conditions are imposed in the  $z$ -direction). The RPM operates as follows: molecules crossing the membrane in the desired flow direction pass freely; molecules crossing the membrane in the opposite direction have some probability,  $p$ , of being elastically reflected in the flow direction. The water flow rate and magnitude of the pressure gradient inside the tube are tuned via the magnitude of  $p$ . As depicted in Fig. 4.2, we calculate  $\partial P/\partial z$  by evaluating the pressure within several sub-volumes along the tube axis and

performing a linear regression analysis. Since we know the position and momentum of each particle in the simulation, the radial velocity profile can be calculated directly. The volumetric flow rate is then found by integrating the velocity profile over the CNT cross-sectional area. Since water molecules remain at least 0.2 nm away from the CNT surface [62, 88, 110] (i.e., there is no flow in these regions), we note that the actual flow diameter is smaller than the full CNT diameter  $d$  that we, remaining consistent with experimental reports [43, 123], use to calculate  $Q_N$  and  $\varepsilon$ .

In Fig. 4.3, we present the volumetric flow rate versus pressure gradient for all seven CNTs. Each data point is the average of at least five independent trials, which consist of a 250 ps equilibration period (during which the flow system reaches a steady state) followed by a 300 ps data collection period. The mean flow velocities are 3-14 m/s. Due to the time scales accessible in MD (a few ns), we cannot resolve the experimental mean flow velocities of 0.01-1 m/s. However, the linear relationship between the flow rate and the pressure gradient, which is consistent with Eq. (4.3), suggests that our results will be applicable to the flow rates realized in the experiments. Unlike previous MD simulations of water flow through CNTs, where the mean flow velocities were 100-300 m/s [88, 110], we are well below the molecular thermal velocity (340 m/s at a temperature of 298 K).

In Fig. 4.4, we present the flow enhancement versus CNT diameter for the seven CNTs considered in this work. For comparison purposes, we also plot the enhancement corresponding to a bulk viscosity ( $\mu_\infty=0.89$  mPa-s, see below) and our predicted slip length for water flow past a flat graphene sheet ( $L_{s,\infty}=30$  nm, see below). These results have three important features. First, the magnitude of the flow enhancement decreases with increasing CNT diameter. Second, with increasing diameter, our predicted enhancement converges to that predicted from Eq. (4.5) with a 30 nm slip

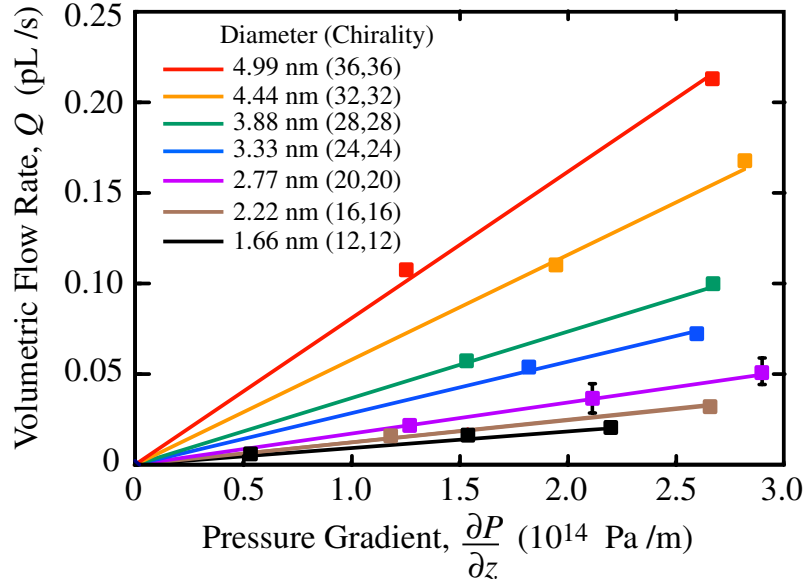


Figure 4.3: Volumetric flow rate in the CNTs versus pressure gradient. Over the pressure range investigated here,  $Q$  is directly proportional to  $\partial P / \partial z$ . Error bars, as shown for the 2.77 nm diameter CNT, are similar for all points and the chirality vector for each CNT is listed in the legend. Copyright 2008 American Institute of Physics.

length and a bulk viscosity. This finding is opposite to the results of Majumder et al. compared to those of Holt et al., which suggest that the flow enhancement (relative to the no-slip predictions) *increases* by a factor of 10-100 as the mean CNT diameter is increased from 1.6 nm to 7 nm. Third, the variation in  $\varepsilon$  with CNT diameter cannot be captured using a single slip length. This result is consistent with previous simulations of simple fluids confined inside CNTs, where both the slip length and the viscosity were found to be dependent on CNT diameter [130]. A CNT-specific water viscosity and slip length (not bulk water properties and a uniform slip length) should therefore be used when making comparisons between the MD-measured enhancement and that predicted from Eq. (4.5).

#### 4.5 Viscosity and slip length predictions

In Fig. 4.5 we present the water viscosity versus CNT diameter for all seven CNTs. We predict the viscosity from the axial self-diffusion coefficient,  $D_z$ , by evoking the

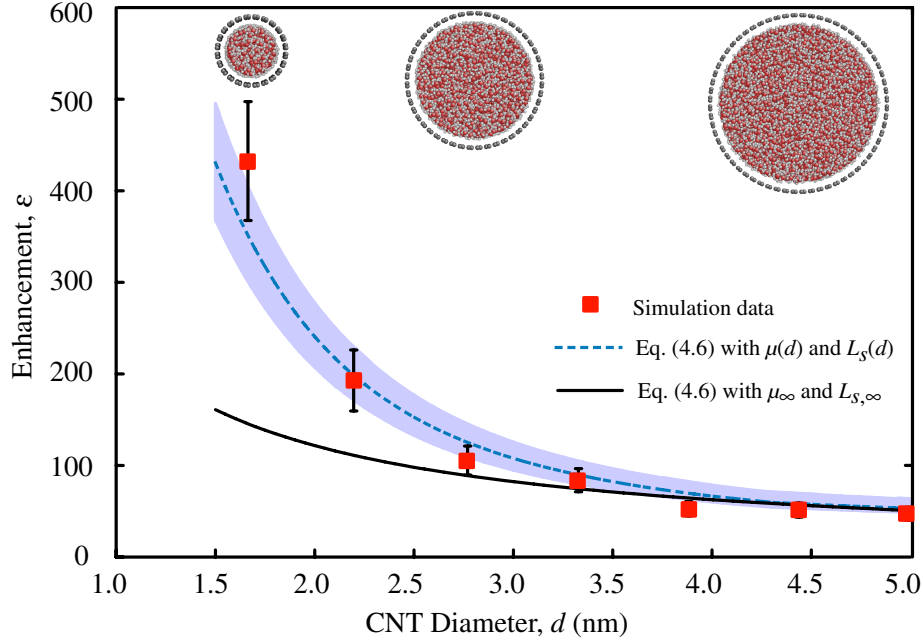


Figure 4.4: Flow enhancement (calculated flow rate divided by  $Q_N$ ) as predicted from MD simulations. Superimposed on the simulation data is the enhancement predicted from Eq. (4.5) with  $L_s=30$  nm and  $\mu(d) = \mu_\infty$ , and the enhancement predicted from Eq. (4.5) using a CNT-specific slip length and viscosity. The shading indicates our 15% uncertainty in the predicted viscosity and slip length data and the error bars indicate our 15% uncertainty in the calculated flow rates. The enhancement range reported for 1.6 nm CNTs is  $560 < \varepsilon < 9600$ . A point corresponding to the reported flow enhancement through 7 nm diameter CNTs would have an  $\varepsilon$  value of 50000, approximately 100 times greater than the maximum value on our plot. Copyright 2008 American Institute of Physics.

Einstein relation [98, 140, 141]:

$$\mu = \frac{k_B T}{3\pi a} \frac{1}{D_z}, \quad (4.7)$$

where  $k_B$  is the Boltzmann constant and  $a$  is the molecular diameter (taken to be 0.17 nm from the average positions of the hydrogen atoms and charge sites relative to the oxygen atom in the TIP5P water model [76]). We predict  $D_z$  from the Green-Kubo linear response relation [68]

$$D_z = \frac{1}{N} \sum_{i=0}^N \int_0^\infty \langle v_{i,z}(t) \cdot v_{i,z}(0) \rangle dt, \quad (4.8)$$

where  $t$  is time and  $v_{i,z}$  is the axial center-of-mass velocity of molecule  $i$ . The brackets denote an autocorrelation and the summation is over all molecules,  $N$ . Unlike in smaller diameter CNTs, where multiple regimes of diffusion have been reported [78],

$D_z$  for each of our tubes is invariant with autocorrelation length.

To test the validity of Eq. (5), we performed equilibrium simulations of bulk water at a temperature of 298 K and pressure of 1 atm. Our calculated self-diffusion coefficient is  $2.63 \times 10^{-9}$  m<sup>2</sup>/s, which matches the TIP5P self-diffusion coefficient reported by Mahoney and Jorgensen [113]. Using this self-diffusion coefficient and the molecular diameter of 0.17 nm, the viscosity calculated from Eq. (5) is 1.02 mPa-s. This value is in good agreement with the experimentally measured value of 0.89 mPa-s [142] and the 1.06 mPa-s value we predict directly from MD simulations and Green-Kubo linear response theory [68].

Since both the diffusion coefficient [61] and viscosity [143] of liquids near solid surfaces are spatially varying, we recognize that our calculated viscosity represents a cross-sectional averaged effective viscosity. We find that our viscosities are well described by a weighted-average of the viscosities in the interface and bulk-like regions in the CNT cross-section,

$$\mu(d) = \mu_i \frac{A_i(d)}{A_c(d)} + \mu_\infty \left[ 1 - \frac{A_i(d)}{A_c(d)} \right], \quad (4.9)$$

where  $\mu_i$  and  $A_i$  are the viscosity and area of the interface region, and  $A_c$  is the total cross-sectional area. Based on the discussion in Chapter III, we define the interface to be the annular region located within 0.7 nm of the CNT surface, as illustrated in Fig. 4.5. We set  $\mu_i$  equal to the viscosity inside the 1.66 nm diameter CNT (where the interface region covers 97% of the cross-sectional area). In CNTs with diameters smaller than 1.66 nm, where the tube diameter is less than ten times the water molecule diameter and subcontinuum transport phenomena are present, Eq. (4.9) will not accurately predict the water viscosity [78, 135].

We predict the slip length of the confined water from the radial velocity profiles

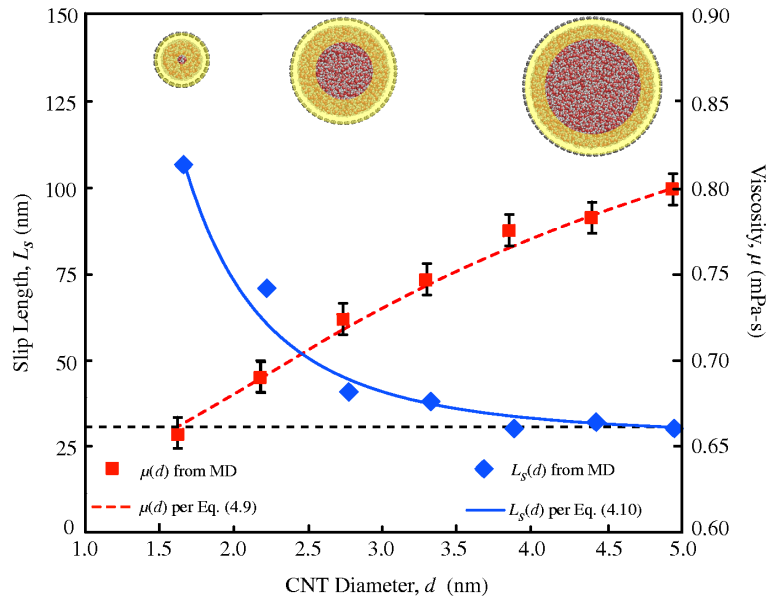


Figure 4.5: Variation of viscosity and slip length with CNT diameter. The MD viscosity was predicted from equilibrium simulation using Eq. (4.7). The highlighted annular regions on the CNT snapshots indicate the interface area used to evaluate Eq. (4.9). The MD slip length was evaluated from the velocity profile inside each CNT and Eq. (4.2). The variation in slip length with CNT diameter is fit using Eq. (4.10) with  $C=352 \text{ nm}^4$ . The dashed horizontal line identifies  $L_{s,\infty}(=30 \text{ nm})$ . The uncertainty in the slip length is  $\pm 1 \text{ nm}$ , making the error bars smaller than the data points. Copyright 2008 American Institute of Physics.

measured during the non-equilibrium flow simulations. By fitting each velocity profile to the parabolic function  $v_z(r)=Ar^2+B$ , we can directly calculate  $L_s$  from Eq. (4.2). We constrain the fit such that  $A$  and  $B$  satisfy the viscosity predicted inside each CNT from our equilibrium simulation. This approach is in contrast to that of Sokhan et al. [130], who fit both the viscosity and slip length to the velocity profile.

To illustrate this procedure, consider the velocity profile for the 2.88 nm CNT presented in Fig. 4.6. If we use the procedure of Sokhan et al., the viscosity is 0.42 mPa-s and the slip length is 24 nm. Since this viscosity is below the value of 0.72 mPa-s predicted from our equilibrium simulation, the calculated slip length will be underestimated. If we constrain the fit, the viscosity is set to 0.72 mPa-s and slip length becomes 41 nm. The slip lengths for all seven CNTs, as calculated using constrained fits, are presented in Fig. 4.5. We suspect that the unconstrained fit procedure may be responsible for the anomalously small slip lengths reported by Sokhan et al. [130].

Petravic and Harrowell [144, 145] have developed a linear response procedure for calculating the slip length at planar liquid/solid boundaries. While this approach cannot be applied to cylindrical systems where there is only one solid surface, it can be used to validate our slip length calculation procedure. We begin by performing equilibrium simulations of water between two infinite graphene sheets separated by 5 nm. Using the procedure of Petravic and Harrowell, we predict a water/graphene slip length of 30 nm. Next, we induce water flow through the channel and evaluate the velocity profile. Using the velocity fitting procedure discussed above, we calculate a slip length of 31 nm. The predicted slip lengths are within the  $\pm 1$  nm uncertainty we associate with both techniques. We also note that, using the 10 nm hydraulic diameter of the channel, the viscosity predicted from the weighted-average relation

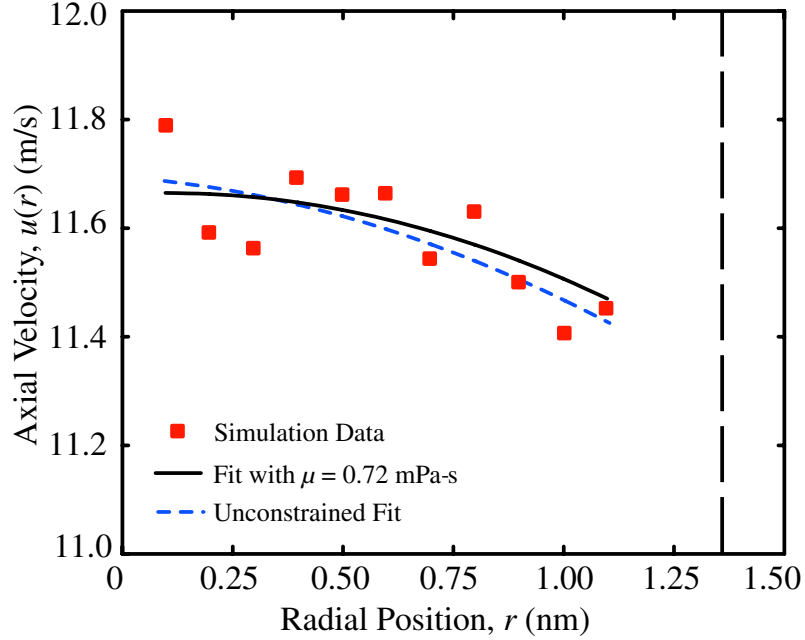


Figure 4.6: Radial velocity profile inside 2.77 nm diameter CNT fit using both unconstrained and constrained fitting procedure. The vertical dashed line at 1.38 nm represents the CNT surface. As discussed in the text, water molecules remain 0.2 nm from the CNT surface. The standard deviation for each point is approximately 2 m/s. Based on a  $\chi^2$  goodness-of-fit test, we can state with a 90% confidence interval that the data used to generate this profile is consistent with our parabolic constrained fit. This confidence interval increases to 95% for the 2.22 nm CNT and to 99% for all the larger tubes. Copyright 2008 American Institute of Physics.

presented in Eq. (7) is 0.88 mPa-s. This value agrees with the value of 0.83 mPa-s we predict using the Einstein relation presented in Eq. (5).

Liquid slip at the solid/liquid boundary is a rate process limited by the ability of molecules to hop between open surface lattice sites [146]. The slip length is therefore large when the solid/liquid binding energy is weak and the solid/liquid potential energy landscape near the solid surface is smooth. In Chapter III, we demonstrated and discussed how decreasing the CNT diameter weakens the coupling between water molecules and the carbon surface [62]. We attribute the increase in slip length with decreasing CNT diameter to this phenomenon. We also showed how the effect of surface curvature on the potential energy landscape becomes negligible as the CNT diameter is increased beyond 5 nm [62]. This trend explains why the slip length

converges to 30 nm—the slip length we predict for a flat graphene sheet—as the CNT diameter increases. As shown in Fig. 4.5, this variation in slip length with CNT diameter is well described by the empirical relation

$$L_s(d) = L_{s,\infty} + \frac{C}{d^3}, \quad (4.10)$$

where  $L_{s,\infty}$ (=30 nm) is the slip length over a flat graphene sheet and  $C$  is a fitting parameter.

#### 4.6 Comparisons to the Poiseuille relation

In Fig. 4.4, we compare the flow enhancement, as measured from our non-equilibrium simulations, to that calculated using Eq. (4.5) with the viscosity and slip length data presented in Fig. 4.5. For the CNTs with diameters between 2.11 nm to 4.99 nm, the enhancement predicted from Eq. (4.5) is within 10% of the enhancement measured during the simulation. For the 1.66 CNT, the values are within 25%. This excellent agreement, coupled with the parabolic velocity profiles detected in the CNTs, indicate that flow through CNTs with diameters greater than and equal to 1.66 nm can be modeled using the slip-modified Poiseuille relation. This finding is consistent with previous investigations of simple fluids, where flow could be modeled using tools from continuum theory when the characteristic flow dimension is at least ten times the molecular diameter [31, 133].

As summarized in Table (4.2), the results from our MD simulations suggest four regimes of water flow inside CNTs. In CNTs with diameters smaller than about 1.6 nm, the interface region spans the entire cross-sectional flow area and a continuum description of the fluid is invalid. As discussed in Chapters I and V, the flow characteristics are related to the liquid's intermolecular structure. The movement of individual molecules must be considered when modeling transport through the tube.

Table 4.2: Regimes of water flow through CNTs, as predicted from MD simulation.

Diameter, $d$ (nm)	Enhancement, $\varepsilon$	Enhancement Magnitude
< 1.6	Subcontinuum flow	Varies with liquid structure
1.6 – 5	$\left[1 + 8 \frac{L_s(d)}{d}\right] \frac{\mu_\infty}{\mu(d)}$	~500
5 – 10	$\left(1 + 8 \frac{L_{s,\infty}}{d}\right) \frac{\mu_\infty}{\mu(d)}$	~100
> 10	$\left(1 + 8 \frac{L_{s,\infty}}{d}\right)$	1-10

In CNTs with diameters between 1.6 nm and 5 nm, a continuum description of the fluid is valid but diameter-related changes to the slip length and the viscosity must be considered when predicting the flow enhancement. When the CNT diameter is between 5 nm and 10 nm, confinement-related changes to the water viscosity must be considered and the slip length will be close to the flat-sheet limit. Finally, in CNTs with diameter larger than 10 nm, diameter-related changes in the water viscosity are negligible and the slip length will be equal to the flat sheet limit. The flow enhancement will then decrease with increasing CNT diameter until  $L_s \ll D$ , when the flow rate becomes consistent with predictions from the no-slip Poiseuille relation.

In addition to the results presented here, Joseph and Aluru used MD simulation to investigate gravity-driven water flow through a 2.22 nm diameter CNT [88]. Using a cross-sectional flow area definition consistent with that used here, we calculate a flow enhancement factor of 459 from their data. We believe that the difference between this value and our result (184) for the same tube is due to differences in the potential functions used to model the molecular interactions. The water-carbon LJ potential function used by Joseph and Aluru predicts a weaker water/carbon interaction energy than the potential used here. This difference will increase the slip length in their flow simulations, leading to a larger flow enhancement. Additionally, Joseph and Aluru used the SPC/E rigid water potential function, which will lead to a different water

viscosity.

The comparison between our simulation data and that reported by Joseph and Aluru illustrates the sensitivity of MD predictions to the chosen intermolecular potential functions. As discussed by Koumoutsakos et al., increasing the magnitude of the water/carbon LJ interaction energy by 50 and 100 percent decreases the water/carbon slip length by factors of two and four [139]. Likewise, depending on the choice of water model, the bulk-water viscosity predicted from MD at a temperature of 298 K varies from 0.6 to 1.0 mPa-s [141]. These differences impede a direct comparison between MD simulations performed using different interatomic potentials and make quantitative comparisons to experimental data difficult. When using the same set of parameters to systematically investigate a range of systems, however, MD simulation can effectively elucidate changes in system-level transport and deviations from continuum mechanics [147]. Improvements to intermolecular potential functions, especially the water/carbon potential function, will enable a more quantitative comparison between simulation and experiment.

#### 4.7 Comparisons to experiment

Our MD-predicted enhancement for the 1.66 nm diameter CNT, as presented in Fig. 4.7, is near the lower end of the 560-9600 enhancement range measured by Holt et al. for a membrane of CNTs with a mean diameter of 1.6 nm. Since the water intermolecular orientations in a 1.6 nm diameter CNTs are uncorrelated [65], the net electric field in each region of space is close to zero and the effects of molecular polarizability on flow should be negligible. We therefore do not expect that simulations using more sophisticated water models will predict significantly different flow enhancements. However, possible variations in the water-CNT interaction

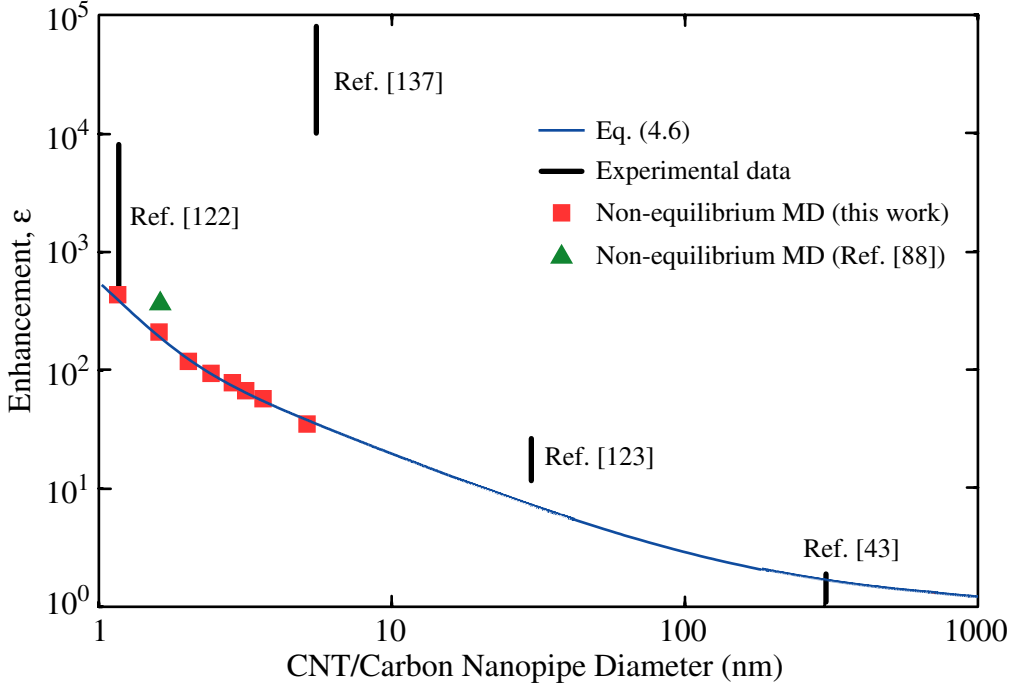


Figure 4.7: Comparison between the enhancement predicted from non-equilibrium MD simulation, the enhancement predicted using Eq. 4.6, and the enhancement measured during experiment.

with tube diameter—not described accurately using currently available LJ potential parameterizations—may account for some of the discrepancy. We also note that the calculated flow enhancement is sensitive to the CNT diameter. For example, a 0.1 nm mis-measurement of the mean CNT radius [used to calculate  $Q_N$  in Eq. (4.4)] will alter the experimentally measured enhancement range for the membrane of Holt et al. by 30%.

The predictions from our MD simulations do not support the  $10^4$  to  $10^5$  enhancement measurements of Majumder et al. for a membrane of 7 nm diameter CNTs. Our results suggest an enhancement factor of only 32 for such CNTs. Some discrepancy may arise from differences in CNT surface chemistry/structure or limitations in the MD potential functions. The exceptionally large flow enhancement reported by Majumder et al., however, suggest to us a miscalculation of either the mean CNT diameter or the density of open-ended CNTs in their membrane. As discussed in

Sec. 4.3, Majumder et al. estimate the diameter of the CNT pores by measuring the diffusion rate of ions through the membrane. The non-uniform electric field near the open end of a CNT, however, will limit the ability for ions to enter the tube while allowing water molecules to pass freely [148]. If this restriction on ion entrance is not considered, the apparent diameter calculated from the ion diffusion rates will be smaller than the flow diameter available for water molecules. This diameter discrepancy would cause the calculated water flow enhancement to exceed the actual flow enhancement.

The apparent slip length calculated by Whitby et al. for 44 nm diameter carbon nanopipes is 110 nm to 220 nm, which is larger than the value of 30 nm we predict directly from MD simulation. Unlike like the graphitic CNTs investigated in our MD simulation, however, the walls of the 44 nm diameter carbon nanopipes are multi-layered and amorphous. Since the structure of the carbon surface has a pronounced effect on the water/carbon contact angle [149], changes in the water/carbon slip length with surface structure are also expected. Additionally, the LJ water-carbon potential function used in our MD simulation was parameterized to reproduce the wetting characteristics of water on a flat graphitic surface. Variations in the carbon atom electrostatic multipoles (caused by the non-uniform distribution of carbon atoms) will not be captured using current potential functions and may affect transport through the nanopipe.

An additional factor that may influence water transport through 44 nm diameter carbon nanopipes is the Fakier effect, where water only interacts with the asperities along the carbon surface and does not fully penetrate through the surface roughness [150]. The Fakier effect reduces the liquid-solid contact area, causing a decrease in the flow friction (relative to Poiseuille flow), and an increase in the apparent liquid

slippage. For water flow over rough surfaces, the Fakier effect has been experimentally shown to increase the apparent slip length by one order of magnitude [150]. Flow enhancement may also be caused by air entrainment, where a low-viscosity gaseous layer near the solid surface entrains the liquid and increases the mean flow velocity. For example, the apparent slip length in water-filled 300-500 nm diameter carbon nanopipes is approximately zero [137]. Entrainment, however, can increase the apparent water/carbon slip length to the order of 100 nm [137].

For CNTs with diameter larger than 200 nm, predictions from MD simulation suggest that the effects of liquid slip are negligible and the viscosity of the liquid will be equal to that of the bulk liquid. This conclusion is consistent with measurements of water and glycerine flow through similarly sized carbon nanopipes, which are inline with predictions from the no-slip Poiseuille relation [126, 137]. Depending on the scale of the carbon nanopipe surface roughness, however, the Fakier effect and air entrainment are possible mechanisms by which the flow rate through these larger carbon nanopipes could be enhanced.

#### 4.8 Conclusion and outlook

In parallel with experimental investigations, MD simulation can be an effective tool for investigating the behavior of water near carbon surfaces and exploring the nature of water flow through CNTs and carbon nanopipes. Predictions from MD simulation indicate that (i) a continuum description of water flow is appropriate inside CNTs larger than 1.66 nm, (ii) diameter-related changes to the viscosity and slip length must be considered when modeling liquid flow, and (iii) the flow enhancement factor decreases monotonically with increasing diameter for smooth walled tubes. The variation in flow enhancement predicted using MD is qualitatively consistent with

the majority of the experimental data. Since the MD simulations considered flow through atomically smooth and defect-free CNTs, discrepancies between simulation and experiment are likely caused by differences in the structure and/or chemistry of the carbon surface.

Additional measurements of water flow through CNTs and carbon nanopipes are required to further understand the magnitude of the flow enhancement and its variation with CNT diameter. Better characterization of CNT and carbon nanopipe surfaces will also help to elucidate the effects of surface structure and surface chemistry on flow. Physically accurate potential functions and simulations utilizing more sophisticated water models are also needed to more fully understand the mechanisms of water flow through smaller CNTs. These additional insights into the physics of nanoscale flows, coupled with new device fabrication processes, will be central to the design and optimization of next-generation nanofluidic devices.

## CHAPTER V

### Subcontinuum water flow in carbon nanotubes

#### 5.1 Introduction

As discussed in Chapter I, an important step towards understanding liquid flow in nanoscale systems is to predict the transition from continuum to subcontinuum transport as the flow area decreases. In a continuum system, the behavior of a liquid is typically described in terms of infinitesimal volumetric elements that are small compared to the flow domain but have well-defined thermophysical properties. Applying Newton’s second law to a system of volumetric elements gives rise to the Cauchy and Navier-Stokes equations, which can be used to derive the Poiseuille and other continuum-level flow relations [151]. In a system where the size of a fluid molecule is comparable to the size of the flow domain, however, the notion of a representative volumetric element is invalid and the applicability of continuum-based relations is questionable. Within such subcontinuum systems, the movement of individual molecules and their structure must be considered when developing flow relations and predicting mass and momentum transport [129].

In Chapter IV, we used MD simulation to investigate liquid water flow through armchair CNTs with diameters ranging from 1.66 nm to 4.98 nm [63]. Accounting for confinement-induced changes to the water viscosity and variations in the wa-

ter/carbon slip length with tube diameter, we found that water flow through each CNT could be described using the slip-modified Poiseuille relation. This finding is consistent with the hypothesis that liquid flow can be described using continuum relations when the characteristic flow dimension is ten times larger than the size of the liquid molecule [133] ( $\approx 0.17$  nm for water). In CNTs with diameters smaller than 1.5 nm, where this criterion is not satisfied for water, a subcontinuum description of flow may be necessary.

In this chapter, we use MD simulation to examine pressure-driven water flow through 75 nm- and 150 nm-long armchair CNTs with diameters ranging from 0.83 nm to 1.66 nm. These CNTs are much longer than those examined in previous investigations, which had lengths and diameters of comparable magnitude [39]. We begin by quantifying the relationship between pressure gradient and average flow velocity for each CNT and then identify the transition to subcontinuum water flow. Next, we predict the liquid structure inside each CNT and correlate the structure to molecular transport. For subcontinuum systems we find that the liquid structure relaxation time, which we define as the time required for a water molecule to become uncorrelated from an initial structural arrangement, exceeds a time scale characteristic of the flow. This behavior leads to coordinated molecular transport inside the CNT and a non-monotonic relationship between CNT diameter and average flow velocity. These trends contrast flow in continuum systems, where the structure relaxation time is ephemeral compared to the flow time scale and the average flow velocity increases with increasing CNT diameter. We find that the subcontinuum liquid structure is long-ranged, and discuss how the relationship between pressure gradient and flow velocity will depend on tube length for CNT fragments shorter than about ten nanometers.

## 5.2 Background

The average flow velocity,  $\bar{v}$ , of an incompressible, creeping liquid (Reynolds number much less than one) inside a tube with a uniform cross-sectional area is given by the Darcy law:

$$\bar{v} = \gamma \left( \frac{\Delta P}{L} \right), \quad (5.1)$$

where  $\Delta P$  is the pressure difference across the tube,  $L$  is its length, and  $\gamma$  is a proportionality coefficient called the hydraulic conductivity [151]. Although the Darcy law is an empirical expression, the hydraulic conductivity of a Newtonian liquid in a circular tube subject to the no-slip boundary condition,  $\gamma_{\text{no-slip}}$ , can be found directly from the no-slip Poiseuille relation [25]:

$$\gamma_{\text{no-slip}} = \frac{D^2}{32\mu}, \quad (5.2)$$

where  $D$  is the tube diameter and  $\mu$  is the liquid viscosity.

Liquid slip at the solid-liquid boundary, confinement-induced reductions in the liquid viscosity, and subcontinuum changes to the liquid structure can all cause the actual hydraulic conductivity ( $\gamma_{\text{actual}}$ , as measured from experiment or predicted from MD simulation) to exceed that calculated from Eq. (5.2) [129]. This increase in  $\gamma$  has led to the definition of a flow enhancement factor,  $\varepsilon$  [43, 63, 122, 123]:

$$\varepsilon = \frac{\gamma_{\text{actual}}}{\gamma_{\text{no-slip}}}. \quad (5.3)$$

For CNTs with diameters larger than 1.6 nm, the variation in  $\varepsilon$  with CNT diameter can be understood in terms of slip at the water/CNT boundary and diameter-related changes to the water viscosity [63]. In CNTs with smaller diameters, however, water molecules have been shown to assemble into diameter-dependent one-dimensional structures for which neither the slip length nor the effective viscosity is well-defined

[129]. This confinement-induced change to the liquid structure introduces a coupling between the rotational and translational motion of the water molecules when subject to an electric field [152], modifies the phase diagram of the confined water [153], and alters the modes of mass diffusion inside the CNT [78]. The correlation between structure and pressure-driven flow, however, is not yet clear for these subcontinuum systems.

### 5.3 Simulation set-up

We simulate pressure-driven water flow through 0.83, 0.97, 1.10, 1.25, 1.39, and 1.66 nm-diameter single-walled armchair CNTs. A snapshot from a typical simulation, which consists of a water-filled CNT fragment connected to two water-filled reservoirs, is presented in Fig. 5.1. We use the TIP5P [76] water model and integrate the equations of motion using the Verlet leapfrog scheme with a 0.5 fs timestep. Interactions between the carbon atoms and the water molecules are modeled using the potential of Werder et al. [83]. Carbon nanotube fragments with lengths of 75 nm and 150 nm are considered and we keep the positions of the carbon atoms fixed with a 1.45 Å nearest-neighbor distance.

All simulations are performed in the *NVT* ensemble (constant number of particles, volume, and temperature) at a temperature of 298 K. The number of molecules in the system is chosen such that the water density in the reservoirs is 1000 kg/m<sup>3</sup> and the average number of water molecules in the CNT fragment is constant. As presented in Fig. 5.2(a), the CNT diameters examined here have water structures corresponding to single-file molecular chains (0.83 nm), tilted pentagonal rings (0.97 nm), stacked pentagonal rings (1.10 nm), stacked hexagonal rings (1.25 nm), and disordered bulk-like water (1.39 nm and 1.66 nm). The water structure and density we predict for

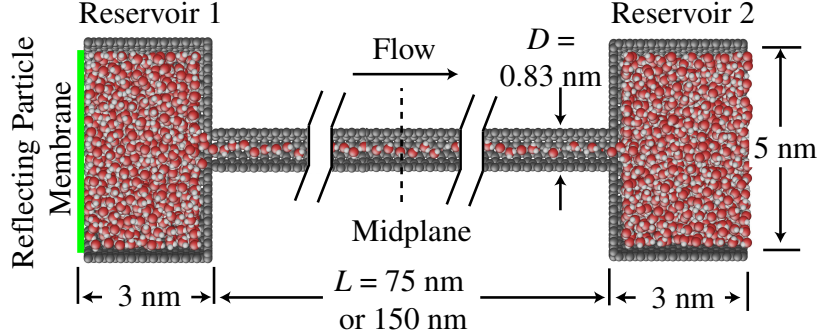


Figure 5.1: Snapshot from a typical flow simulation for the 0.83 nm-diameter CNT. A pressure difference between the reservoirs is established using a reflecting particle membrane and periodic boundary conditions are imposed in the flow direction. The number of molecules inside the CNT ranges from  $310 \pm 5$  for the 75 nm-long 0.83 nm-diameter CNT to  $3676 \pm 20$  for the 150 nm-long 1.66 nm-diameter CNT. Copyright 2009 American Physical Society.

each CNT are consistent with previous MD simulation results [154].

We create a pressure difference between the reservoirs,  $\Delta P$ , using a reflecting particle membrane that establishes a high pressure in Reservoir 1 and a low pressure in Reservoir 2 [63,133]. After a 0.25 ns initialization period, the mean pressure in each reservoir remains constant over the duration of the ensuing data collection period. We find that the pressure difference within each reservoir [ $O(0.1 \text{ MPa})$ ] is negligible compared to the pressure difference between the reservoirs [ $O(10 \text{ MPa})$ ]. We calculate the average flow velocity,  $\bar{v}$ , from the average axial velocity of all the molecules inside the CNT fragment. The average flow velocities are 1-7 m/s, a range that is well below the molecular thermal velocity (340 m/s at a temperature of 298 K). We also track the cumulative number of molecules crossing the CNT midplane,  $n(t)$ , during steady-state flow.

#### 5.4 Flow enhancement and liquid structure

In Fig. 5.3(a), we plot  $\bar{v}$  versus  $\Delta P/L$  for the 75 nm-long CNTs investigated here. Each point in Fig. 5.3(a) is the average of at least four independent 1 ns simulations. Consistent with Eq. (5.1), the average flow velocity for each CNT increases with

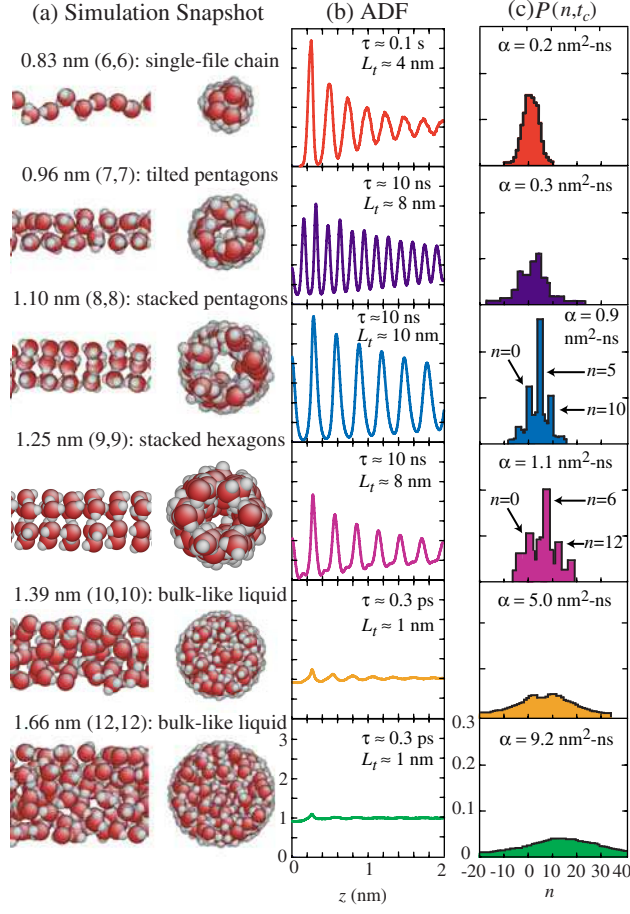


Figure 5.2: (a) Water structures inside the 0.83 nm- to 1.66 nm-diameter CNTs. Carbon atoms are removed for clarity and the chirality vector for each CNT is provided. (b) Axial distribution function (ADF), structure relaxation time  $\tau$ , and extent of the ADF,  $L_t$ , for each CNT. (c) Distribution of  $P(n, t_c)$ , the probability that  $n$  molecules cross the system midplane over the characteristic flow time  $t_c$ . The CNT permeability,  $\alpha$ , is shown for  $\Delta P/L = 4 \times 10^{14} \text{ Pa/m}$ . Copyright 2009 American Physical Society.

increasing pressure gradient. For a fixed value of  $\Delta P/L$ , however, the average flow velocity does not increase monotonically with CNT diameter, as would be predicted from Eqs. (5.1) and (5.2). Instead, when subject to the same pressure gradient, the average velocity decreases from the 0.83 nm CNT to the 1.10 nm CNT, is similar in the 1.10 nm and 1.25 nm CNTs, and then increases from the 1.25 nm CNT to the 1.66 nm CNT. As we will describe, this trend is related to the liquid structure inside each tube.

The non-linear relationship between  $\bar{v}$  and  $\Delta P/L$  in Fig. 5.3(a) is the result of in-

ertial losses (i.e., minor losses) at the two CNT/reservoir boundaries. Inertial losses are velocity-dependent and caused by sudden expansions, contractions and other obstacles in the flow field. The penalty associated with such losses,  $\Delta P_m(\bar{v})$ , can be incorporated into the Darcy law [151]:

$$\bar{v} = \gamma \left[ \frac{\Delta P - \Delta P_m(v)}{L} \right]. \quad (5.4)$$

Given the that the inertial losses are unknown, the hydraulic conductivity can be extracted from Eq. (5.4) as follows: Consider a long CNT with length  $L_l$ , and a shorter CNT with length  $L_s$ , with identical diameters and connected to identical reservoirs. Let the ratio of length to diameter for both tubes be large such that the entrance and exit effects are decoupled. If both systems have the same average flow velocity, the inertial losses in each system will be the same. However, due to additional frictional flow resistance in the longer CNT, the total pressure drop across it,  $\Delta P_l$ , will exceed that across the short CNT,  $\Delta P_s$ . Applying Eq. (5.4) to both systems and eliminating  $\Delta P_m(\bar{v})$  gives:

$$\gamma = \bar{v} \left( \frac{L_l - L_s}{\Delta P_l - \Delta P_s} \right). \quad (5.5)$$

The flow enhancement can then be specified using Eq. (5.3). For the 1.66 nm-diameter CNT, the enhancement calculated using Eq. (5.5) is within 17% of the value we predicted in Chapter IV, which was free of reservoirs and had no inertial losses. We estimate the uncertainty in  $\gamma$  to be  $\pm 25\%$  from the measured variances in  $\bar{v}$  and  $\Delta P_l - \Delta P_s$ . We find that, within this prediction uncertainty,  $\gamma$  is invariant over the flow velocities considered.

In Fig. 5.3(b), we present the variation of  $\varepsilon$  with CNT diameter. We also include the enhancement values for the 1.66 nm- to 3.33 nm-diameter CNTs we reported in Chapter IV [63]. In CNTs with diameters larger than 1.66 nm, where a continuum

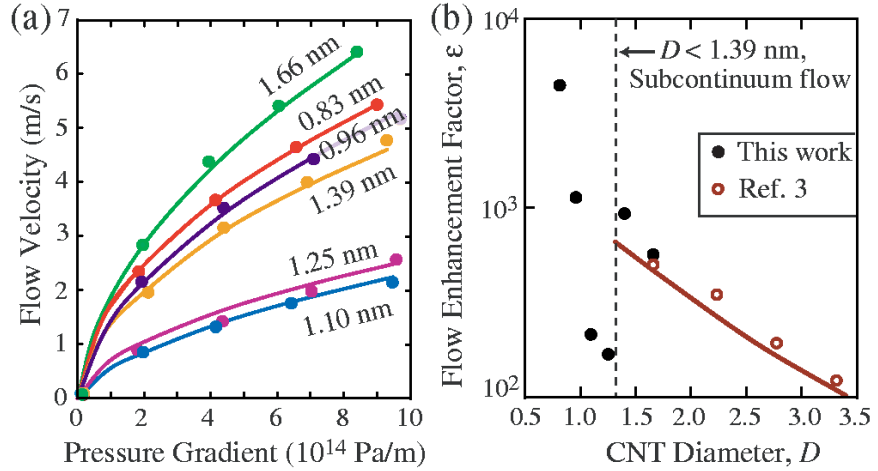


Figure 5.3: (a) Relationship between average flow velocity,  $\bar{v}$ , and applied pressure gradient,  $\Delta P/L$ , for the 75 nm-long CNTs. A similar relationship exists for the 150 nm-long CNTs. For each data point, the standard deviation in  $\bar{v}$  and  $\Delta P/L$  are  $0.5 \text{ m/s}$  and  $2 \times 10^{13} \text{ Pa/m}$ , leading to a  $\pm 25\%$  uncertainty in  $\varepsilon$ . Guidelines are added to highlight the trends. (b) Semi-log plot of the variation in flow enhancement factor,  $\varepsilon$ , with CNT diameter,  $D$ . The dashed line between  $D = 1.25 \text{ nm}$  and  $D = 1.39 \text{ nm}$  delineates continuum and subcontinuum flow regimes. The line in the continuum regime is a model we developed in Chapter IV. Copyright 2009 American Physical Society.

description of water flow is valid, we found that  $\varepsilon$  increased monotonically with decreasing CNT diameter. Here, we find that this trend extends to the 1.39 nm-diameter CNT. The abrupt reduction in flow enhancement between the 1.39 nm- and 1.25 nm-diameter CNT suggests a transition to subcontinuum transport, which is consistent with the change from disordered bulk-like water to one-dimensional structures with decreasing CNT diameter [see Fig. 5.2(a)]. The variation in flow enhancement within CNTs with diameters smaller than 1.25 nm cannot be described using continuum relations and, as we will show, is related to the water structure.

To quantify the variation in liquid structure with tube diameter, in Fig. 5.2(b) we present the axial distribution function (ADF) for water molecules inside each CNT. We define the ADF,  $a(z)$ , by:

$$\int_{z=0}^{z=\pm L} a(z) \frac{\pi D^2}{4} dz = N_t - 1 \simeq N_t, \quad (5.6)$$

where  $N_t$  is the number of water molecules between  $z = \pm L$ . Like the radial distribu-

tion function (RDF) [68], which describes the likelihood of finding a second molecule some radial (three-dimensional) distance away from an origin molecule, the ADF describes the likelihood of finding a second molecule some axial (one-dimensional) distance away from an origin molecule. For the finite-length CNTs investigated in this work, we calculate  $a(z)$  using origin molecules located within 25 nm of the system midplane.

In CNTs with diameters greater than 1.66 nm, the ADF has a small peak at  $z = 0.3$  nm and is invariant with CNT diameter. The position of this peak is similar to the position of the first peak in the RDF of bulk water [76]. The ADF inside the 1.39 nm-diameter CNT is comparable to that of larger tubes, suggesting that confinement induced changes to the liquid structure are insignificant in this CNT [32]. Inside the 1.25 nm- to 0.83 nm-diameter CNTs, where the layered and single-file molecular structures are present, the axial positions of the water molecules are strongly correlated and oscillations in the ADF extend 4 nm to 10 nm from the origin molecule. Such long-range positional correlation, which is not present in bulk water, is a distinguishing feature of subcontinuum fluids [129]. We find no difference between the ADFs in the 75 nm- and 150 nm-long CNTs, indicating that the ADFs predicted here are representative of infinitely-long CNTs.

In CNTs with diameters less than 1.39 nm and lengths shorter than about 10 nm, all the water molecules inside the tube will have correlated positions. Although the distinction between solid phase water and liquid phase water is unclear for such systems, we expect that the solid-like molecular structure will limit the mobility of individual molecules and lower the average flow velocity of water inside such short CNTs. This hypothesis is supported by the MD simulation data of Corry [39], who investigated pressure-driven water flow through CNT membranes with diameters sim-

ilar to those investigated here, but with lengths of 1.3 nm and 2.6 nm. The positions and movement of water molecules inside the short CNTs were indeed correlated and transport through the tubes occurred via collective bursts. Moreover, the flow enhancement factors we calculate from the Corry data are 1 to 10, a range lower than the 100 to 1000 range we predict here for 75 nm- and 150 nm-long CNTs. This result suggests that as the CNT length decreases below 10 nm and the molecules at the tube inlet become increasingly coupled to those at the tube outlet, mass transport will become less like flow through a pipe and more like coordinated diffusion through a two-dimensional pore. This transition will reduce the flow rate through the tube and cause a reduction in the flow enhancement factor.

## 5.5 Correlation between structure and flow

Although the CNTs investigated in this work are longer than the oscillations in their ADFs, the local liquid structure in each tube still governs molecular transport through it. This coupling between structure and flow can be identified by examining the cumulative midplane mass flux,  $n(t)$ . In Fig. 5.2(c), we present the probability  $P(n, t_c)$  that  $n$  molecules cross the CNT midplane over a characteristic flow time  $t_c$ . We define  $t_c$  from:

$$t_c = \frac{L_c}{\bar{v}}, \quad (5.7)$$

where  $L_c$  is a characteristic length scale and  $\bar{v}$  is the average flow velocity inside the CNT. We set  $L_c$  equal to the location of the first peak in the ADF and calculate  $P(n, t_c)$  for each flow simulation. Since the liquid structure does not vary with flow velocity (over the range considered here),  $P(n, t_c)$  for each CNT collapses onto a velocity-independent distribution. We note that with  $L_c \sim 0.17\text{-}0.3$  nm and  $\bar{v} \sim 1\text{-}7$  m/s,  $t_c$  is  $O(100$  ps).

Inside the 1.66 nm-diameter CNT (where flow can be modeled using continuum-based relations)  $P(n, t_c)$  is non-zero over a large range of  $n$ . This large range is accessible because the structure relaxation time, which we estimate to be 0.3 ps from the decay of the velocity autocorrelation function, is very small compared to  $t_c$ . The flow is therefore independent of liquid structure and a random number of molecules, subject to the distribution of  $P(n, t_c)$ , can cross the midplane during  $t_c$ . Although the accessible range of  $n$  increases with CNT diameter, we find that the shape of the  $P(n, t_c)$  distribution in larger CNTs is similar to what we report here for the 1.66 nm diameter tube and find no appreciable change in the structure relaxation time. This smooth distribution of  $P(n, t_c)$  is also present in the 1.39 nm-diameter CNT, further suggesting that the flow in this tube is independent of structure and a continuum description of mass flow will be appropriate.

Inside the 1.25 nm-diameter CNT,  $P(n, t_c)$  exhibits peaks at  $n = 6$  and  $n = 12$ . A similar distribution is present inside the 1.10 nm-diameter CNT, where  $P(n, t_c)$  exhibits peaks at  $n = 5$  and  $n = 10$ . These peaks, which are related to the stacked hexagonal and pentagonal rings in the tubes, indicate a coupling between structure and flow. The relaxation time of the layered water structure inside these CNTs, as estimated from MD simulation, is  $O(10 \text{ ns})$  [78, 152], indicating that water molecules may travel from the tube inlet to the tube outlet as members of a single layer. Unlike bulk-like systems, where water molecules can move independently, the transport of molecules in these structured subcontinuum systems is conditional upon the movement of nearby layers. A layer of water molecules that fills an energetically stable CNT surface site [62, 146] can therefore impede the movement of other layers. Such localized limitations on transport will reduce  $\bar{v}$  and lower the overall flow enhancement (see Fig. 5.3). This hypothesis is consistent with the findings of Kolesnikov et

al. [155] and Mamontov et al. [32], who demonstrate from neutron scattering experiments and MD simulation that the water molecules in layered structures have, on average, less mobility than water molecules in bulk-like water.

Between the 1.10 nm- and 0.83 nm-diameter CNTs, the liquid structure transitions from stacked pentagonal rings to tilted pentagonal rings and finally to a single-file molecular chain. With decreasing CNT diameter, we find that the effects of layer-by-layer transport become less prominent, the spatial extent of the ADF decreases [see Fig. 5.2(b)], and the average flow velocity increases for a given pressure gradient [see Fig. 5.3(a)]. Although the mass transport mechanisms within these tubes are not yet clear, in Chapter III we found that water molecules become less coupled to the CNT surface with decreasing CNT diameter [61]. This effect will reduce flow friction in smaller CNTs and may contribute to the increase in flow velocity with decreasing diameter. In the 0.83 nm-diameter CNT, where the single-file water structure relaxation time has been estimated to be  $O(0.1$  s) [156], the probability of two or more molecules crossing the midplane in either the positive or negative direction is 0.6. This behavior is the result of coordinated molecular motion inside the CNT. It confirms that, although the tube inlet and tube outlet are decoupled in our system, localized bursting still governs mass transport inside long length, small-diameter CNTs.

In Fig. 5.2(c), we also provide the molecular permeability,  $\alpha$ , of each CNT corresponding to a pressure gradient of  $4 \times 10^{14}$  Pa/m. The permeability describes the relationship between molecular flux and applied pressure gradient, and incorporates the effects of diameter-related changes to the flow area, water density, and flow velocity [151]. Despite the decrease in flow velocity from the 0.83 nm- to the 1.10 nm-diameter CNT, the permeability increases monotonically with CNT diameter for

all tubes. This trend arises from the fact that the cross-sectional flow area increases faster with diameter than the structure-related reductions in the flow velocity. For example, the average flow velocity in the 0.83 nm-diameter CNT is more than three times larger than that for the 1.39-nm diameter CNT, when subjected to the same pressure gradient. The permeability of the 1.39 nm-diameter CNT, however, is approximately five times larger.

## 5.6 Conclusions

We have investigated water flow through CNTs with diameters ranging from 0.83 nm to 1.66 nm. We quantified the flow enhancement factor inside each CNT and investigated the coupling between liquid structure and liquid flow. In CNTs with diameters greater than 1.39 nm, our results suggest that flow velocities will be in-line with predictions from continuum fluid mechanics. In CNTs with diameters smaller than 1.39 nm, the flow enhancement factor can be correlated to confinement-induced changes in liquid structure (i.e., the flow enters a subcontinuum regime). This behavior leads to a transition from slow-moving layered structures in the 1.25 nm- and 1.10 nm-diameter CNTs, to a faster moving tilted-layer structure in the 0.96 nm-diameter CNT, and finally to a single-file molecular chain in the 0.83 nm-diameter CNT. Since the structure of water inside a CNT may vary with temperature [155], the mean flow flow velocity inside a CNT will likely depend on the CNT membrane operating environment. The effects of CNT chirality and surface composition on liquid structure and flow, and possible interactions between the water molecules and the CNT vibrational modes [89] also warrant further exploration.

Although this work focused on water flow through CNTs, several trends can be extrapolated to the more general field of subcontinuum liquid transport. First, un-

like predictions from continuum mechanics, the flow enhancement in subcontinuum systems may not increase monotonically with decreasing flow area. Instead, when the flow area is comparable to the size of the fluid molecules, confinement-induced changes to the liquid structure may reduce the flow enhancement and must be considered. Second, if the system length is comparable to the particle correlation length, the fluid inlet and outlet are not independent and the hydraulic conductivity may depend on system length. Within very short systems, transport may therefore be less like flow through a pipe and more like coordinated diffusion through a two-dimensional pore. Third, liquid structure and liquid flow are independent in systems where the characteristic flow time scale is much longer than the structure relaxation time. These scales must be considered when comparing results from different flow investigations and examining flow/structure interactions. Finally, due to the small flow cross-section, large flow enhancements in small diameter systems may not correlate to a large membrane permeability. Changes in the liquid density and cross-sectional flow area must also be considered.

## CHAPTER VI

### Thermal conductivity of empty and water-filled carbon nanotubes

#### 6.1 Introduction

In addition to their use as nanofluidic devices, the high thermal conductivities of CNTs measured experimentally [44, 45, 157, 158] and predicted from theory [159–162] have generated interest in CNT-based thermal management materials. Most investigations of thermal transport in these materials, however, have focused on their behavior in vacuum. As components of a thermal management device, the atoms in CNTs will exchange energy with atoms and molecules in an adjacent liquid or gas. Results from earlier investigations indicate that the low interaction energy between solid-phase carbon atoms and non-bonded fluid molecules [57, 85] gives rise to velocity slip at the solid/liquid boundary [43, 63, 65, 122] and a large interfacial thermal resistance between CNTs and an adjacent fluid [54, 163–165]. What remains unclear, however, is how interactions with fluid molecules influence thermal transport in CNTs and modify their thermal conductivities. Understanding how interactions with non-bonded atoms modify phonon transport in a CNT is an important next step in predicting how CNT-based materials will behave in heat transfer applications.

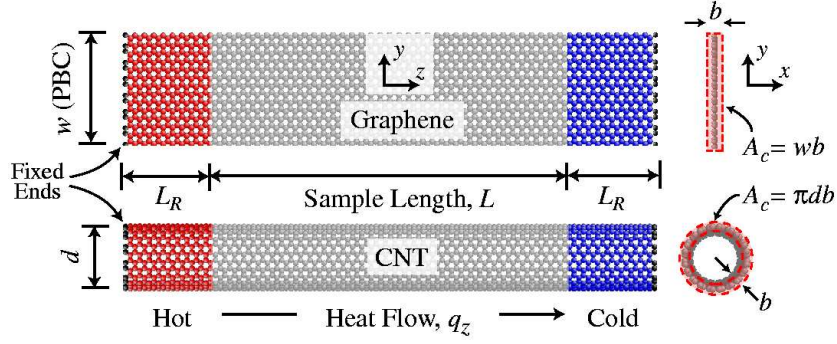


Figure 6.1: Simulation set-up used to predict graphene and CNT thermal conductivities. The dashed lines identify the cross-sectional area,  $A_c$ . The heat flow is introduced by transferring energy from the carbon atoms in the cold reservoir to those in the hot reservoir. The differently-colored carbon atoms are used to distinguish the reservoirs from the sample. The reservoir length,  $L_R$ , is 50 nm and the atoms at the ends of the systems are frozen to prevent sublimation. Periodic boundary conditions (PBC) are applied in the graphene  $y$  direction. Copyright 2010 American Physical Society.

Thermal conductivity,  $\mathbf{k}$ , is a second-order tensor defined by the Fourier law:

$$\mathbf{q}'' = -\mathbf{k}\nabla T, \quad (6.1)$$

where  $\mathbf{q}''$  is the heat flux vector and  $\nabla T$  is the spatial temperature gradient. Although defined by this empirical expression, the thermal conductivity of a solid is directly related to the mobility of electrons and phonons. Electronic contributions to the CNT thermal conductivity are generally considered to be negligible [166, 167]. Instead, the high thermal conductivities of CNTs have been attributed to the long phonon mean-free paths associated with low-dimensional (1-D or 2-D) crystals [168].

For single-walled CNTs with diameters smaller than 1 nm and lengths shorter than  $O(100 \text{ nm})$ , most thermal energy is transported ballistically by acoustic phonons that scatter at the ends of the CNT [169]. Within this ballistic transport regime, the effective thermal conductivity increases with increasing CNT length as the effects of boundary scattering decrease and additional long-wavelength phonon modes become accessible [169]. Our use of the term “effective thermal conductivity” emphasizes that the ballistic modes contributing to the heat flux do not follow the Fourier law [161]. As the CNT length is increased beyond  $O(100 \text{ nm})$ , an increasing fraction of

phonons scatter with other phonons before reaching the ends of the CNT [168, 170]. Eventually, with increasing CNT length, the phonon transport becomes fully-diffusive and the thermal conductivity becomes length-independent as contributions to thermal transport from ballistic modes become negligible [171]. The specifics of how this fully-diffusive thermal conductivity varies with CNT diameter and how interactions with non-bonded molecules influence this transition are not yet clear [89].

In this chapter, we use MD simulation to investigate the fully-diffusive thermal conductivity of empty and water-filled single-walled CNTs. We begin by describing our simulation methodology and thermal conductivity prediction procedure. Next, we investigate the variation in thermal conductivity for 200 nm- to 1400 nm-long CNTs and flat graphene sheets, which can be viewed as infinite-diameter single-walled CNTs. For empty CNTs, we find that the fully-diffusive thermal conductivity and the length required to obtain fully-diffusive phonon transport both decrease with increasing CNT diameter. We attribute this behavior to the increase in acoustic phonon scattering events caused by the larger number of optical phonon modes that exist in larger diameter CNTs. We find that the magnitude of the fully-diffusive thermal conductivity of water-filled CNTs is 20% to 35% lower than that of the empty CNTs and that the transition to fully-diffusive transport occurs at shorter lengths. By comparing the carbon atom density of states (DOS) of empty and water-filled CNTs, we demonstrate that the thermal conductivity reduction is related to the overlap between the vibrational frequencies accessible to the water molecules and the low-frequency acoustic phonon modes in the CNTs.

## 6.2 Simulation set-up

We simulate thermal transport through empty and water-filled 0.83 nm-, 1.10 nm-, and 1.36 nm-diameter CNTs [chirality vectors of (6,6), (8,8) and (10,10)] and an isolated graphene sheet. As illustrated in Fig. 6.1, we define the cross-sectional area of the CNTs to be  $A_c = \pi db$ , where  $b (= 0.34 \text{ nm})$  is the van der Waals thickness of the CNT surface and  $d$  is the CNT diameter [171–173]. We fix one layer of carbon atoms at the ends of the CNT to prevent atoms from sublimating. For graphene, we define the cross-sectional area to be  $A_c = wb$ , where  $w$  is the width of the sheet (see Fig. 6.1). We fix the atoms at the end of the graphene sheet and apply periodic boundary conditions in the  $y$  direction. These simulations are thus representative of an infinite graphene sheet and not the graphene nanoribbons studied by others [171, 174]. We note that the systems investigated here are longer than the 10 nm- to 400 nm-long systems typically investigated using MD simulation, as summarized by Mingo and Briodo [169] and Lukes and Zhong [172].

The number of carbon atoms in the CNT ranges from 29,232 (for the 200 nm-long, 0.83 nm-diameter CNT) to 195,120 (for the 1200 nm-long, 1.10 nm-diameter CNT) and the equilibrium nearest-neighbor distance is 1.42 Å [38]. Interactions between carbon atoms are modeled using the second-generation REBO potential [87] and the water/carbon interactions are modeled using the LJ potential of Werder et al. [83]. Interactions between water molecules are modeled using the TIP4P/2005 potential, which has been shown to reproduce the structure of water clusters more accurately than the TIP5P potential [175]. Electrostatic interactions between water molecules are modeled using the Wolf sum [99, 176]. We integrate the equations of motion using a velocity Verlet scheme with a 0.5 fs time step and model the rotational dynamics

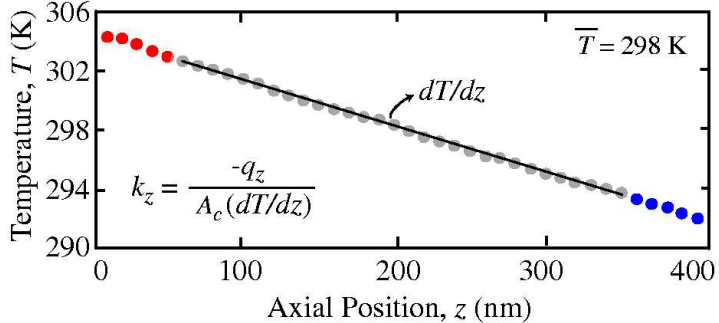


Figure 6.2: Typical temperature gradient obtained from MD simulation. The thermal conductivity is obtained using Eq. (6.2). The data here correspond to the 1.36 nm-diameter CNT. The temperature gradient in this trial was  $29.5 \pm 1.12 \text{ K}/\mu\text{m}$  (i.e., 3.8% uncertainty) and the heat flow is 15 nW. The uncertainty represents the 95% confidence interval of the linear regression. Copyright 2010 American Physical Society.

of the water molecules using the quaternion method [68, 177].

We fill the CNT according to the equilibrium water density, determined by simulating an open-ended sample of each CNT in a liquid water reservoir at a temperature of 298 K and a pressure of 1 atm. Water molecules were able to freely diffuse across the open ends of the CNT and the density of the water in the reservoir was maintained at  $1000 \text{ kg/m}^3$ . After a 250 ps initialization period, the average number of molecules enclosed in the CNT became steady, allowing us to determine the equilibrium water density. The water molecules assemble into a single-file molecular chain (0.83 nm-diameter CNT), stacked pentagonal rings (1.10 nm), or a disordered bulk-like liquid (1.36 nm) [65]. As discussed in Chapter V, the molecular positional correlations for the chain and ring liquid structures extend 5 nm to 10 nm and the structure relaxation times predicted from theory are between 1 ns and 1 ms [65]. These values are much larger than that the 1 nm position correlation length and 0.5 ps structure relaxation time of bulk water [178].

We predict the effective axial thermal conductivity,  $k_z$ , of the CNTs and graphene using a one-dimensional form of the Fourier law:

$$q_z = -k_z A_c \frac{dT}{dz}, \quad (6.2)$$

where  $q_z$  is the heat flow in the  $z$  direction and  $dT/dz$  is the temperature gradient. As shown in Fig. 6.1, we introduce a heat flow by transferring a known and constant quantity of kinetic energy from carbon atoms in the cold reservoir to those in the hot reservoir at each simulation time step [179, 180]. The total energy of the simulation cell remains constant and corresponds to an average temperature of 298 K. In response to the energy redistribution, however, thermal energy moves from the hot reservoir to the cold reservoir and a temperature gradient is established in the system. We use reservoir lengths of 50 nm and find that increasing this length has no detectable effect on the predicted thermal conductivity. For graphene, we find that a sample width of 5 nm is sufficient to eliminate width-related size-effects when predicting  $k_z$ .

Each simulation consists of a 10 ns equilibration period (after which the systems reach a steady-state), followed by a 10 ns data collection and averaging period. As depicted in Fig. 6.2, we specify  $dT/dz$  by calculating the temperature of the carbon atoms within 40 sub-volumes (i.e., bins) along the sample during the data collection period. Our imposed heat flow of 15 nW introduces a temperature gradient between 25 K/ $\mu\text{m}$  and 80 K/ $\mu\text{m}$  (depending on the system length and cross-sectional area). The temperature within each bin is related to the average kinetic energy of the carbon atoms. Thus, with increasing CNT diameter and length, a larger number of carbon atoms are in each bin and the uncertainty in the temperature gradient decreases from 10% in the empty 200 nm-long 0.83 nm-diameter CNT to less than 2% in the empty 1200 nm-long 1.10 nm-diameter CNT. The uncertainty in the temperature gradient for all the water-filled CNTs is less than 2%. Consistent with systems in a linear-response regime, we find that the predicted thermal conductivity is not affected by small changes in the magnitude of the heat flow.

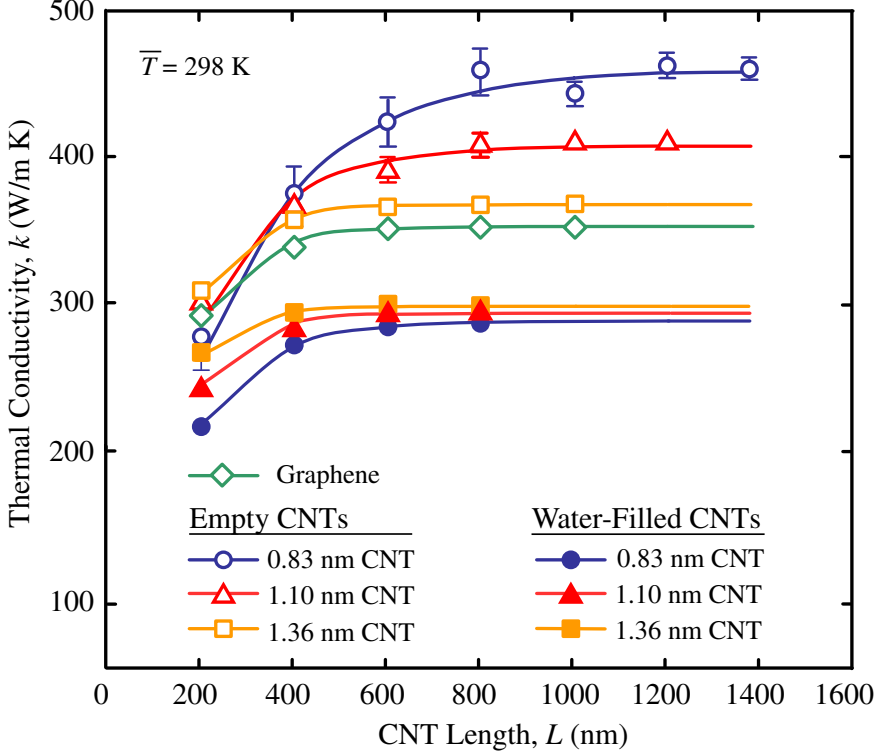


Figure 6.3: Variation in thermal conductivity with length for empty CNTs, water-filled CNTs, and graphene. The diameter of each CNT is given in the legend and each data set is fit to Eq. (6.3). The error bars for  $k_z$  are associated with uncertainty in specifying  $dT/dz$ . For points without error bars, the uncertainty in the thermal conductivity is comparable to the size of the data point. Copyright 2010 American Physical Society.

### 6.3 Empty CNT thermal conductivity

In Fig. 6.3, we present the variation in thermal conductivity with length for the empty 0.83 nm-, 1.10 nm-, and 1.36 nm-diameter CNTs and for graphene. From this data, we observe the transition from a regime where the thermal conductivity is length-dependent to a regime where it is length-independent and the phonon transport is fully-diffusive. To quantify the transition from ballistic to diffusive phonon transport, we fit the thermal conductivity data to the empirical function

$$k_z = k_{z,\infty} \left[ 1 - \exp \left( -\frac{L}{L_c} \right) \right], \quad (6.3)$$

where  $k_{z,\infty}$  is the fit fully-diffusive thermal conductivity,  $L$  is the sample length, and  $L_c$  is a fit length that describes the transition. We define the quantity  $L_{99}$  to be the

length at which  $k_z = 0.99k_{z,\infty}$ , such that

$$L_{99} \equiv \ln(100)L_c = 4.605L_c. \quad (6.4)$$

Another procedure for extracting  $k_{z,\infty}$ , as proposed by Schelling et al. [181], incorporates the effects of boundary scattering into the phonon mean-free path using the Matthiessen rule [182]. The Matthiessen rule, when combined with the kinetic theory expression for thermal conductivity [183], predicts that  $1/k_z$  will be linearly related to  $1/L$ , such that finite-size effects can be eliminated using a linear extrapolation (e.g.,  $1/L \rightarrow 0$ ). Although this procedure has been successfully applied to three-dimensional solid systems [180,181,184], the relationship between  $1/k_z$  and  $1/L$  for the CNTs considered here is non-linear. A direct extrapolation to an infinite system length is therefore not possible. We hypothesize that the primary reason for this breakdown of the linear extrapolation procedure is the assumption of a single phonon mean-free path in the kinetic theory expression for thermal conductivity [34]. This approximation, which assumes that every phonon travels the same distance on average before scattering, is poor for CNTs and graphene, where the low-frequency acoustic phonon modes have mean-free paths several orders-of-magnitude larger than those of the other acoustic modes [159].

In Figs. 6.4(a) and 6.4(b) we present the variation in  $k_{z,\infty}$  and  $L_{99}$  with the inverse of the CNT diameter. Included in the plots are additional  $k_{z,\infty}$  values for empty 1.63 nm and 2.17 nm-diameter CNTs that we predict from simulations of 600 nm-long samples. Based on the  $L_{99}$  values for the 1.36 nm-diameter CNT and for graphene, we believe that the thermal conductivities predicted from simulations of 600 nm-long 1.63 nm- and 2.17 nm-diameter CNTs represent the fully-diffusive thermal conductivity. For the empty CNTs, we find that both  $k_{z,\infty}$  and  $L_{99}$  decrease with increasing

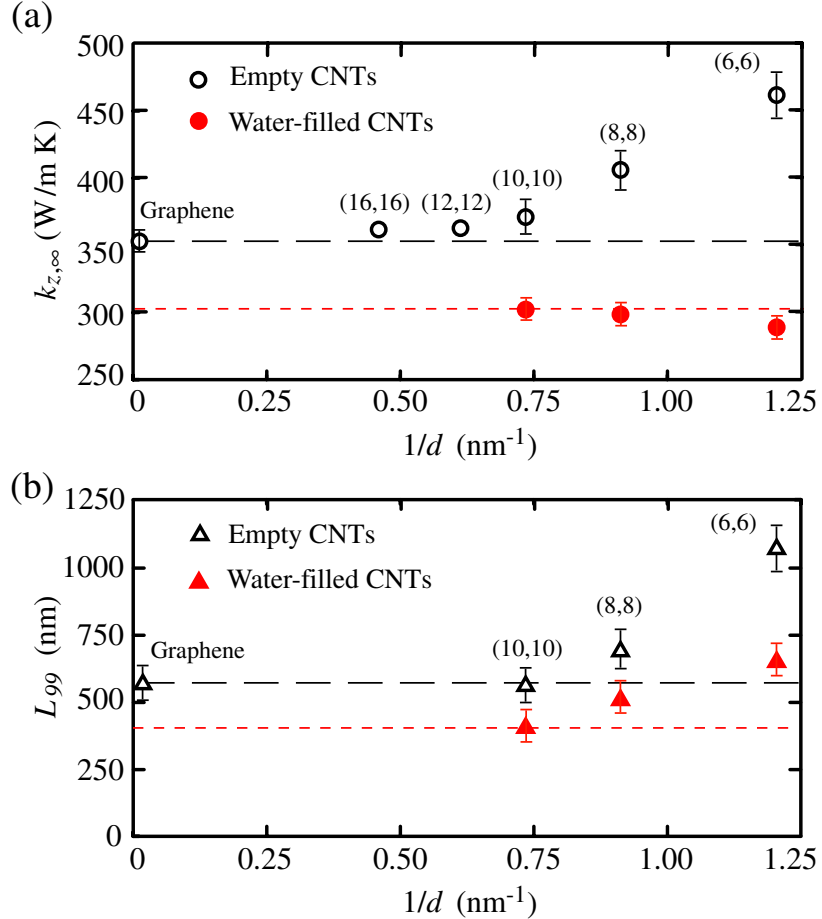


Figure 6.4: Variation in (a)  $k_{z,\infty}$  and (b)  $L_99$  with the inverse of diameter for empty and water-filled CNTs. The chirality vectors for each CNT are used to label the data points. We also include  $k_{z,\infty}$  for empty 1.63 nm-diameter ( $1/d=0.61$  nm $^{-1}$ ) and 2.17 nm-diameter ( $1/d=0.46$  nm $^{-1}$ ) CNTs, which are predicted using a 600 nm-long CNT sample. The horizontal long-dashed lines indicate  $k_{z,\infty}$  and  $L_99$  for the flat graphene sheet ( $1/d=0$ ). The horizontal short-dashed lines indicate our estimated values for  $k_{z,\infty}$  and  $L_99$  for water/graphene systems based on analysis of the CNT density of states (see Sec. 6.4). The error bars indicate the standard error calculated from a regression analysis of Eq. (6.3). Copyright 2010 American Physical Society.

CNT diameter and approach the value we predict for graphene. To understand this behavior, note that the high thermal conductivity of CNTs is related to the long-wavelength acoustic phonon modes accessible to the system [168]. With increasing CNT diameter, the number of acoustic phonon modes does not change but new optical phonon modes are created due to the increased number of atoms in the unit cells of larger-diameter CNTs. Since the optical phonons in CNTs typically have small mean-free paths, their mode-by-mode contributions to thermal conductivity are small [30].

As suggested by the Fermi golden rule for phonon scattering [185], however, the additional optical modes in larger-diameter CNTs introduce additional multi-phonon scattering channels that shorten the acoustic-phonon mean-free paths [56,186]. These additional interactions lower the fully-diffusive thermal conductivity in the larger-diameter CNTs and, due to the shorter acoustic phonon mean-free paths, shorten the CNT length required to obtain fully-diffusive transport [187].

The data presented in Figs. 6.4(a) and 6.4(b) are consistent with the MD simulation results of Shiomi and Maruyama, who, also using the REBO potential, found that  $k_z$  for a 1000 nm-long, 0.41 nm-diameter CNTs is higher than that for a 0.68 nm-diameter CNTs with the same length [171]. Our predicted fully-diffusive thermal conductivity of 355 W/m-K for the 1.36 nm-diameter CNT is consistent with the MD simulation predictions of Padgett and Brenner [173], who modeled the same CNT using the REBO potential and predicted a fully-diffusive thermal conductivity of 350 W/m-K. We note that the thermal conductivities of graphitic materials predicted using the REBO potential are lower than those measured from experiments, which range from 2,000 W/m-K to 10,000 W/m-K [44, 45, 172, 188]. This behavior is in contrast to the Tersoff potential [189], which tends to overestimate the thermal conductivity of graphitic materials [159]. Our predictions from anharmonic lattice dynamics calculations indicate that a fully quantum mechanical treatment of the phonon transport in our CNTs at a temperature of 298 K changes the magnitude of the fully-diffusive thermal conductivity by less than 5% [190].

#### 6.4 Water-filled CNT thermal conductivity

We predict the thermal conductivity of water-filled CNTs using the same heat flux method used to investigate empty CNTs. The water-filled CNTs are filled with

the number of water molecules corresponding to the equilibrium density and span the entire simulation cell. No water is present outside the CNT. After the 10 ns equilibration period, we find that the axial temperature profiles in the CNT and in the water are identical. This expected steady-state condition implies that the net energy transfer between the two materials is zero but that thermal energy will be transferred from the hot reservoir to the cold reservoir through both materials. Our preliminary investigations indicate that the thermal conductivity of the ordered water in these CNT is approximately 1 W/m-K [191,192]. Since the water and CNTs in our study have comparable cross-sectional areas, the relationship between their thermal conductivities implies that a negligible fraction of the total heat transfer through the composite occurs through the water (i.e., the water has a negligible thermal conductance). As discussed below, however, interactions between the carbon atoms and the water molecules influence phonon transport in the CNT and cannot be ignored.

In Fig. 6.3, we compare the thermal conductivities of the water-filled CNTs to those of the empty CNTs. Although simulating longer water-filled CNTs is computational impractical, the data presented here are sufficient to illustrate the transition to fully-diffusive transport. We calculate  $k_{z,\infty}$  and  $L_{99}$  using Eqs. (6.3) and (6.4) and report these values in Figs. 6.4(a) and 6.4(b). Three trends are apparent: First, the fully-diffusive thermal conductivities of the water-filled CNTs are 20% to 35% lower than those of the empty CNTs. Second, the CNT length required to obtain fully-diffusive thermal transport in water-filled CNTs is shorter than that required for empty CNTs. Third, unlike in empty CNTs, where the fully-diffusive thermal conductivity decreases with increasing diameter, the thermal conductivity of the water-filled 0.83 nm-diameter CNT is lower than that of the water-filled 1.36 nm- and 1.10 nm-

diameter CNTs (which are the same to within the prediction uncertainty).

To understand the mechanisms responsible for these trends, we plot in Fig. 6.5(a) the DOS for carbon atoms in the empty 1.10 nm-diameter CNT predicted from the Fourier transform of the carbon atom velocity autocorrelation function [193]. The DOS was obtained from equilibrium simulation (no heat flux) of a 200 nm-long CNT fragment with fixed ends at a temperature of 298 K in the microcanonical ensemble. The same DOS is predicted from simulations using a periodic boundary condition in the axial direction. For both the fixed-end and periodic systems, we find that increasing the CNT length does not change the position or relative magnitudes of the peaks in the DOS. The DOS for the empty 0.83 nm- and 1.36 nm-diameter CNTs are similar to that for the 1.10 nm-diameter CNT, although the larger number of optical modes in the larger-diameter CNTs cause the number of frequency peaks to increase with increasing diameter. As discussed by others [159, 168, 169], a large part of the CNT thermal conductivity comes from the acoustic phonon modes. An inspection of CNT dispersion curves [36, 166] indicates that these acoustic modes have frequencies less than 120 rad/ps.

In Fig. 6.5(b), we plot the vibrational spectrum accessed by the water molecules inside each CNT. This spectrum is calculated from the Fourier transform of the water molecule velocity autocorrelation function. The vibrational spectra for water inside the 1.36 nm- and 1.10 nm-diameter CNTs are both similar to that of bulk water and indicate that the molecules inside the CNT vibrate primarily with frequencies below 60 rad/ps. Inside the 0.83 nm-diameter CNT, where water molecules assemble into a one-dimensional hydrogen-bonded water wire, the range of accessible frequencies extends up to 100 rad/ps. We believe that the extended range of frequencies accessible to these water molecules is related to the stability and correspondingly

long structure relaxation time ( $\sim 1$  ms) of the water-wire [156].

In Fig. 6.5(c), we compare the low-frequency DOS for carbon atoms in the empty 1.10 nm-diameter CNT to what we predict for the water-filled 1.10 nm-diameter CNT. Changes in the DOS are particularly evident in the sub-40 rad/ps frequency range, where peaks present in the empty CNT DOS are missing from the water-filled CNT DOS. As shown in Fig. 6.5(b), this frequency range is highly populated by the water molecules inside the CNT, suggesting that collisions between water molecules and the carbon surface scatter the low-frequency acoustic phonons traveling through the CNT. As the magnitude of the water molecule spectrum decreases with increasing frequency, the DOS for carbon atoms in the empty and water-filled CNTs converge. This finding is consistent with theoretical investigations into heat transfer across a CNT/liquid octane interface, which indicate that liquid polymers exchange energy primarily with CNT phonon modes with comparable vibrational frequencies [163,164].

By definition, the area under the CNT DOS is equal to the total number of phonon modes accessible to the carbon atoms. This number is the same for both the empty and water-filled CNTs, meaning that the missing peaks in the water-filled CNT DOS indicate a broadening (but not elimination) of the phonon modes accessible to the empty CNTs. Molecular dynamics-based investigations of thermal boundary resistance between CNTs and liquid or solid argon indicate that this broadening is primarily caused by phonon linewidth collision-broadening [194]. This behavior is explained as follows: The phonon linewidth, which is inversely proportional to the phonon relaxation time, describes how the actual atomic vibrational frequencies deviate from the non-interacting normal modes of vibration. In empty CNTs, the phonon linewidth is related to the number of phonon-phonon scattering interactions that arise from anharmonicities in the potential energy landscape [195]. In water-filled CNTs, inter-

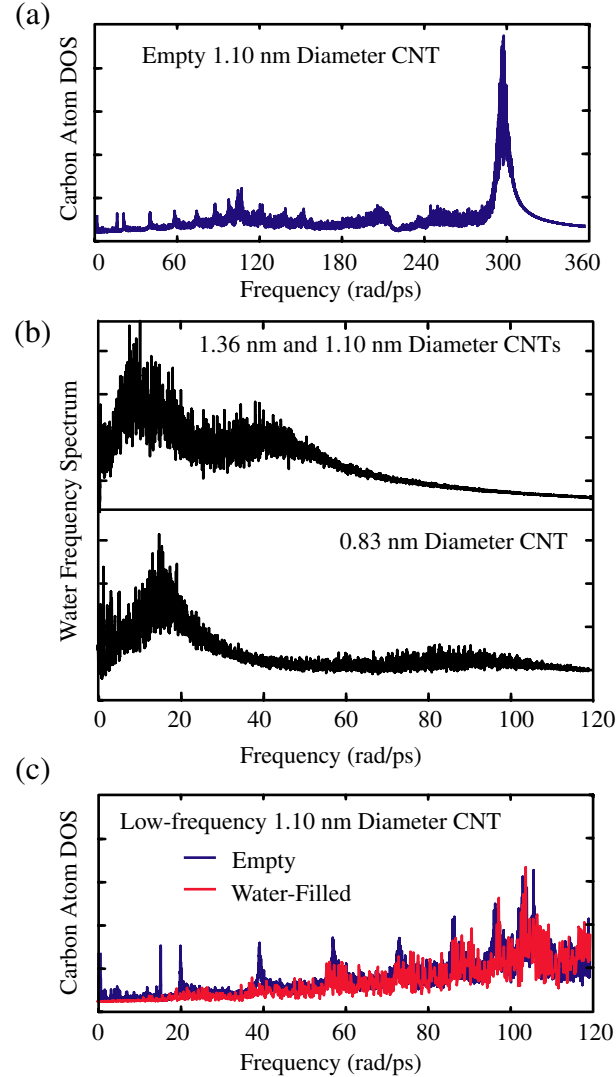


Figure 6.5: (a) Density of states (DOS) for the 1.10 nm-diameter empty CNT. The DOS for 0.83 nm- and 1.36 nm-diameter CNTs have similar features. (b) Vibrational spectra of water molecules inside 1.36 nm-, 1.10 nm-, and 0.83 nm-diameter CNTs. The spectra inside the 1.36 nm- and 1.10 nm-diameter CNTs are similar to what we predict for bulk water. (c) Low-frequency DOS for the carbon atoms in the empty and water-filled 1.10 nm-diameter CNT. As the magnitude of the water molecule spectrum decreases with increasing frequency, the DOS for carbon atoms in the empty and water-filled CNTs converge. Copyright 2010 American Physical Society.

actions between the phonons and non-bonded molecules further perturb the carbon atom potential energy landscape. This behavior increases the range of atomic vibrational frequencies accessed by the carbon atoms in specific modes, further increasing the number of phonon-phonon interactions within the crystal. Collision-broadening due to interactions with the water molecules therefore smears phonon modes over a wider range of vibration frequencies, reducing the height of individual peaks in the carbon atom DOS, and reducing the corresponding low-frequency phonon lifetimes.

Based on the above discussion, we believe that low-frequency acoustic phonon scattering due to interactions with water molecules is primarily responsible for the reduced  $k_{z,\infty}$  in water-filled CNTs [see Fig. 6.4(a)]. In support of this argument, we note that the increased range of vibrational frequencies accessible to the water molecules in the 0.83 nm-diameter CNT cause them to influence more phonon modes than do the water molecules in larger diameter CNTs. Since the thermal energy transported by these higher-frequency modes is smaller than that transported by the low-frequency acoustic phonons, however, the additional reduction in thermal conductivity is small. This behavior also suggests that, given the weak dependence of  $k_{z,\infty}$  on diameter for the water-filled CNTs, the thermal conductivity of graphene in bulk-like water will be similar to  $k_{z,\infty}$  for the water-filled 1.36 nm-diameter CNT [as indicated in Fig. 6.4(b)]. Additionally, since interactions between CNTs and water molecules outside the CNT are unaffected by changes in the CNT surface curvature [62], we believe that  $k_{z,\infty}$  for CNTs surrounded by liquid water (i.e., water only outside the CNT) will be similar to that predicted here for the water-filled 1.36 nm- and 1.10 nm-diameter CNTs.

## 6.5 Summary

We used MD simulation to examine the transition to fully-diffusive phonon transport in empty and water-filled CNTs and in graphene. For empty CNTs, as shown in Fig. 6.3, we find that the magnitude of the fully-diffusive thermal conductivity and the length required to obtain fully-diffusive transport both decrease with increasing CNT diameter. We attribute this behavior to the higher number of acoustic phonon mode scattering events due to the larger number of optical phonon modes accessible to larger-diameter CNTs. As presented in Fig. 6.4, we find that the fully-diffusive thermal conductivity of water-filled CNTs is 20% to 35% lower than that of empty CNTs and only weakly dependent on CNT diameter. By examining the carbon atom DOS and water molecule vibrational spectra presented in Fig. 6.5, we showed that water molecules only scatter phonons with comparable vibrational frequencies. This finding indicates that low-frequency phonon scattering due to interactions with water molecules is primarily responsible for the reduction in the CNT thermal conductivity. Better intermolecular potential functions are needed, however, to make a more quantitative comparison between simulation predictions and future experimental measurements.

Although focused on water/CNT systems, the results presented here can be extended to other solid/liquid composite systems. Most importantly, reductions in the thermal conductivity of a solid in a fluid will be related to the overlap between its phonon frequencies and the vibrational frequencies of the adjacent non-bonded molecules. This relationship is an important feature of composite systems and indicates that not all phonons are influenced equally by interactions with non-bonded molecules [159]. In a real system, compared to the classical MD system modeled here,

consideration must also be given to the phonon quantum occupation number. For water-filled CNTs, the phonon modes that overlap with the water molecule vibrational frequencies are highly populated at room temperature, so that we believe our results are representative of an actual water/CNT composite. In other composite systems, the relationship between temperature, phonon mode population, and liquid vibrational spectrum may need to be considered explicitly. Finally, it is important to note that the influence of solid/liquid interactions on the solid thermal conductivity is also related to the ratio of the solid surface area to solid volume. When this ratio is large (as in a single-walled CNT), the influence of non-bonded molecules on phonon transport is appreciable. Conversely, when this ratio is small, surface effects will be negligible and phonon transport through the solid will be minimally affected by interactions with non-bonded atoms.

## CHAPTER VII

# Predicting phonon properties from the spectral energy density

### 7.1 Introduction

As discussed in Chapter VI, predicting and describing the behavior of semiconductors and dielectric materials requires knowledge of their phonon dispersion relations and lifetimes. At low temperatures, the phonon properties of a crystal in vacuum can be evaluated using harmonic and third-order anharmonic lattice dynamics calculations [195, 196]. In CNTs, silicon nanowires, and other nanoscale materials in realistic environments, however, the phonons will scatter via interactions with non-bonded molecules at surfaces [66, 194]. Since these interactions are non-periodic in time and space, their effects on the phonon properties cannot be directly incorporated into a lattice dynamics calculation. Challenges in predicting the phonon properties also arise with increasing temperature, as the magnitude of the atomic displacements grow and the influence of higher-order phonon scattering events becomes increasingly important [56]. Since third-order anharmonic lattice dynamics calculations only account for three-phonon scattering events, the phonon lifetimes they predict at elevated temperatures will be overestimated [196].

In this chapter, we present a fast, accurate, and straightforward technique for

predicting phonon dispersion relations and lifetimes directly from the velocities of the atoms in a crystal using the phonon spectral energy density. This technique, which extends formulations developed by others [161,162,197,198], naturally includes the full temperature-dependent anharmonicity of the atomic interactions and can be applied to both bulk crystals and crystals interacting with non-bonded molecules. We apply this technique to classical MD simulations of empty and water-filled CNTs, and use the predicted phonon properties to calculate the mode-by-mode contributions to the total thermal conductivity. Next, we compare the fully-anharmonic phonon properties to those obtained from third-order anharmonic lattice dynamics calculations. Our findings indicate that, even at room temperature, neglecting higher-order scattering events in a CNT leads to an overestimation of the acoustic phonon mode lifetimes and the CNT length required to obtain fully-diffusive phonon transport. We then use the spectral energy density to identify how interactions with confined water molecules shift the phonon frequencies, lower the phonon lifetimes, and reduce the CNT thermal conductivity.

The CNT thermal conductivities predicted using the fully-anharmonic phonon properties are in excellent agreement with what we predict using a direct application of the Fourier law in Chapter VI. The number of atoms and simulation runtime required to predict the spectral energy density, however, are both at least one order-of-magnitude smaller than required by MD-based techniques that predict only the thermal conductivity. Thus, although applied here to classical MD simulation, the techniques outlined in this work can be used to predict fully-anharmonic phonon properties using atomic velocities obtained from ab initio MD simulations driven by density functional theory (DFT) calculations.

## 7.2 Calculating the spectral energy density

The spectral energy density is derived by projecting the positions of the atoms in a crystal onto the normal modes of vibration,  $q(\kappa_\nu, t)$ , where  $\kappa$  is the wave vector,  $\nu$  denotes the polarization branch, and  $t$  is time. As discussed in Appendix C, the components of each normal mode are then given by:  $q(\kappa_\nu \alpha, t)$ , such that [193]:

$$q(\kappa_\nu \alpha, t) = e(\kappa_\nu \alpha) \sqrt{\frac{m_b}{N_T}} \times \left\{ \sum_{n_{x,y,z}}^{N_T} u_\alpha(n_{x,y,z}, t) \exp[i\kappa \cdot \mathbf{r}(n_{x,y,z})] \right\}, \quad (7.1)$$

where  $e$  is the corresponding component of the polarization vector and  $u_\alpha(n_{x,y,z}, t)$  is the displacement in the  $\alpha$ -direction of atom  $b$  (with mass  $m_b$ ) inside unit cell  $n_{x,y,z}$  at time  $t$ . The equilibrium position of each unit cell is  $\mathbf{r}(n_{x,y,z})$  and  $N_T (= N_x N_y N_z)$  is the total number of unit cells. The average kinetic energy of each normal mode is:

$$\bar{T}(\kappa_\nu) = \sum_\alpha \sum_b^B \bar{T}(\kappa_\nu \alpha) = \sum_\alpha \sum_b^B \left[ \frac{1}{\tau_0} \int_0^{\tau_0} \frac{1}{2} \dot{q}^*(\kappa_\nu \alpha, t) \dot{q}(\kappa_\nu \alpha, t) dt \right], \quad (7.2)$$

where  $\dot{q}^*$  is the complex conjugate of  $\dot{q}$ . The kinetic energy can be transformed from the time domain to the frequency domain by Parseval's theorem [199] to give:

$$\sum_\alpha \sum_b^B \bar{T}(\kappa_\nu \alpha; \omega) = \sum_\alpha \sum_b^B \lim_{\tau_0 \rightarrow \infty} \frac{1}{4\tau_0} \left| \frac{1}{\sqrt{2\pi}} \int_0^{\tau_0} \dot{q}(\kappa_\nu \alpha; t) \exp(-i\omega t) dt \right|^2, \quad (7.3)$$

where  $\omega$  is an angular frequency. Substituting the time-derivative of Eq. (7.1) into Eq. (7.3) and averaging over  $N_T$  gives the spectral energy density:

$$\begin{aligned} \Phi(\kappa, \omega) &= \\ &\frac{1}{4\pi\tau_0 N_T} \sum_\alpha \sum_b^B m_b \times \\ &\left| \int_0^{\tau_0} \sum_{n_{x,y,z}}^{N_T} \dot{u}_\alpha(n_{x,y,z}; t) \exp[i\kappa \cdot \mathbf{r}(n_{x,y,z}) - i\omega t] dt \right|^2. \end{aligned} \quad (7.4)$$

The polarization vectors do not appear in Eq. (7.4) because they are orthonormal [193]. The spectral energy density is the average kinetic energy per unit cell

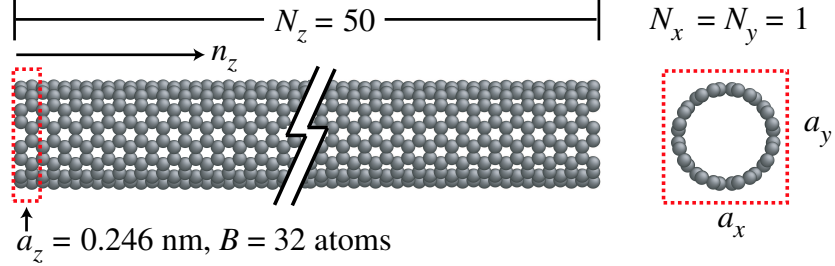


Figure 7.1: Carbon nanotube fragment used when evaluating the phonon spectral energy density. The dashed lines identify the 32 atom unit cell used in Eq. (7.4). The chirality vector for the CNT is (8,8) and the zero-temperature nearest-neighbor atomic spacing is 1.42 Å.

as a function of wave vector and frequency. Although similar expressions for calculating the phonon linewidth have appeared in other reports [197, 198], Eq. (7.4) and its derivation are self-consistently motivated by lattice dynamics and provide more physically meaningful results. For the one-dimensional CNT systems considered here, as shown in Fig. 7.1, the Brillouin zone is one-dimensional. The non-degenerate wavevectors are thus limited to  $\kappa_z = \frac{2\pi n_z}{a_z N_z}$ , where  $a_z$  is the lattice constant,  $N_z$  is the total number of unit cells in the  $z$  direction, and  $n_z$  is an integer ranging from  $-N_z + 1$  to  $N_z$ .

In Fig. 7.2(a) we present the spectral energy density for an empty 1.10 nm-diameter CNT. The resolution of the frequency axis is 0.001 THz and the resolution of the wave number axis is  $0.02 \kappa_z / (2\pi/a_z)$ . The atomic velocities were obtained from *NVE* (constant mass, volume, and energy) MD simulation at a temperature of 298 K [66]. Interactions between carbon atoms are modeled using the REBO potential [87] and periodic boundary conditions are imposed in the axial direction. The shading on the plot indicates the magnitude of the spectral energy density for each  $(\kappa_z, \omega)$  combination corresponding to a total integration time of 1 ns. We find that integrating beyond 1 ns, which is approximately ten times greater than the longest phonon lifetime (see below), does not change the predicted phonon properties.

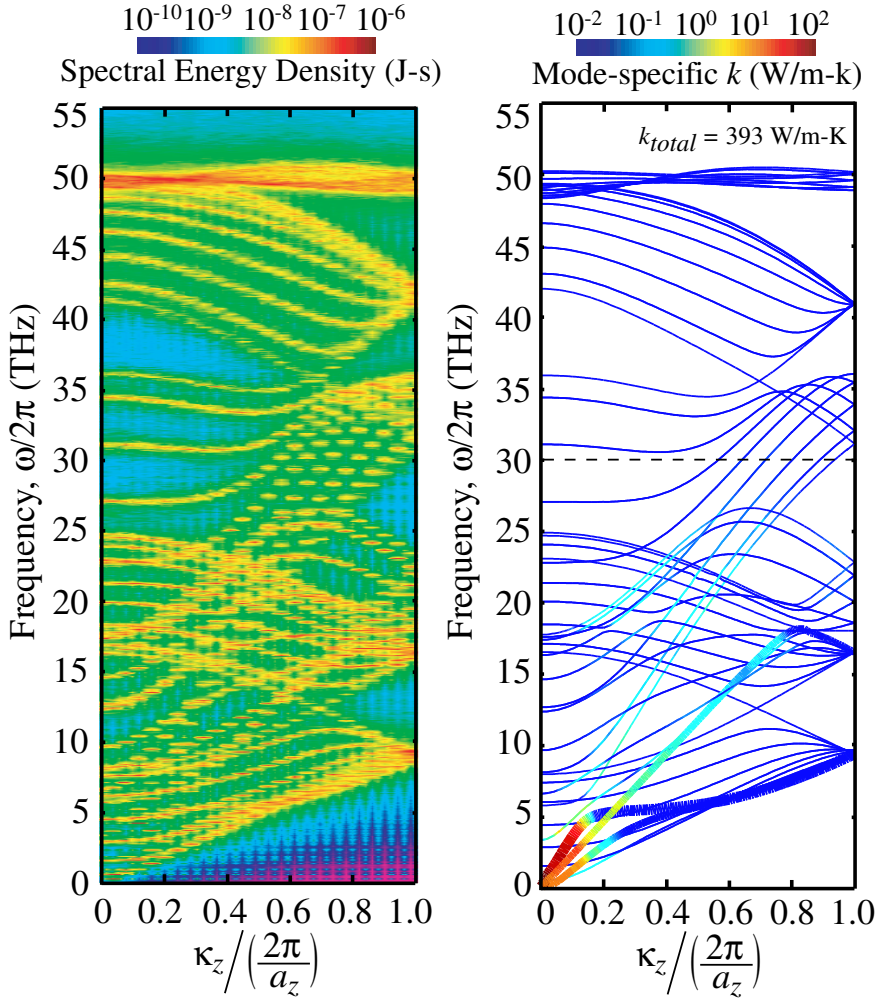


Figure 7.2: (a) Spectral energy density for the 1.10 nm diameter CNT at  $T=298$  K. The color shading indicates the magnitude of the spectral energy density for each combination of  $\kappa_z$  and  $\omega$  corresponding to an integration time of 1 ns. (b) Phonon dispersion relationships and mode-by-mode contributions to the empty CNT total thermal conductivity. The acoustic branches are presented as thick lines for clarity. The dashed line at 30 THz separates high-frequency optical modes from the low-frequency optical modes (see text).

In Fig. 7.4(a) we present the spectral energy density along  $\kappa_z=0$  for frequencies below 5 THz. Similar peak-and-valley profiles exist along the entire frequency axis at each wave vector. The location of the peaks in the spectral energy density are in excellent agreement with the phonon frequencies we obtain from harmonic lattice dynamics calculations, indicating that phonon frequency shifts due to anharmonic effects are negligible. For each phonon mode, the range of frequencies accessed by the carbon atoms is related to the anharmonicity of the interatomic potential and the

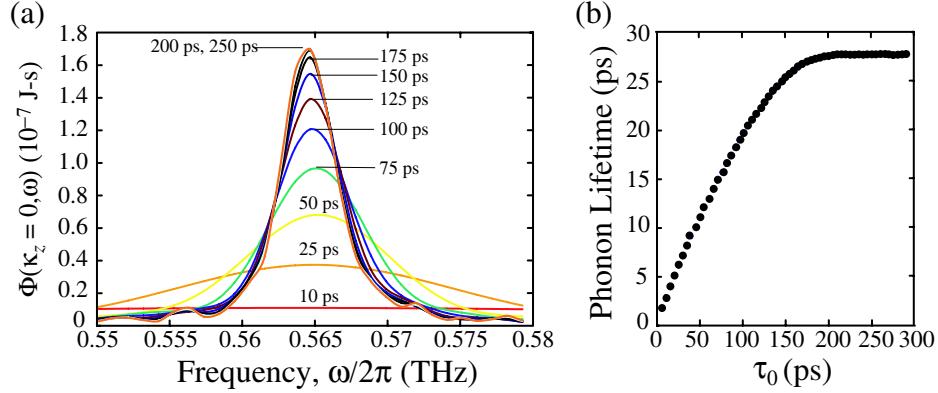


Figure 7.3: (a) Evolution of the spectral energy density for the empty CNT at  $\kappa = 0$  and  $\omega = 0.564$  THz with increasing integration time. (b) Evolution of the phonon lifetime at  $\kappa = 0$  and  $\omega = 0.564$  THz with increasing integration time.

corresponding rate of multi-phonon scattering processes. The shape of this frequency spread for each mode is the Lorentzian function

$$\Phi(\kappa_z, \omega) = \frac{I}{1 + [(\omega - \omega_c)/\gamma]^2}, \quad (7.5)$$

where  $I$  is the peak magnitude,  $\omega_c$  is the frequency at the peak center, and  $\gamma$  is the half-width at half-maximum. As discussed in Appendix C, Eq. (7.5) can be derived by substituting the time-dependant anharmonic normal-mode coordinates [196] into Eq. (7.2). The phonon lifetime is then defined by  $\tau = 1/2\gamma$  [196]. We superimpose fits of Eq. (7.5) onto the spectral energy density shown in Fig. 7.4(a) and estimate the uncertainty of each fit to be 10% of the phonon lifetime.

In Fig. 7.3(a) and 7.3(b), we present the time-evolution of the spectral energy density at  $\kappa = 0$  and  $\omega = 0.564$  THz for the empty CNT. After a 50 ps velocity tracking period, the location of the maximum along the frequency axis [Fig. 7.3(a)] becomes invariant with time. Each peak in the spectral energy density exhibits similar convergence behavior, suggesting that a relatively quick ( $< 0.1$  ns) scan of the Brillouin zone can be used to predict the fully-anharmonic phonon frequencies and dispersion relations. Obtaining a fully-converged phonon lifetime, as illustrated in

Fig. 7.3(b), requires a longer velocity tracking period. In general, we find that a tracking period five times longer than fully-converged phonon lifetime is required to obtain fully-converged phonon properties. For the low-frequency acoustic modes, we find that the necessary tracking period increases to 10 times longer than the phonon lifetime.

In Fig. 7.2(b), we present the phonon dispersion curves, which are formed by connecting the peaks in the spectral energy density with continuous and differentiable curves along  $\kappa_z$ . For many-atom unit cells, like the 32-atom CNT unit cell used here, guidance from lattice dynamics calculations is needed to determine how the peaks in the spectral energy density should be joined and to identify degenerate branches. For materials with smaller unit cells, such as the four-atom rectangular graphene unit cell, we find that the dispersion branches can be identified directly from the spectral energy density. The axial group velocity is obtained from  $v_{g,z} = \partial\omega/\partial\kappa_z$ , which we evaluate numerically using a central difference technique.

### 7.3 Validating the spectral energy density

The relationship between phonon properties and the axial CNT thermal conductivity,  $k_z$ , comes by combining the Boltzmann transport equation under the relaxation time approximation with the Fourier law to give

$$k_z = \sum_{\kappa} \sum_{\nu} c_{ph} v_{g,z}^2 \tau, \quad (7.6)$$

where  $c_{ph}$  is the phonon specific heat [196]. The phonon specific heat for the classical system considered here is  $\frac{k_B}{V}$ , where  $k_B$  is the Boltzmann constant and  $V$  is the system volume. Using phonon properties obtained from the spectral energy density, we predict a total CNT thermal conductivity of 393 W/m-K. As illustrated in Fig. 7.2(b), we find that the four acoustic branches are responsible for 173 W/m-K (44%) of the

thermal conductivity, with the majority of this contribution coming from acoustic modes with reduced wave vectors less than  $0.2 \kappa_z/(2\pi/a_z)$ . The mid-frequency optical branches, defined here as the 55 optical branches with  $\Gamma$ -point ( $\kappa_z=0$ ) frequencies less than 30 THz, are responsible for 196 W/m-K (50%). The remaining higher-frequency optical branches provide the remaining 24 W/m-K (6%). The non-uniform distribution of the thermal conductivity contributions is primarily related to the disparate phonon mean-free paths ( $= v_{g,z}\tau$ ), which extend up to 780 nm for the acoustic modes, to 395 nm for the mid-frequency optical modes, but only to 9 nm for the higher-frequency optical modes. We find that doubling the number of unit cells in the CNT fragment (i.e., doubling its length) does not change the predicted phonon lifetimes or the thermal conductivity.

In Chapter VI, we used a direct application of the Fourier law to explore the variation in thermal conductivity with length for an equivalent 1.10 nm-diameter CNT also modeled using the REBO potential. We found that the thermal conductivity reached a fully-diffusive (i.e., length-independent) value of 409 W/m-K when the CNT length exceeded 700 nm. This thermal conductivity is in excellent agreement with the value of 393 W/m-K calculated here using phonon properties obtained from the spectral energy density. The 700 nm sample length required to obtain fully-diffusive transport in the direct-method calculations, needed to eliminate changes in the phonon lifetimes related to boundary scattering, is longer than 98% of the phonon mean-free paths predicted from the spectral energy density. The additional contributions to thermal transport from phonons with longer mean-free paths, present in the direct-method MD simulations, are comparable to the uncertainty in our reported thermal conductivity prediction [66].

For modes with frequencies greater than 2 THz, the fully-anharmonic lifetimes we

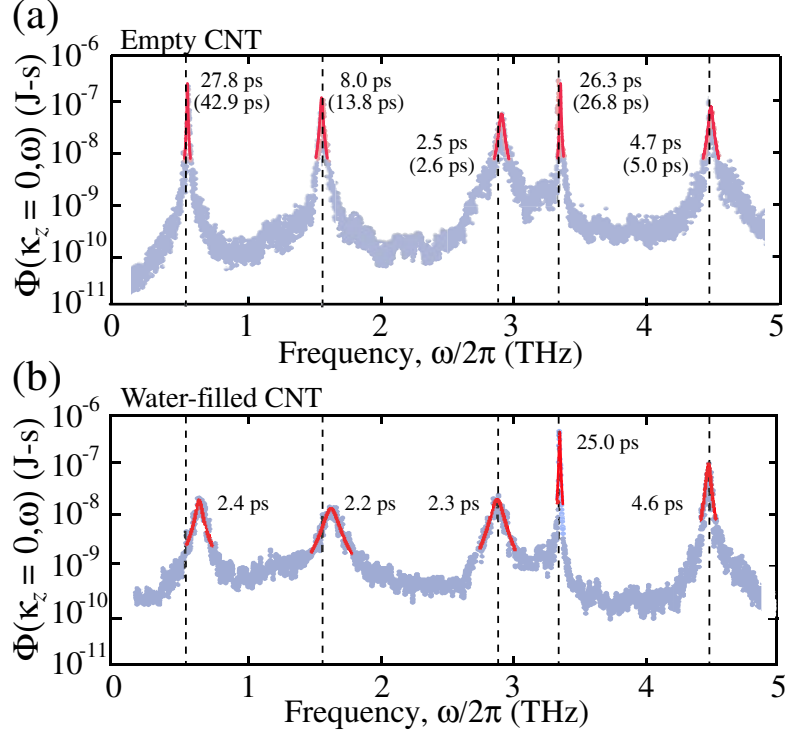


Figure 7.4: (a) Semi-log plot of the empty CNT spectral energy density along  $\kappa_z=0$  for frequencies below 5 THz at  $T=298$  K. The lifetime of each mode is determined by fitting each peak to Eq. (7.5). Sample fits, shown as solid red lines, and the corresponding phonon lifetimes are presented for each peak. The normal mode frequencies calculated from harmonic lattice dynamics calculations are shown as vertical dashed lines and the phonon lifetimes obtained from third-order anharmonic lattice dynamics calculations are given in parentheses. (b) Water-filled CNT spectral energy density along  $\kappa_z=0$ . Interactions with water molecules decrease the phonon lifetime and introduce a small frequency shift for modes with frequencies less than 2 THz.

calculate using the spectral energy density are within 10% of the lifetimes we calculate using third-order anharmonic lattice dynamics calculations [both at a temperature of 298 K, see Fig. 7.4]. We find that increasing the length of the CNT fragment beyond 50 unit cells (the MD system size) does not change the magnitude of the third-order anharmonic lifetimes for frequencies greater than 2 THz. For frequencies less than 2 THz, however, the lifetimes we calculate from third-order anharmonic lattice dynamics calculations exceed the fully-anharmonic lifetimes predicted from MD by up to two orders-of-magnitude. Furthermore, even for CNT fragments 2000 unit-cells long, some of the low-frequency third-order anharmonic lifetimes are not yet

fully converged. Using lifetimes extrapolated from the third-order anharmonic lattice dynamics calculations in place of the fully anharmonic MD values, we find that the maximum phonon mean-free path increases from 780 nm to over 10  $\mu$ m, and that the CNT thermal conductivity increases by a factor of two. Similarly long mean-free paths were reported by Mingo and Broido [168], who used third-order anharmonic lattice dynamics calculations to explore the transition to fully-diffusive phonon transport with increasing length in smaller-diameter CNTs. A comparison of these two third-order anharmonic lattice dynamics results to the fully-anharmonic phonon properties predicted from the spectral energy density, however, suggests that neglecting higher-order phonon scattering leads to a overestimation of the CNT thermal conductivity and the length required to observe fully diffusive phonon transport.

#### 7.4 Phonon transport in water-filled CNTs

The spectral energy density can also be used to study phonon transport in systems that cannot be investigated using lattice dynamics calculations. For example, in Fig. 7.4(b) we present the spectral energy density along  $\kappa_z=0$  for frequencies less than 5 THz obtained from MD simulation of a water-filled 1.10 nm-diameter CNT. Simulations are performed in the *NVE* ensemble using the classical potential functions and simulation procedures discussed in previous chapters. Comparing the water-filled CNT spectral energy density to the empty CNT spectral energy density [Fig. 7.4(a)] clearly shows the effects of collision linewidth broadening, whereby interactions with the water molecules smear the sub-10 THz phonon modes over a wider range of frequencies, reducing the phonon lifetimes by a factor of five to ten. For phonon modes with frequencies less than 2 THz, the water molecules also introduce a small frequency shift of 0.05 to 0.1 THz. We find that for frequencies greater than 10 THz

(the maximum frequency accessed by water molecules inside the CNT), the spectral energy density and the phonon lifetimes are unaffected by interactions with the water molecules [66].

Using the group velocity and lifetime data obtained from the complete water-filled CNT spectral energy density, we predict a total thermal conductivity of 311 W/m-K. This value is in excellent agreement with the thermal conductivity of 295 W/m-K we predicted using a direct application of the Fourier law in an MD simulation [66]. The 82 W/m-K reduction in thermal conductivity is a result of a 75 W/m-K decrease in the acoustic phonon contribution and a 7 W/m-K decrease in optical phonon contribution. Since the spectral energy density naturally captures the effects of non-bonded atoms on phonon transport, mimicking such interactions by damping the atomic velocities is not necessary [159].

In addition to providing a more complete description of phonon transport, the computational effort required to predict the thermal conductivity using the spectral energy density is orders-of-magnitude smaller than that required in other MD-based techniques. For example, using the direct method to predict the thermal conductivity of a 1.10 nm-diameter CNT requires a simulation system cell containing over 100,000 atoms and an equilibration/data collection time of 20 ns [66]. Using the spectral energy density technique, we find that an integration time of 1 ns and a system size of 1,600 atoms are required to obtain fully converged and system size-independent phonon properties. Although equilibrium linear-response techniques (e.g., Green-Kubo) can be used to predict the thermal conductivity using similarly small systems, such calculations require much longer simulation times ( $\sim$ 80 ns) and give no insight into the phonon lifetimes [159].

## 7.5 Discussion and conclusions

The computational effort required to calculate the spectral energy density can be reduced by intelligent sampling of the Brillouin zone. For example, as presented in Fig. 7.3(a), we find that the positions of the peaks in the spectral energy density can be identified after 0.1 ns of integration time; the remaining calculation time is required to obtain fully-converged phonon lifetimes. Thus, performing a short sweep over all values of  $\kappa_z$  and  $\omega$  to identify the peak locations, then performing a focused scan around each peak to determine the phonon linewidths, would significantly reduce the computational time compared to our reported procedure. We also note that, since the calculation time for Eq. (7.4) is proportional to  $N_x N_y N_z$ , calculating the spectral energy density “on-the-fly” may not be practical for simulation of two- or three-dimensional materials. Instead, a more efficient technique would be to print the velocity of each atom at each timestep ( $\approx 10$  GB of required memory depending on the system size), then calculate the spectral energy density as a post-processing procedure that can be trivially parallelized.

We have presented a procedure for extracting phonon dispersion relations and lifetimes directly from atomic velocities. Our predicted CNT thermal conductivities, calculating using the phonon properties predicted from the spectral energy density, agree with those obtained using a direct application of the Fourier law in an equivalent MD simulation. The computational demand associated with calculating the spectral energy density, however, is orders-of-magnitude smaller. Although we modeled the interactions between atoms using empirical potential functions, the formulation presented here can be directly incorporated into ab initio quantum MD simulations (e.g., Car–Parrinello).

## CHAPTER VIII

### Contributions and future research directions

#### 8.1 Summary of findings and contributions

As discussed in Chapter I, the objectives of this work were to (i) understand water flow and heat transfer through CNTs at a transport carrier level, and (ii) develop a set of transport formulations to assist in the design and optimization of CNT-based engineering devices. Chapter II contained an introduction to computer simulation, discussion of potential functions, and overview of MD simulation [61]. Next, in Chapter III, the density and structure of water molecules inside CNTs were examined using MD simulation [62]. In Chapters IV and V, water flow through CNTs and the transition from continuum-level transport to subcontinuum transport with decreasing CNT diameter was investigated [63–65]. Finally, in Chapters VI and VII, phonon transport through empty and water-filled CNTs and the effects of non-periodic interactions on phonon transport [66, 67] were studied. In this chapter, a summary of the major contributions to the research community are presented and three related future research areas are discussed.

- *Poiseuille flow through carbon nanotubes*

We performed a comprehensive investigation into pressure-driven water flow through pristine CNTs with diameters ranging from 1.66 nm to 4.98 nm using MD simula-

tion. We quantified the relationship between pressure gradient and flow rate for each CNT, developed techniques for calculating the variation in water viscosity and slip length with diameter, and derived a model for predicting the flow enhancement of CNTs prior to experimental measurement. The results showed that, by accounting for diameter-related changes in viscosity and slip length, water flow through each CNT could be fully explained in the context of continuum fluid mechanics. Although these findings challenged the validity of some earlier experimental/theoretical investigations, they have been validated by more recent reports [137] and have become an important benchmark for other investigations of water flow through CNTs [200].

- *Subcontinuum flow through carbon nanotubes*

The next step in our investigation of water flow through CNTs was to identify the transition to subcontinuum transport with decreasing CNT diameter. In Chapter V, we performed a systematic investigation into pressure-driven water transport through CNTs with diameters between 0.83 nm and 1.66 nm. We developed tools for characterizing and quantifying the structure of water inside CNT, and developed a procedure for correlating the intra-molecular structure to molecular transport through the tube. We identified the relationship between liquid structure and hydraulic conductivity, and showed how the diameter-related changes in liquid structure govern the flow enhancement of each CNT. We also identified how the long-range structure of water inside CNTs extended the effects of the entrance and exit, leading to diffusion-like transport through CNTs shorter than about 10 nm. These findings have direct application to the development of chemical separation and desalination technologies.

- *Thermal transport through carbon nanotubes*

The high thermal conductivities of CNTs have generated interest in CNT-based thermal transport and management composites [38]. Results from earlier investigations indicated that the low interaction energy between solid-phase carbon atoms and non-bonded fluid molecules [57, 85] gives rise to a large interfacial thermal boundary resistance. Despite these previous investigations into transport across CNT/liquid boundaries, however, fundamental questions concerning the variation in thermal conductivity with CNT length and the effects of non-periodic boundary interactions on phonon transport through CNTs remained unanswered. To address these questions, in Chapter VI we examined thermal transport through empty and water-filled single-walled CNTs with diameters between 0.83 nm and 1.36 nm. Our systems had lengths ranging from 200 nm to 1400 nm, which are much longer than the 100 nm-long systems typically studied by others. We performed an investigation into the transition to fully-diffusive phonon transport with increasing length. We then showed how interactions with water molecules lower the lifetime of the low-frequency phonon modes, leading to a reduction in their contribution to the total CNT thermal conductivity. These findings are an important benchmark for future investigations into thermal transport through graphitic materials. The new insights into the interactions between phonons and fluid molecule also represent a major step towards understanding thermal transport through crystals embedded within non-periodic matrix materials.

- *Predicting phonon properties from the spectral energy density*

We derived a procedure for predicting phonon dispersion relations, lifetimes, and thermal conductivities directly from the velocities of the atoms in a crystal using the spectral energy density. Unlike existing lattice dynamics techniques, this procedure naturally incorporates the full anharmonicity of the atomic interactions into the

phonon property prediction and can be applied to both bulk-like and non-periodic systems. We used this procedure to identify how interactions with confined water molecules shift the phonon frequencies, lower the phonon lifetimes, and reduce the CNT thermal conductivity. Like the direct-method calculations presented in Chapter VI, these findings have an application to the design of nanoscale thermal management materials. However, the techniques outlined in Chapter VII can be used to predict fully-anharmonic phonon properties using atomic velocities obtained from ab initio MD simulations. This ability to simultaneously predict phonon transport properties (using the spectral energy density) and electron transport properties (from the electronic structure) will have a transformative influence on the design of thermal/electrical transport materials.

## 8.2 Future research directions

### 8.2.1 Future-generation gas sequestration and chemical filtration systems

Two issues outlined in the 2009 United Nations Millennium Development Goals Progress Report illustrate the need for advanced fluid filtration and chemical sequestration systems: (i) the rate of global CO<sub>2</sub> emissions has increased by 30 percent over the past fifteen years and (ii) over one billion people do not have sustainable access to clean drinking water [201]. Reports of new techniques for growing nanoporous sieves have generated significant excitement in the filtering communities as possible solutions to both of these global challenges [15]. These sieves, which are usually formed from carbon nanotube (CNT) or zeolite-based materials, have demonstrated higher-than-expected filtrate throughput while exhibiting exceptional chemical selectivities. Provided fabrication technologies can be up-scaled to mass-production levels, these materials have been suggested as lower-cost alternatives to existing CO<sub>2</sub>

scrubbing/sequestering technologies and lower-energy alternatives to existing reverse-osmosis desalination systems.

Despite these rapid advances in fabrication capabilities, many fundamental questions concerning the structure and flow behavior of fluids through nano-sized pores remain unanswered. These challenges are principally related to breakdowns in continuum flow relationships, which occur as the pore diameter approaches the mean-free path of the gas and/or liquid molecules. As discussed in Chapters IV and V, typical boundary conditions (e.g., no-slip) become invalid and material fluid properties (e.g., density and viscosity) become system-size dependent. Consequently, the interactions between the solid and the fluid molecules, along with the effects of surface structure and chemistry on flow, must be considered explicitly to model such systems.

The work presented in Chapters IV and V on water flow through CNTs and the relationship between liquid structure and liquid flow in subcontinuum systems is an important step forward in this area. The next steps to take include developing improved potentials functions for use in MD simulation and identifying the molecular mechanisms of ion and contaminant exclusion/separation from fluids. The role of membrane entrance/exit effects on mass flow rates and the effects of chemical functionalization on system selectivity must also be investigated. Both of these issues must be addressed prior to large-scale device design and fabrication.

### **8.2.2 Biological nanotechnology: Applications to advanced pharmacology**

Recently proposed pharmaceutical treatments have used nano-engineered materials to combat cancer growth and enhance drug delivery. For example, non-invasive techniques have been developed for attaching gold nanoparticles to malignant cancer cells located within living tissue [202]. Exposing the tissue to near-infrared radiation

increases the temperature of the nanoparticles, thereby destroying cancerous tumors without affecting nearby healthy cells. Progress has also been made towards the development of nanodroplet-based aerosols for inhalation therapy and surface-modified nanoparticles for drug delivery [203]. The improved precision associated with such drug-delivery systems, in contrast to conventional inhalers and intravenous therapies, can significantly increase the drug bioavailability (defined as the drug levels that reach the bloodstream) and increase therapeutic index (ratio of desired effect to toxic effect).

Since the performance of these specialty pharmaceuticals are governed by interfacial and boundary interactions, conventional transport relationships used to predict mass and heat flux in bulk-like systems will not accurately predict the performance of these systems [204]. Instead, transport in such nanoscale systems and across the system boundaries must be investigated at the atomic/molecular level. The information presented in Chapter III on liquid density and structure near a solid surfaces is directly related to predicting the dissolution-rate of nanoparticles immersed in biofluids. The next steps in this area are to investigate more realistic solid/liquid boundaries and to explore how dissolution is affected by particle geometry, surface structure, and biofluid flow rate.

### **8.2.3 New materials for energy generation, conversion, and storage**

As discussed in Chapter I, reducing the thickness of photo-voltaic (PV) cells increases their conversion efficiency while lowering the associated manufacturing costs. Uncertainties concerning the crystal structure, electronic band structure, and phonon transport characteristics in sub-micron films, however, have frustrated further advances in PV design and further improvements in device efficiency [14]. Similar

questions concerning transport and carrier scattering have limited efforts to develop nanostructured thermoelectric materials for waste heat recovery systems [205].

These problems can be solved by developing an atomic-level computational framework, based in ab initio quantum chemistry methods, for predicting the transport properties of electrons, photons, and phonons in thin films and nanostructured solid materials. Choosing to build a modeling framework from the “bottom-up,” rather than choosing to modify existing continuum-level theories, will provide a more robust and general modeling tool. Not only can the transport characteristics predicted from the atomic model be generalized to macroscale systems, but changes in carrier transport due to changes in material dimensionality, structure, and chemical composition can be considered explicitly. The atomistic model will also enable engineers to predict not only *which* material configurations give the best transport/energy conversion performance, but also *how* changes in material structure affect transport characteristics. Furthermore, since the tools will be grounded in density functional theory, the accuracy of the predicted transport properties will be comparable to those obtained from experiment.

The work presented in Chapter VII makes important progress towards this goal by developing techniques for predicting fully-anharmonic phonon transport and scattering characteristics directly from first-principles calculations. The next steps are to develop techniques for predicting electron/electron and phonon/electron scattering rates, and to begin validating the predictions through collaboration with experimentalists working in this field.

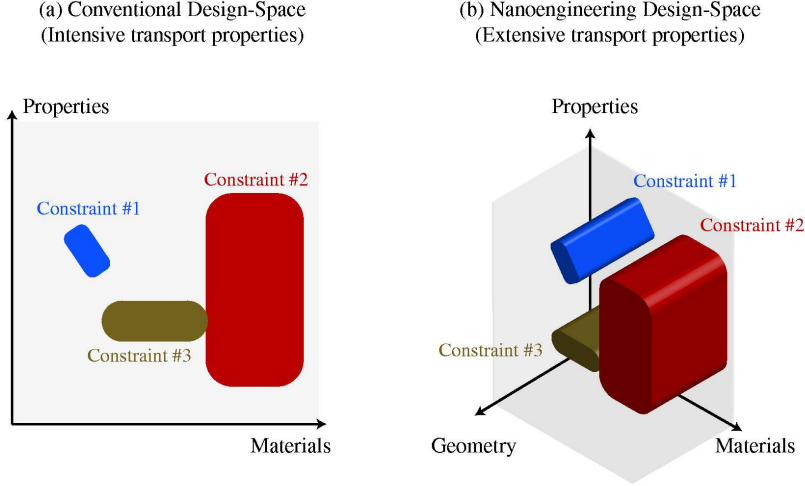


Figure 8.1: Comparison between conventional engineering design-space and nano-engineering design-space. Both design-spaces have design-constraints, which are related to the desired system functionality and cost. Within nanoscale engineering systems, the properties of materials and transport systems become geometry-dependent. This behavior increases both the dimensionality of the design-space and number of candidate materials that will satisfy the design-constraints.

### 8.3 Outlook and perspective

Discoveries related to nanoscale transport phenomena rarely garner the headlines and publicity given to other engineering and robotics disciplines. In a more subtle sense, however, work in this area is changing the way engineering systems are designed, optimized, and miniaturized. For example, during a traditional design-process, as illustrated in Fig 8.1(a), various bulk-like materials and their corresponding transport properties are assembled into a so-called engineering design-space. A number of design-constraints are then mapped onto the design-space to identify a subset of materials that satisfy the device’s performance requirements. Since materials within the design-space rarely (if ever) satisfy all the design-constraints, compromises between performance, cost, and efficiency must be accepted [206].

Now, think of a nano-structured system, where the transition to ballistic carrier transport causes the material-specific thermophysical properties to become size and geometry dependent. As illustrated in Fig 8.1(b), this behavior transforms the

design-space domain and design-space dimensionality, thereby increasing the number of candidate materials that may satisfy the design-constraints. Furthermore, if a material that satisfies the design requirements is not currently available, a nanostructured engineering material with tailored transport characteristics can be built using “bottom-up” fabrication techniques to satisfy a pre-specified set of constraints. As discussed earlier, this procedure is already being used to improve the performance of thermoelectric waste-heat reclamation systems, photovoltaic energy generation systems, and high-capacity batteries. Such practices are also improving the performance of bio-mechanical and pharmacological materials [207,208]. Although many questions and challenges still remain, the topics related to nanoscale transport phenomena will become an increasingly important component of engineering design and practice over the next few decades.



## APPENDIX A

### The REBO potential function

#### A.1 Introduction to the REBO potential

The reactive empirical bond order (REBO) potential is a classical many-body potential function that describes the structure and dynamics of atoms in hydrocarbon molecules, graphite structures, and diamond lattices. The analytic form of the REBO potential was originally derived by Abell from chemical pseudopotential theory [209]:

$$E_b = \frac{1}{2} \sum_i \sum_j [V^R(r_{ij}) - b_{ij} V^A(r_{ij})], \quad (\text{A.1})$$

where  $E_b$  is the chemical binding energy and  $r_{ij}$  is separation distance between bonded atoms  $i$  and  $j$ . The term  $V^R(r_{ij})$  is a repulsive interaction given by a screened Coulomb function:

$$V^R(r_{ij}) = \left(1 + \frac{Q}{r_{ij}}\right) A e^{-\alpha r_{ij}}. \quad (\text{A.2})$$

The term  $V^A(r_{ij})$  is an attractive covalent interaction between bonded atoms. For defect-free carbon nanotubes, where each carbon atom is bonded to three nearest-neighbors, this interaction is given by

$$V^A(r_{ij}) = B_1 e^{-\beta_1 r_{ij}} + B_2 e^{-\beta_2 r_{ij}} + B_3 e^{-\beta_3 r_{ij}}. \quad (\text{A.3})$$

In Eqs. (A.2) and (A.3),  $Q$ ,  $A$ ,  $\alpha$ ,  $B_1$ ,  $B_2$ ,  $B_3$ ,  $\beta_1$ ,  $\beta_2$  and  $\beta_3$  are fitting parameters tuned to reproduce the atomization energy, bond energy, and bond distance of the

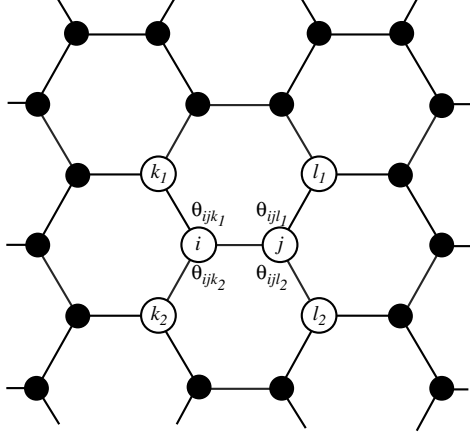


Figure A.1: Atomic indices and angles used in the REBO potential.

carbon atoms. The parameters used to model carbon atoms in a pristine CNT are presented in Table (A.1).

The bond order,  $b_{ij}$ , describes the instantaneous hybridization of the atomic bonding orbitals and is defined by the empirical function:

$$b_{ij} = \frac{1}{2} [b_{ij}^{\sigma-\pi} + b_{ji}^{\sigma-\pi}] + \Pi_{ij}^{RC} + b_{ij}^{DH}, \quad (\text{A.4})$$

where

$$b_{ij}^{\sigma-\pi} = [1 + G(\cos \theta_{ijk_1}) + G(\cos \theta_{ijk_2})]^{-1/2}, \quad (\text{A.5})$$

$$b_{ji}^{\sigma-\pi} = [1 + G(\cos \theta_{jil_1}) + G(\cos \theta_{jil_2})]^{-1/2}, \quad (\text{A.6})$$

In Eq. (A.5), as shown in Fig. A.1,  $\theta_{ijk_1}$  and  $\theta_{ijk_2}$  are the angles formed by atoms  $i$ ,  $j$ , and  $k_1$  (with  $i$  at the vertex), and  $i$ ,  $j$ , and  $k_2$  (also with  $i$  at the vertex). Atoms  $k_1$  and  $k_2$  are the two other atoms (in addition to  $j$ ) bonded to atom  $i$ . In Eq. (A.6),  $\theta_{jil_1}$  and  $\theta_{jil_2}$  are the angles formed by atoms  $j$ ,  $i$ , and  $l_1$  (with  $j$  at the vertex), and  $j$ ,  $i$ , and  $l_2$  (also with  $j$  at the vertex). Atoms  $l_1$  and  $l_2$  are the two other atoms (in addition to  $i$ ) bonded to atom  $j$ .

Table A.1 Fitting parameters used in the REBO potential [87]

$B_1=12388.79197793$ eV	$\beta_1=4.7204523127$ Å $^{-1}$	$Q=0.3134602960833$ Å	$Q_1=0.2386$
$B_2=17.56740646509$ eV	$\beta_2=1.4332132499$ Å $^{-1}$	$A=10953.544162170$ eV	$Q_2=0.4164$
$B_3=30.71493208065$ eV	$\beta_3=1.3826912506$ Å $^{-1}$	$\alpha=4.7465390606595$ Å $^{-1}$	$Q_3=0.2016$

For pristine CNTs, the function  $G(\cos \theta)$  can be written as:

$$G(\cos \theta) = Q_1 \cos^2 \theta + Q_2 \cos \theta + Q_3, \quad (\text{A.7})$$

where  $Q_1$ ,  $Q_2$ , and  $Q_3$  are fitting parameters [presented in Table (A.1)]. This function, which modulates the contribution that each neighbor makes to the bond order based on the instantaneous bond geometry, mimics changes in the carbon-carbon bond hybridizations. The last two terms in Eq. (A.4) account for conjugated bonds and the carbon-carbon double bond dihedral angle. Since conjugate bonds are not present in the pristine CNTs, this term is not needed in our implementation. We also find that contributions to the energy/force stemming from changes in the dihedral angle are negligible. Thus, for computational efficiency, this term is neglected in our simulations.

## A.2 Calculating forces between carbon atoms

The derivative of the potential energy function is required to calculate the force on each atom and integrate the equations of motion. For the REBO potential, this derivative is:

$$-\mathbf{F}_i = \frac{\partial E_b}{\partial r_i} = \sum_j^3 \left[ \frac{\partial V^R(r_{ij})}{\partial r_i} - \frac{\partial b_{ij}}{\partial r_i} V^A(r_{ij}) - b_{ij} \frac{\partial V^A(r_{ij})}{\partial r_i} \right], \quad (\text{A.8})$$

where

$$\frac{\partial V^R(r_{ij})}{\partial r_i} = \left[ \left( 1 + \frac{Q}{r_{ij}} \right) (-\alpha A e^{-\alpha r_{ij}}) + \left( -\frac{Q}{r_{ij}^2} \right) A e^{-\alpha r_{ij}} \right] \left( \frac{r_{ij}}{r_i} \right), \quad (\text{A.9})$$

$$\frac{\partial V^A(r_{ij})}{\partial r_i} = (-\beta_1 B_1 e^{-\beta_1 r_{ij}} - \beta_2 B_2 e^{-\beta_2 r_{ij}} - \beta_3 B_3 e^{-\beta_3 r_{ij}}) \left( \frac{r_{ij}}{r_i} \right), \quad (\text{A.10})$$

and

$$\frac{\partial b_{ij}}{\partial r_i} = \frac{1}{2} \left[ \frac{\partial b_{ij}^{\sigma-\pi}}{\partial r_i} + \frac{\partial b_{ji}^{\sigma-\pi}}{\partial r_i} \right]. \quad (\text{A.11})$$

As mentioned above, the last two terms of Eq. (A.4) are not needed in the energy and force calculations for carbon atoms in pristine CNTs. The derivatives within Eq. (A.11) are:

$$\begin{aligned} \frac{\partial b_{ij}^{\sigma-\pi}}{\partial r_i} &= \frac{1}{2 [1 + G(\cos \theta_{ijk_1}) + G(\cos \theta_{ijk_2})]^{3/2}} \times \\ &\left( \frac{\partial G(\cos \theta_{ijk_1})}{\cos \theta_{ijk_1}} \frac{\partial \cos \theta_{ijk_1}}{\partial r_i} + \frac{\partial G(\cos \theta_{ijk_2})}{\partial \cos \theta_{ijk_2}} \frac{\partial \cos \theta_{ijk_2}}{\partial r_i} \right) \end{aligned} \quad (\text{A.12})$$

where

$$\frac{\partial \cos \theta_{ijk_1}}{\partial r_i} = \cos \theta_{ijk_1} \left[ \frac{\mathbf{r}_{ij}}{(r_{ij})^2} + \frac{\mathbf{r}_{ik_1}}{(r_{ik_1})^2} \right] - \left[ \frac{\mathbf{r}_{ij} + \mathbf{r}_{ik_1}}{(r_{ij})(r_{ik_1})} \right], \quad (\text{A.13})$$

$$\frac{\partial \cos \theta_{ijk_2}}{\partial r_i} = \cos \theta_{ijk_2} \left[ \frac{\mathbf{r}_{ij}}{(r_{ij})^2} + \frac{\mathbf{r}_{ik_2}}{(r_{ik_2})^2} \right] - \left[ \frac{\mathbf{r}_{ij} + \mathbf{r}_{ik_2}}{(r_{ij})(r_{ik_2})} \right], \quad (\text{A.14})$$

and

$$\begin{aligned} \frac{\partial b_{ji}^{\sigma-\pi}}{\partial r_i} &= \frac{1}{2 [1 + G(\cos \theta_{jil_1}) + G(\cos \theta_{jil_2})]^{3/2}} \times \\ &\left( \frac{\partial G(\cos \theta_{jil_1})}{\partial \cos \theta_{jil_1}} \frac{\partial \cos \theta_{jil_1}}{\partial r_i} + \frac{\partial G(\cos \theta_{jil_2})}{\partial \cos \theta_{jil_2}} \frac{\partial \cos \theta_{jil_2}}{\partial r_i} \right), \end{aligned} \quad (\text{A.15})$$

where

$$\frac{\partial \cos \theta_{jil_1}}{\partial r_i} = \cos \theta_{jil_1} \left[ \frac{\mathbf{r}_{ij}}{(r_{ij})^2} \right] - \left[ \frac{\mathbf{r}_{ij}}{(r_{ij})(r_{il_1})} \right], \quad (\text{A.16})$$

$$\frac{\partial \cos \theta_{jil_2}}{\partial r_i} = \cos \theta_{jil_2} \left[ \frac{\mathbf{r}_{ij}}{(r_{ij})^2} \right] - \left[ \frac{\mathbf{r}_{ij}}{(r_{ij})(r_{il_2})} \right]. \quad (\text{A.17})$$

Using these forces, the equations of motion can be integrated using a Verlet algorithm. Note that, since the carbon atoms in pristine CNTs (modeled using MD) remain bonded to the same three nearest-neighbors, the REBO potential can be implemented to scale linearly with the number of carbon atoms.

## APPENDIX B

### Quaternions and molecular rotation

#### B.1 Rigid body motion

Within the context of classical dynamics, the motion of molecules can be described in terms of center-of-mass translation and rigid-body rotation. The translational motion is typically described using the equation of motion presented in Eq. (2.4). When describing rotational motion, however, additional methodologies for calculating the torque on each molecule, the inertia tensor, and the local molecular orientation must also be specified.

Within the non-relativistic regime, the total torque  $\boldsymbol{\tau}$  on molecule  $i$  is given by

$$\boldsymbol{\tau}_i = \sum_a (\mathbf{r}_{ia} - \mathbf{r}_i) \times \mathbf{f}_{ia}, \quad (\text{B.1})$$

where  $a$  is the total number of atoms in the molecule,  $\mathbf{f}_{ia}$  is the total force on atom  $a$  (due to interactions with other molecules), and  $\mathbf{r}_{ia} - \mathbf{r}_i$  describes the position of atom  $a$  relative to the molecule center of mass,  $\mathbf{r}_i$ . The torque on each molecule is directly related to the time-derivative of the angular momentum of the molecule,  $\mathbf{L}_i$ , through

$$\boldsymbol{\tau}_i = \frac{d\mathbf{L}_i}{dt}, \quad (\text{B.2})$$

where  $t$  is time. The angular momentum, which is analogous to linear momentum and describes the rotational state of the molecule, is a three-dimensional vector defined

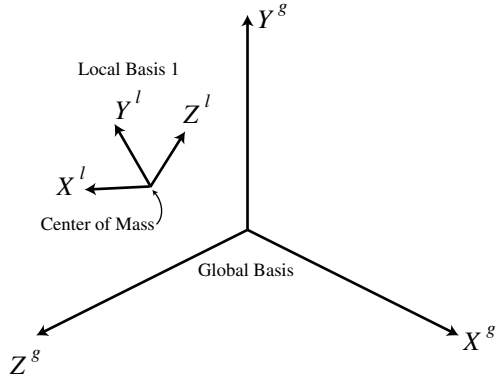


Figure B.1: Local basis set (defined by  $X^l$ ,  $Y^l$ , and  $Z^l$ ) positioned within a global basis set (defined by  $X^g$ ,  $Y^g$ , and  $Z^g$ ). A transformation matrix is required to convert vectors defined in the global basis to the local basis.

by:

$$\mathbf{L} = I\boldsymbol{\omega}, \quad (\text{B.3})$$

where  $I$  is the inertia tensor and  $\boldsymbol{\omega}$  is the angular velocity. The inertia tensor describes the distribution of mass about a local reference frame [210]:

$$I = \begin{pmatrix} I_{xx} & -I_{xy} & -I_{xz} \\ -I_{yx} & I_{yy} & -I_{yz} \\ -I_{zx} & -I_{zy} & I_{zz} \end{pmatrix}. \quad (\text{B.4})$$

Using this definition to expand Eq. (B.3) gives:

$$\begin{pmatrix} L_x \\ L_y \\ L_z \end{pmatrix} = \begin{pmatrix} I_x & -I_{xy} & -I_{xz} \\ -I_{yx} & I_y & -I_{yz} \\ -I_{zx} & -I_{zy} & I_z \end{pmatrix} \begin{pmatrix} \omega_x \\ \omega_y \\ \omega_z \end{pmatrix}, \quad (\text{B.5})$$

where  $\omega_i$  are the components of the angular velocity vector.

## B.2 Describing the orientation of molecules

Calculating  $\tau_i$  requires a knowledge of the orientations and center-of-mass positions of all molecules within the simulation. As illustrated in Fig. B.1, this description

requires two reference frames: (i) a fixed global basis set, which defines the center-of-mass positions, and (ii) a moving local basis set, which defines the molecular orientation. For computational efficiency, the local basis-sets usually corresponds to the principal moments of inertia such that the inertia tensor is diagonal [210].

Any vector defined in the global basis-set,  $\mathbf{e}^g$ , can be expressed in terms of the local basis-set,  $\mathbf{e}^l$ , using a transformation matrix,  $\mathbf{A}$ :

$$\mathbf{e}^l = \mathbf{A}\mathbf{e}^g. \quad (\text{B.6})$$

Within the context of molecular simulation, two methodologies are commonly used to define the transformation matrix: Euler angles [211] and quaternions [68]. When using an Euler angles description, as illustrated in Fig. B.2, the three-dimensional transformation matrix is defined by:

$$\mathbf{A} = \begin{pmatrix} \cos \phi \cos \psi - \sin \phi \cos \theta \sin \psi & \sin \phi \cos \psi + \cos \phi \cos \theta \sin \psi & \sin \theta \sin \psi \\ -\cos \phi \sin \psi - \sin \phi \cos \theta \cos \psi & -\sin \phi \sin \psi + \cos \phi \cos \theta \cos \psi & \sin \theta \cos \psi \\ \sin \phi \sin \theta & -\cos \phi \sin \theta & \cos \theta \end{pmatrix}, \quad (\text{B.7})$$

where  $\phi$  is a rotation about the  $z$  axis,  $\theta$  is a rotation about the new  $x$  axis, and  $\psi$  is a rotation about the new  $z$  axis. The equations of motion of the Euler angles are then:

$$\begin{aligned} \dot{\phi} &= -\omega_x^g \frac{\sin \phi \cos \theta}{\sin \theta} + \omega_y^g \frac{\cos \phi \cos \theta}{\sin \theta} + \omega_z^g \\ \dot{\theta} &= \omega_x^g \cos \phi + \omega_y^g \sin \phi \\ \dot{\psi} &= \omega_x^g \frac{\sin \phi}{\sin \theta} - \omega_y^g \frac{\cos \phi}{\sin \theta}. \end{aligned} \quad (\text{B.8})$$

As discussed in standard linear algebra textbooks [212], Eq. (B.7) can be obtained directly from the successive multiplication of the three Euler angle rotation matrices.

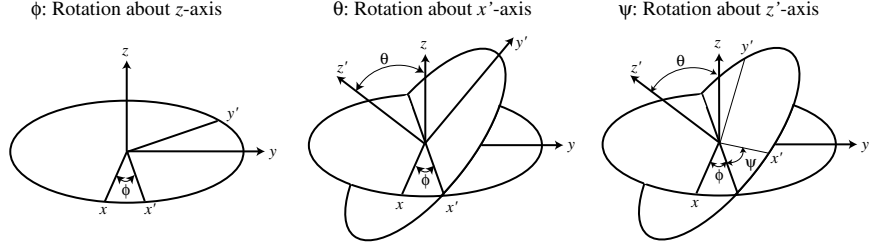


Figure B.2: Definition of the Euler angles. The rotation sequence is noncommutative.

Although the Euler angle approach is conceptually straightforward, the 29 trigonometric functions associated with Eq. (B.7) are too computationally expensive for large-scale simulation and the singularities present in Eq. (B.8) as  $\theta \rightarrow 0$  lead to numerical instabilities.

Quaternions provide an alternative and more computationally efficient definition of  $\mathbf{A}$ . A quaternion is a set of four scalar quantities [213]:

$$\mathbf{Q} = (q_0, q_1, q_2, q_3), \quad (\text{B.9})$$

which are subject to the normalization condition:

$$q_0^2 + q_1^2 + q_2^2 + q_3^2 = 1. \quad (\text{B.10})$$

In the context of Euler angles, the four components of the quaternion are defined by:

$$\begin{aligned} q_0 &= \cos\left(\frac{1}{2}\theta\right) \cos\left[\frac{1}{2}(\phi + \psi)\right] \\ q_1 &= \sin\left(\frac{1}{2}\theta\right) \cos\left[\frac{1}{2}(\phi - \psi)\right] \\ q_2 &= \sin\left(\frac{1}{2}\theta\right) \sin\left[\frac{1}{2}(\phi - \psi)\right] \\ q_3 &= \cos\left(\frac{1}{2}\theta\right) \sin\left[\frac{1}{2}(\phi + \psi)\right], \end{aligned} \quad (\text{B.11})$$

and the transformation matrix becomes:

$$\mathbf{A} = \begin{pmatrix} q_0^2 + q_1^2 - q_2^2 - q_3^2 & 2(q_1q_2 + q_0q_3) & 2(q_1q_3 - q_0q_2) \\ 2(q_1q_2 + q_0q_3) & q_0^2 - q_1^2 + q_2^2 - q_3^2 & 2(q_2q_3 + q_0q_1) \\ 2(q_1q_3 + q_0q_2) & 2(q_2q_3 - q_0q_1) & q_0^2 - q_1^2 - q_2^2 + q_3^2 \end{pmatrix}. \quad (\text{B.12})$$

The quaternion equations of motion are given by the differential equations [68]:

$$\begin{pmatrix} \dot{q}_0 \\ \dot{q}_1 \\ \dot{q}_2 \\ \dot{q}_3 \end{pmatrix} = \begin{pmatrix} q_0 & -q_1 & -q_2 & -q_3 \\ q_1 & q_0 & -q_3 & q_2 \\ q_2 & q_3 & q_0 & -q_1 \\ q_3 & -q_2 & q_1 & q_0 \end{pmatrix} \begin{pmatrix} 0 \\ \omega_x^b \\ \omega_y^b \\ \omega_z^b \end{pmatrix}. \quad (\text{B.13})$$

This quaternion-based equation of motion, which can be advanced through time using Verlet algorithms, contains no singularities.

### B.3 Implementation

The combined effects of translation and rotation can be described in a single MD simulation using the following computational sequence:

1. Calculate the total force and torque on each molecule at time  $t$
2. Define the rotation matrix  $\mathbf{A}_i$  for each molecule using the quaternions at  $t$  and Eq. (B.12)
3. Using the calculated torques and Eq. (B.2), advance  $\mathbf{L}_i^g$ , the angular momentum defined in the global basis from  $t$  to  $t + \delta t$
4. Convert  $\mathbf{L}_i^g$  to  $\omega_i^l$ , the angular velocity defined in the local basis, using Eqs. (B.3) and (B.6)
5. Use  $\omega_i^l$  and Eq. (B.13) to the advance the quaternions from  $t$  to  $t + \delta t$  (B.13)

6. Using the calculated forces, advance the center-of-mass positions and velocities  $t$  to  $t + \delta t$  using a Verlet algorithm
7. Using the new positions and quaternions, calculate the global position of each atom at  $t + \delta t$
8. Return to step 1 and repeat

Other techniques for modeling rigid body translation and rotation, such as the SHAKE [214] and RATTLE algorithms [215], are also available. Although these techniques can conserve energy and momentum using a larger timestep than the quaternion methods used here, their implementation requires a computationally expensive iterative solution or matrix inversion for all molecules at each integration step.

## APPENDIX C

### Spectral energy density

#### C.1 Deriving the spectral energy density

To derive the spectral energy density, we begin with results from standard harmonic lattice dynamics (LD) theory. The system Hamiltonian is [190],

$$H = \frac{1}{2} \sum_{\kappa, \nu}^{N, 3n} [\dot{q}^*(\kappa; t) \dot{q}(\kappa; t) + \omega_0^2(\kappa) q^*(\kappa; t) q(\kappa; t)] = \sum_{\kappa, \nu}^{N, 3n} [T(\kappa; t) + V(\kappa; t)], \quad (\text{C.1})$$

where  $\omega_0(\kappa)$  is the frequency of the phonon denoted by wave vector  $\kappa$  and dispersion branch  $\nu$ , and  $N$  and  $n$  are the total number of unit cells and number of atoms in the unit cell. The Hamiltonian is the total system energy and is equal to the sum of the mode- and time-dependent kinetic and potential energies,  $T(\kappa; t)$  and  $V(\kappa; t)$ . The phonon mode (normal mode) coordinate and its time derivative are given by

$$q(\kappa; t) = \sum_{\alpha, b, l}^{3, n, N} \sqrt{\frac{m_b}{N}} u_\alpha(b; t) e^*(\kappa \cdot \alpha) \exp[i\kappa \cdot \mathbf{r}_0(l)], \quad (\text{C.2})$$

and

$$\dot{q}(\kappa; t) = \sum_{\alpha, b, l}^{3, n, N} \sqrt{\frac{m_b}{N}} \dot{u}_\alpha(b; t) e^*(\kappa \cdot \alpha) \exp[i\kappa \cdot \mathbf{r}_0(l)], \quad (\text{C.3})$$

where  $m_b$  is the mass of the  $b^{\text{th}}$  atom in the unit cell, and  $\mathbf{r}_0(l)$  is the equilibrium position vector of the  $l^{\text{th}}$  unit cell. The  $\alpha$ -component of the displacement (from equilibrium),  $u_\alpha(b; t)$ , and velocity,  $\dot{u}_\alpha(b; t)$ , of the  $b^{\text{th}}$  atom in the  $l^{\text{th}}$  unit cell are

time-dependent and are related to the phonon mode coordinates through the time-independent polarization vector  $e(\kappa_\nu^b)$  [the asterisk superscript in Eqs. (C.2) and (C.3) denotes the complex conjugate].

The allowed wave vectors are defined by the crystal lattice. The phonon frequencies and polarization vectors, however, are not known a priori. It is convenient to define  $\sum_{\alpha,b}^{3,n} q(\kappa_\nu^b; t) = q(\kappa_\nu; t)$  and recast Eqs. (C.1), (C.2), and (C.3) as

$$\begin{aligned} H &= \frac{1}{2} \sum_{\kappa,\nu}^{N,3n} \sum_{\alpha,b}^{3,n} [\dot{q}^*(\kappa_\nu^b; t) \dot{q}(\kappa_\nu^b; t) + \omega_0^2(\kappa_\nu^b) q^*(\kappa_\nu^b; t) q(\kappa_\nu^b; t)] \\ &= \sum_{\kappa,\nu}^{N,3n} \sum_{\alpha,b}^{3,n} [T(\kappa_\nu^b; t) + V(\kappa_\nu^b; t)], \end{aligned} \quad (\text{C.4})$$

$$q(\kappa_\nu^b; t) = e(\kappa_\nu^b) \sqrt{\frac{m_b}{N}} \sum_l^N u_\alpha(l; t) \exp[i\kappa \cdot \mathbf{r}_0(l)], \quad (\text{C.5})$$

and

$$\dot{q}(\kappa_\nu^b; t) = e(\kappa_\nu^b) \sqrt{\frac{m_b}{N}} \sum_l^N \dot{u}_\alpha(l; t) \exp[i\kappa \cdot \mathbf{r}_0(l)]. \quad (\text{C.6})$$

The coordinates  $q(\kappa_\nu^b; t)$  are associated with atom  $b$  and direction  $\alpha$ . In arriving at Eq. (C.4), we make use of the fact that  $e(\kappa_\nu^b) = e^*(-\kappa_\nu^b)$  and  $q(\kappa_\nu; t) = q^*(-\kappa_\nu; t)$  to pull the summations over  $\alpha$  and  $b$  out of the multiplications in Eq. (C.1).

The average kinetic energy of the crystal is

$$\langle T(\kappa_\nu^b; t) \rangle = \frac{1}{2} \lim_{\tau_0 \rightarrow \infty} \frac{1}{2\tau_0} \int_{-\tau_0}^{\tau_0} \dot{q}^*(\kappa_\nu^b; t) \dot{q}(\kappa_\nu^b; t) dt. \quad (\text{C.7})$$

The kinetic energy can be transformed from the time domain ( $t$ ) to the frequency domain ( $\omega$ ) by Parseval's theorem [199], allowing Eq. (C.7) to be written as

$$\langle T(\kappa_\nu^b; \omega) \rangle = \lim_{\tau_0 \rightarrow \infty} \frac{1}{4\tau_0} \left| \frac{1}{\sqrt{2\pi}} \int_{-\tau_0}^{\tau_0} \dot{q}(\kappa_\nu^b; t) \exp(-i\omega t) dt \right|^2. \quad (\text{C.8})$$

Substituting the expression for  $\dot{q}(\kappa_\nu^b; t)$  [Eq. (C.6)] into Eq. (C.8), we obtain

$$\langle T(\kappa_\nu^b; \omega) \rangle = \frac{m_b |e(\kappa_\nu^b)|^2}{8\pi\tau_0 N} \left| \int_{-\tau_0}^{\tau_0} \sum_l^N \dot{u}_\alpha(l; t) \exp[i\kappa \cdot \mathbf{r}_0(l) - i\omega t] dt \right|^2, \quad (\text{C.9})$$

where the limit has been dropped.

The spectral energy density is

$$\begin{aligned}\Phi(\omega, \boldsymbol{\kappa}) &= 2 \sum_{\nu}^{3n} \sum_{\alpha,b}^{3,n} \langle T(\nu^b_{\alpha}; \omega) \rangle \\ &= \frac{1}{4\pi\tau_0 N} \sum_b^n m_b \sum_{\alpha}^3 \left| \int_{-\tau_0}^{\tau_0} \sum_l^N \dot{u}_{\alpha}(l_b; t) \exp[i\boldsymbol{\kappa} \cdot \mathbf{r}_0(l_0) - i\omega t] dt \right|^2, \quad (\text{C.10})\end{aligned}$$

where we have used the fact that the eigenvectors are orthonormal (i.e.,  $\sum_{\nu}^{3n} |e(\nu^b_{\alpha})|^2 = 1$ ) [193] and equipartition of energy (valid for a classical, harmonic system). The Hamiltonian can be written as

$$H = \sum_{\boldsymbol{\kappa}}^N \int_0^{\infty} \Phi(\omega, \boldsymbol{\kappa}) d\omega = 2 \sum_{\boldsymbol{\kappa}, \nu}^{N, 3n} \sum_{\alpha, b}^{3,n} \langle T(\nu^b_{\alpha}; t) \rangle. \quad (\text{C.11})$$

## C.2 Predicting phonon lifetimes using the spectral energy density

In an anharmonic system, the phonon populations fluctuate about the equilibrium distribution function. The phonon mode coordinates and their time derivatives are

$$q_A(\nu; t) = q_{SS}(\nu; t) + q_T(\nu; t) \quad (\text{C.12})$$

and

$$\dot{q}_A(\nu; t) = \dot{q}_{SS}(\nu; t) + \dot{q}_T(\nu; t). \quad (\text{C.13})$$

The steady-state (ss) and transient (t) parts and their time derivatives are given by [190]

$$q_{SS}(\nu; t) = C_1(\nu) \exp\{i\omega_A(\nu) t\} + C_2(\nu) \exp\{-i\omega_A(\nu) t\}, \quad (\text{C.14})$$

$$q_T(\nu; t) = \exp[-\Gamma(\nu) |t|] \{C_3(\nu) \exp[i\omega_A(\nu) t] - C_4(\nu) \exp[-i\omega_A(\nu) t]\}, \quad (\text{C.15})$$

$$\dot{q}_{SS}(\nu; t) = iC_1(\nu) \omega_A(\nu) \exp\{i\omega_A(\nu) t\} - iC_2(\nu) \omega_A(\nu) \exp\{-i\omega_A(\nu) t\}, \quad (\text{C.16})$$

and

$$\begin{aligned} \dot{q}_T(\kappa; t) = & \exp[-\Gamma(\kappa) |t|] \{ iC_3(\kappa) [\omega_A(\kappa) + i\Gamma(\kappa)] \exp[i\omega_A(\kappa) t] \\ & - iC_4(\kappa) [\omega_A(\kappa) - i\Gamma(\kappa)] \exp[-i\omega_A(\kappa) t] \}, \quad (\text{C.17}) \end{aligned}$$

where the  $C$ 's are constants and  $\omega_A(\kappa)$  and  $\Gamma(\kappa)$  are the phonon mode frequency and scattering rate (i.e., linewidth). The transient part describes the creation of an excess in the population of a phonon mode for  $t < 0$  and its decay back to equilibrium for  $t > 0$ .

The framework used for anharmonic lattice dynamics is an excitation and decay of a single phonon mode. In a real system, there will be multiple phonons in each mode that simultaneously grow or decay with time. Thus, dealing only with  $\dot{q}$  we let

$$\begin{aligned} \dot{q}(\kappa; t) = & \sum_j i \exp[-\Gamma(\kappa) |t - t_j|] \{ A_j(\kappa) [\omega_A(\kappa) + i\Gamma(\kappa)] \exp[i\omega_A(\kappa) (t - t_j)] \\ & - B_j(\kappa) [\omega_A(\kappa) - i\Gamma(\kappa)] \exp[-i\omega_A(\kappa) (t - t_j)] \}, \quad (\text{C.18}) \end{aligned}$$

where many phonons in each mode, indexed by  $j$ , are simultaneously being created and destroyed. The phonons grow for  $t < t_j$  and decay for  $t > t_j$  and  $A_j$  and  $B_j$  are constants. We are unconcerned with the values of  $t_j$ ,  $A_j$ , and  $B_j$ , though they should take on values such that  $\langle \dot{q}_{SS}^*(\kappa; t) \dot{q}_{SS}(\kappa; t) \rangle = \langle \dot{q}^*(\kappa; t) \dot{q}(\kappa; t) \rangle$ .

Next, we note that

$$\langle T(\kappa; \omega) \rangle = \sum_{\alpha, b}^{3,n} \langle T(\kappa \alpha^b; \omega) \rangle = \lim_{\tau_0 \rightarrow \infty} \frac{1}{4\tau_0} \left| \frac{1}{\sqrt{2\pi}} \int_{-\tau_0}^{\tau_0} \dot{q}(\kappa; t) \exp(-i\omega t) dt \right|^2, \quad (\text{C.19})$$

which can be shown using  $T(\kappa; t)$  and  $\dot{q}(\kappa; t)$  in place of  $T(\kappa \alpha^b; t)$  and  $\dot{q}(\kappa \alpha^b; t)$  in Eq. (C.7) and using Parseval's theorem [as used to obtain Eq. (C.8)]. By substituting Eq.

(C.18) into Eq. (C.19) and performing the integration overtime we find

$$\langle T(\nu; \omega) \rangle = \frac{1}{16\pi\tau_0} \left| \sum_j \exp[-i\omega t_j] \left\{ A_j(\nu) \frac{\omega_A(\nu) + i\Gamma(\nu)}{\omega_A(\nu) - \omega + i\Gamma(\nu)} + B_j(\nu) \frac{\omega_A(\nu) - i\Gamma(\nu)}{\omega_A(\nu) + \omega - i\Gamma(\nu)} \right\} \right|^2. \quad (\text{C.20})$$

We are primarily interested in values of  $\omega$  where  $\omega \approx \omega_A$ . When  $\omega \approx \omega_A$ , the term involving  $A_j$  becomes large since  $\Gamma \ll \omega_A$  and the term involving  $B_j$  can be neglected. Hence, we find

$$\langle T(\nu; \omega) \rangle = \frac{1}{16\pi\tau_0} \sum_{j,j'} \cos[\omega(t_{j'} - t_j)] A_j(\nu) A_{j'}(\nu) \frac{\omega_A^2(\nu) + \Gamma^2(\nu)}{\Gamma(\nu)} \frac{\Gamma(\nu)}{[\omega_A(\nu) - \omega]^2 + \Gamma^2(\nu)}. \quad (\text{C.21})$$

Using Eqs. (C.10), (C.19), and (C.21), we finally arrive at

$$\Phi(\omega, \kappa) = 2 \sum_{\nu}^{3n} \langle T(\nu; \omega) \rangle = \sum_{\nu}^{3n} C_0(\nu) \frac{\Gamma(\nu)/\pi}{[\omega_A(\nu) - \omega]^2 + \Gamma^2(\nu)}, \quad (\text{C.22})$$

where

$$C_0(\nu) = \sum_j \sum_{j'} \cos[\omega(t_{j'} - t_j)] A_j(\nu) A_{j'}(\nu) \frac{\omega_A^2(\nu) + \Gamma^2(\nu)}{8\tau_0\Gamma(\nu)}. \quad (\text{C.23})$$

Thus,  $\Phi(\omega, \kappa)$  is a superposition of  $3n$  Lorentzian functions with centers at  $\omega_A(\nu)$  with a half width at half maximum of  $\Gamma(\nu)$ . We know from anharmonic LD that [185, 216]

$$\tau(\nu) = \frac{1}{2\Gamma(\nu)}, \quad (\text{C.24})$$

where  $\tau$  is the phonon relaxation time.

## BIBLIOGRAPHY

- [1] F. X. Xiu, Z. Yang, L. J. Mandalapu, D. T. Zhao, J. L. Liu, and W. P. Beyermann, “High-mobility Sb-doped p-type ZnO by molecular-beam epitaxy.” *Applied Physics Letters* **87** (2005) 152101.
- [2] R. K. Debnath, R. Meijers, T. Richter, T. Stoica, R. Calarco, and H. Luth, “Mechanism of molecular beam epitaxy growth of GaN nanowires on Si(111).” *Applied Physics Letters* **90** (2007) 123117.
- [3] W. McCray, “Mbe deserves a place in the history books.” *Nature Nanotechnology* **2** (2007) 2–4.
- [4] P. F. Garcia, R. S. McLean, M. H. Reilly, and G. N. Jr., “Transparent ZnO thin-film transistor fabricated by RF magnetron sputtering.” *Applied Physics Letters* **82** (2003) 1117.
- [5] T. Kubart, D. Depla, D. M. Martin, T. Nyberg, and S. Berg, “High rate reactive magnetron sputter deposition of titanium oxide.” *Applied Physics Letters* **92** (2008) 221501.
- [6] G. M. Veith, A. R. Lupini, S. J. Pennycook, A. Villa, L. Prati, and N. J. Dudney, “Magnetron sputtering of gold nanoparticles onto  $\text{WO}_3$  and activated carbon.” *Catalysis Today* **122** (2007) 248–253.
- [7] G. A. T. Eyck, J. J. Senkevich, F. Tang, D. Liu, S. Pimanpang, T. Karaback, G.-C. Wang, T.-M. Lu, C. Jezewski, and W. A. Lanford, “Plasma-assisted atomic layer deposition of palladium.” *Chemical Vapor Deposition* **11** (2005) 60.
- [8] C. Bower, O. Zhou, W. Zhu, D. J. Werder, and S. Jin, “Nucleation and growth of carbon nanotubes by microwave plasma chemical vapor deposition.” *Applied Physics Letters* **77** (2000) 2767.
- [9] H.-X. Zhang, J.-P. Ge, and Y.-D. Li, “High-temperature growth of silica sheathed  $\text{Bi}_2\text{S}_3$  semiconductor nanowires.” *Chemical Vapor Deposition* **11** (2005) 147.
- [10] A. S. Arico, P. Bruce, B. Scrosati, J.-M. Tarascon, and W. van Schalkwijk, “Nanostructured materials for advanced energy conversion and storage devices.” *Nature Materials* **4** (2006) 366–377.
- [11] P. Simon and Y. Gogotsi, “Materials for electrochemical capacitors.” *Nature Materials* **7** (2008) 845–854.
- [12] A. Srivastava, O. N. Srivastava, S. Talapatra, R. Vajtai, and P. M. Ajayan, “Carbon nanotube filters.” *Nature Materials* **3** (2004) 610–614.
- [13] C. K. Chan, H. Peng, G. Liu, K. McIlwrath, X. F. Zhang, R. A. Huggins, and Y. Cui, “High-performance lithium battery anodes using silicon nanowires.” *Nature Nanotechnology* **3** (2008) 31–35.

- [14] R. Noufi and K. Zweibel, “High-efficiency CdTe and CIGS thin-film solar cells: Highlights and challenges.” In “2006 IEEE 4th World Conference on Photovoltaic Energy Conversion,” IEEE, 1–4, paper number NREL/CP-520-39894.
- [15] D. S. Sholl and J. K. Johnson, “Making high-flux membranes with carbon nanotubes.” *Science* **312** (2006) 1003–1004.
- [16] C. Chang, D. Okawa, H. Garcia, A. Majumdar, and A. Zettl, “Breakdown of fouriers law in nanotube thermal conductors.” *Physical Review Letters* **101** (2008) 075903.
- [17] J. Berthier and P. Silberzan, *Microfluidics for Biotechnology*. Artech House, Norwood, MA (2006).
- [18] Z. M. Zhang, *Nano/microscale Heat Transfer*. McGraw Hill, London, United Kingdom (2007).
- [19] M. Kaviany, *Heat Transfer Physics*. Cambridge University Press, New York (2008).
- [20] H. J. M. Hanley, *Transport Phenomena in Fluids*. Marcel Dekker, New York (1969).
- [21] R. K. Pathria, *Statistical Mechanics, 2nd Edition*. Elsevier, Great Britain (1996).
- [22] R. B. Bird, W. E. Stewart, and E. N. Lightfoot, *Transport Phenomena*. John Wiley and Sons, USA (1960).
- [23] N. J. Themelis, *Transport and Chemical Rate Phenomena*. Gordon and Breach, Switzerland (1995).
- [24] C. Kittel, *Thermal Physics*. Freeman Press, San Francisco, California (1980).
- [25] F. White, *Viscous Fluid Flow, 3rd Edition*. McGraw-Hill, Boston (2006).
- [26] J. R. Welty, C. E. Wicks, and R. E. Wilson, *Fundamentals of Momentum, Heat and Mass Transfer, 3<sup>rd</sup> Edition*. Wiley and Sons, New York (1984).
- [27] F. White, *Fluid Mechanics, 5th Edition*. McGraw-Hill, Boston (2003).
- [28] M. F. Modest, *Radiative Heat Transfer, 2nd Edition*. Academic Press, San Diego, California (2003).
- [29] G. Chen, *Nanoscale Energy Transfer and Conversion*. Oxford University Press, USA (2005).
- [30] J. Yang, “Theory of thermal conductivity.” In T. M. Tritt (ed.), “Thermal Conductivity: Theory, Properties and Applications,” Kluwer Academic, New York (2004) 1–20.
- [31] K. P. Travis, B. D. Todd, and D. J. Evans, “Departure from Navier-Stokes hydrodynamics in confined liquids.” *Physical Review E* **55** (1997) 4288–4295.
- [32] E. Mamontov, C. J. Burnham, S.-H. Chen, A. P. Moravsky, C.-K. Loong, N. R. de Souza, and A. I. Kolesnikov, “Dynamics of water confined in single- and double-wall carbon nanotubes.” *The Journal of Chemical Physics* **124** (2006) 194703.
- [33] G. Hummer, J. C. Rasaiah, and J. P. Noworyta, “Water conduction through the hydrophobic channel of a carbon nanotube.” *Nature* **414** (2001) 188–190.
- [34] D. P. Sellan, E. S. Landry, J. E. Turney, A. J. H. McGaughey, and C. H. Amon, “Size effects in molecular dynamics thermal conductivity predictions.”, unpublished.
- [35] H. Rafii-Tabar, *Computational Physics of Carbon Nanotubes*. Cambridge University Press, New York (2008).
- [36] R. Saito, G. Dresselhaus, and M. S. Dresselhaus, *Physical Properties of Carbon Nanotubes*. Imperial College Press, London (2003).

- [37] Y. Yun, Z. Dong, V. N. Shanov, A. Bange, W. R. Heineman, H. B. Halsall, L. Conforti, A. Bhattacharya, and M. J. Schulz, “On-line carbon nanotube-based biosensors in microfluidic channels.” *Proceedings of the Society of Photographic Instrumentation Engineers* **6528** (2007) 65280T.
- [38] P. J. F. Harris, *Carbon Nanotube Science*. Cambridge University Press, New York (2009).
- [39] B. Corry, “Designing carbon nanotube membranes for efficient water desalination.” *Journal of Physical Chemistry B* **112** (2008) 1427–1434.
- [40] A. Kalra, S. Garde, and G. Hummer, “Osmotic water transport through carbon nanotube membranes.” *Proceedings of the National Academy of Sciences* **100** (2003) 10175–10180.
- [41] A. M. Stark, “Nanotube membranes offer possibility of cheaper desalination.” *Lawrence Livermore National Laboratory News Release NR-06-05-06* (May 18, 2006).
- [42] V. V. Simonyan and J. K. Johnson, “Hydrogen storage in carbon nanotubes and graphitic nanofibers.” *Journal of Alloys and Compounds* **330-332** (2002) 659–665.
- [43] J. K. Holt, H. G. Park, Y. Wang, M. Stadermann, A. B. Artyukhin, C. P. Grigoropoulos, A. Noy, and O. Bakajin, “Fast mass transport through sub-2-nanometer carbon nanotubes.” *Science* **312** (2006) 1034–1037.
- [44] C. Yu, L. Shi, Z. Yao, D. Li, and A. Majumdar, “Thermal conductance and thermopower of an individual single-wall carbon nanotube.” *Nano Letters* **5** (2005) 1842–1846.
- [45] E. Pop, D. Mann, Q. Wang, K. Goodson, and H. Dai, “Thermal conductance of an individual single-wall carbon nanotube above room temperature.” *Nano Letters* **6** (2006) 96–100.
- [46] T. W. Ebbesen, H. J. Lezec, H. Hiura, J. W. Bennett, H. F. Ghaemi, and T. Thio, “Electrical conductivity of individual carbon nanotubes.” *Nature* **408** (1996) 541–549.
- [47] J. Hu, M. Ouyang, P. Yang, and C. M. Lieber, “Controlled growth and electrical properties of heterojunctions of carbon nanotubes and silicon nanowires.” *Nature* **399** (1999) 48–51.
- [48] M. Biercuk, M. Llaguno, M. Radosavljevic, J. Hyun, A. Johnson, and J. Fischer, “Carbon nanotube composites for thermal management.” *Applied Physics Letters* **80** (2002) 2767–2769.
- [49] S. Sinha, S. Barjam, G. Iannacchione, A. Schwab, and G. Muench, “Off-axis thermal properties of carbon nanotube films.” *Applied Physics Letters* **7** (2005) 651–657.
- [50] G.-D. Zhan, J. D. Kuntz, A. K. Mukherjee, P. Zhu, and K. Koumoto, “Thermoelectric properties of carbon nanotube/ceramic nanocomposites.” *Scripta Materialia* **54** (2006) 77–82.
- [51] F. Yakuphanoglu and B. F. Senkal, “Thermoelectrical and optical properties of double wall carbon nanotubes: polyaniline containing boron n-type organic semiconductors.” *Polymers For Advanced Technologies* **19** (2007) 905908.
- [52] C. Joachim, J. K. Gimzewski, and A. Aviram, “Electronics using hybrid-molecular and mono-molecular devices.” *Nature* **382** (2000) 54–56.
- [53] H. T. Soh, C. F. Quate, A. F. Morpurgo, C. M. Marcus, J. Kong, and H. Dai, “Integrated nanotube circuits: Controlled growth and ohmic contacting of single-walled carbon nanotubes.” *Applied Physics Letters* **75** (1999) 627629.
- [54] S. T. Huxtable, D. G. Cahill, S. Shenogin, L. Xue, R. Ozisik, P. Barone, M. Usrey, M. S. Strano, G. Siddons, M. Shim, and P. Kebinski, “Interfacial heat flow in carbon nanotube suspensions.” *Nature Materials* **2** (2003) 731–734.

- [55] T. J. Bandosz, M. J. Biggs, K. E. Gubbins, Y. Harrori, T. Iijama, K. Kaneko, J. Pikunic, and K. T. Thomson, “Molecular models of porous carbons.” In L. R. Radovic (ed.), “Chemistry and Physics of Carbon,” CRC Press, New York (2003) 41–199.
- [56] G. P. Srivastava, “Lattice thermal conduction mechanisms in solids.” In S. L. Shinde and J. S. Goela (eds.), “High Thermal Conductivity Materials,” Springer, Boca Raton (2006) 1–33.
- [57] X. Zhao and J. K. Johnson, “An effective potential for adsorption of polar molecules on graphite.” *Molecular Simulation* **31** (2005) 1–10.
- [58] A. I. Skouidas and D. S. Sholl, “Direct tests of the darken approximation for molecular diffusion in zeolites using equilibrium molecular dynamics.” *The Journal of Physical Chemistry B* **105** (2001) 3151–3154.
- [59] G. Chen, M. S. Dresselhaus, G. Dresselhaus, J.-P. Fleurial, and T. Caillat, “Recent developments in thermoelectric materials.” *International Materials Reviews* **48** (2003) 45–66.
- [60] T. Fujii, Y. Gao, R. Sharma, E. L. Hu, S. P. DenBaars, and S. Nakamura, “Increase in the extraction efficiency of GaN-based light-emitting diodes via surface roughening.” *Applied Physics Letters* **84** (2004) 855–857.
- [61] J. A. Thomas and A. J. H. McGaughey, “Effect of surface wettability on liquid density, structure, and diffusion near a solid surface.” *Journal of Chemical Physics* **126** (2007) 034707.
- [62] J. A. Thomas and A. J. H. McGaughey, “Density, distribution, and orientation of water molecules inside and outside carbon nanotubes.” *Journal of Chemical Physics* **128** (2008) 084715.
- [63] J. A. Thomas and A. J. H. McGaughey, “Reassessing fast water transport through carbon nanotubes.” *Nano Letters* **9** (2008) 2788–2793.
- [64] J. A. Thomas, A. J. H. McGaughey, and O. Kuter-Arneback, “Pressure-driven water flow through carbon nanotubes: Insights from molecular dynamics simulations.” *International Journal of Thermal Sciences* **49** (2010) 281–289.
- [65] J. A. Thomas and A. J. H. McGaughey, “Water flow in carbon nanotubes: Transition to subcontinuum transport.” *Physical Review Letters* **102** (2009) 184502.
- [66] J. A. Thomas, R. M. Iutzi, and A. J. H. McGaughey, “Thermal conductivity and phonon transport in empty and water-filled carbon nanotubes.” *Physical Review B* **81** (2010) 045413.
- [67] J. A. Thomas, J. E. Turney, R. M. Iutzi, A. J. H. McGaughey, and C. H. Amon, “Predicting phonon properties from the spectral energy density.” *Submitted to Physical Review Letters* (2010) .
- [68] M. P. Allen and D. J. Tildesley, *Computer Simulation of Liquids*. Clarendon Press, Oxford (1987).
- [69] D. C. Rapaport, *The Art of Molecular Dynamics Simulation*. Cambridge University Press, Cambridge (2004).
- [70] F. Jensen, *Introduction to Computational Chemistry*. Wiley and Sons, USA (2006).
- [71] N. Goldman, R. S. Fellers, M. G. Brown, L. B. Braly, C. J. Keoshian, C. Leforestier, and R. J. Saykally, “Spectroscopic determination of the water dimer intermolecular potential-energy surface.” *Journal of Chemical Physics* **116** (2002) 10148–10163.
- [72] F. N. Keutsch and R. J. Saykally, “Water clusters: Untangling the mysteries of the liquid, one molecule at a time.” *Proceedings of the National Academy of Sciences* **98** (2001) 10533–10540.

- [73] M. Masella and J. P. Glament, “A pairwise and two many-body models for water: Influence of nonpairwise effects upon the stability and geometry of  $(\text{H}_2\text{O})_n$  cyclic ( $n=36$ ) and cagelike ( $n=620$ ) clusters.” *Journal of Chemical Physics* **107** (1997) 9105–9116.
- [74] N. Gresh, P. Claverie, and A. Pullman, “Intermolecular interactions: Elaboration on an additive procedure including an explicit charge-transfer contribution.” *International Journal of Quantum Chemistry* **29** (1985) 101–118.
- [75] J. O. Hirschfelder, C. F. Curtiss, and R. B. Bird, *Molecular theory of gases and liquids*. Wiley, New York (1964).
- [76] M. W. Mahoney and W. L. Jorgensen, “A five-site model for liquid water and the reproduction of the density anomaly by rigid, nonpolarizable potential functions.” *Journal of Chemical Physics* **112** (2000) 8910–8922.
- [77] A. DeFusco, D. P. Schofield, and K. D. Jordan, “Comparison of models with distributed polarizable sites for describing water clusters.” *Molecular Physics* **105** (2007) 2681–2696.
- [78] A. Striolo, “The mechanism of water diffusion in narrow carbon nanotubes.” *Nano Letters* **6** (2006) 633–639.
- [79] W. L. Jorgensen, J. Chandrasekhar, J. Madura, R. W. Impey, and M. L. Klein, “Comparison of simple potential functions for simulating liquid water.” *Journal of Chemical Physics* **79** (1983) 926–935.
- [80] W. L. Jorgensen and J. D. Madura, “Temperature and size dependence for Monte Carlo simulations of TIP4P water.” *Molecular Physics* **56** (1985) 1381–1392.
- [81] H. J. C. Berendsen, J. P. M. Postma, W. F. van Gunsteren, J. Hermans, and B. Pullman, *Intermolecular Forces*. Reidel, Dordrecht (1981).
- [82] L. X. Dang and T.-M. Chang, “Molecular dynamics study of water clusters, liquid, and liquid-vapor interface of water with many-body potentials.” *Journal of Chemical Physics* **106** (1997) 8149–8159.
- [83] T. Werder, J. H. Walther, R. L. Jaffe, T. Halicioglu, and P. Koumoutsakos, “On the water-carbon interaction for use in molecular dynamics simulations of graphite and carbon nanotubes.” *Journal of Physical Chemistry B* **107** (2003) 1345–1352.
- [84] A. Pertsina and M. Grunze, “Water as a lubricant for graphite: A computer simulation study.” *Journal of Chemical Physics* **125** (2006) 114707.
- [85] G. Jenness and K. D. Jordan, “A DF-DFT-SAPT investigation of the binding of water of coronene and dodecabenzenocoronene: Implications for the water-graphite interaction.” *Journal of Physical Chemistry C* **113** (2009) 10242–10248.
- [86] J. Tersoff, “Empirical interatomic potential for carbon, with applications to amorphous carbon.” *Physical Review Letters* **61** (1988) 2879–2882.
- [87] D. W. Brenner, O. A. Shenderova, J. A. Harrison, S. J. Stuart, B. Ni, and S. B. Sinnott, “A second-generation reactive empirical bond order (REBO) potential energy expression for hydrocarbons.” *Journal of Physics: Condensed Matter* **14** (2002) 783–802.
- [88] S. Joseph and N. R. Aluru, “Why are carbon nanotubes fast transporters of water?” *Nano Letters* **8** (2008) 452–458.
- [89] J. Shiomi and S. Maruyama, “Water transport inside a single-walled carbon nanotube driven by a temperature gradient.” *Nanotechnology* **20** (2009) 055708.

- [90] M. J. Longhurst and N. Quirke, “Temperature-driven pumping of fluid through single-walled carbon nanotubes.” *Nano Letters* **7** (2007) 3324–3328.
- [91] L. E. Goodman and W. H. Warner, *Dynamics*. Dover, New York (2001).
- [92] F. B. Hildebrand, *Finite-Difference Equations and Simulations*. Prentice-Hall, Englewood Cliffs, New Jersey (1968).
- [93] R. D. Richtmyer and K. W. Morton, *Difference Methods for Initial Value Problems*. Wiley, New York (1967).
- [94] L. Verlet, “Computer ‘experiments’ on classical fluids. i. thermodynamical properties of lennard-jones molecules.” *Physical Review* **159** (1967) 98–103.
- [95] D. Fincham and D. M. Heyes, “Integration algorithms in molecular dynamics.” *CCP5 Quarterly* **6** (1982) 4–10.
- [96] D. Fincham, “How big is a timestep?” *CCP5 Quarterly* **17** (1985) 43–50.
- [97] D. Frenkel and B. Smit, *Understanding Molecular Simulation: From Algorithms to Applications*. Academic Press, Elsevier, San Diego (2002).
- [98] D. M. Heyes, *The Liquid State: Applications of Molecular Simulations*. Wiley and Sons, New York (1998).
- [99] C. J. Fennell and J. D. Gezelter, “Is the Ewald summation still necessary? Pairwise alternatives to the accepted standard for long-range electrostatics.” *Journal of Chemical Physics* **124** (2006) 234104.
- [100] G. Gruner, “Carbon nanotube transistors for biosensing applications.” *Analytical and Bioanalytical Chemistry* **384** (2006) 322335.
- [101] J. Li, C. Papadopoulos, and J. Xu, “Nanoelectronics: Growing y-junction carbon nanotubes.” *Nature* **402** (1999) 253–254.
- [102] A. I. Skouidas, D. M. Ackerman, J. K. Johnson, , and D. S. Sholl, “Rapid transport of gases in carbon nanotubes.” *Physical Review Letters* **89** (2002) 185901.
- [103] A. Noy, H. G. Park, F. Fornasiero, J. K. Holt, C. P. Grigoropoulos, and O. Bakajin, “Nanofluidics in carbon nanotubes.” *Nanotoday* **2** (2001) 22–29.
- [104] M. Shim, N. W. S. Kam, R. J. Chen, Y. Li, and H. Dai, “Functionalization of carbon nanotubes for biocompatibility and biomolecular recognition.” *Nano Letters* **2** (2002) 285–288.
- [105] J. Martí and M. C. Gordillo, “Temperature effects on the static and dynamic properties of liquid water inside nanotubes.” *Physical Review E* **64** (2001) 021504.
- [106] K. Koga and H. Tanaka, “Phase diagram of water between hydrophobic surfaces.” *Journal of Chemical Physics* **122** (2005) 104711.
- [107] J. H. Walther, R. Jaffe, T. Halicioglu, and P. Koumoutsakos, “Carbon nanotubes in water: Structural characteristics and energetics.” *J. Phys. Chem. B* **105** (2001) 9980–9987.
- [108] N. Choudhury, “Dynamics of water in solvation shells and intersolute regions of C60: A molecular dynamics simulation study.” *Journal of Physical Chemistry C* **111** (2007) 2565–2572.
- [109] E. M. Kotsalis, J. H. Walther, and P. Koumoutsakos, “Multiphase water flow inside carbon nanotubes.” *International Journal of Multiphase Flow* **30** (2004) 995–1010.

- [110] I. Hanasaki and A. Nakatani, “Flow structure of water in carbon nanotubes: Poiseuille type or plug-like?” *Journal of Chemical Physics* **124** (2006) 144708.
- [111] M. Lisal, J. Kolafa, and I. Nezbeda, “An examination of the five-site potential (TIP5P) for water.” *Journal of Chemical Physics* **117** (2002) 8892–8897.
- [112] D. J. Griffiths, *Introduction to Electrodynamics, 3rd Edition*. Prentice Hall, New Jersey (1999).
- [113] M. W. Mahoney and W. L. Jorgensen, “Diffusion constant of the TIP5P model of liquid water.” *Journal of Chemical Physics* **114** (2001) 363–366.
- [114] W. L. Jorgensen and J. Tirado-Rives, “Potential energy functions for atomic-level simulations of water and organic and biomolecular systems.” *Proceedings of the National Academy of Sciences of the United States of America* **102** (2005) 6665–6670.
- [115] A. H. Barber, S. R. Cohen, and H. D. Wagner, “External and internal wetting of carbon nanotubes with organic liquids.” *Physical Review B* **71** (2005) 115443.
- [116] R. L. Jaffe, P. Gonnet, T. Werder, J. H. Walther, and P. Koumoutsakos, “Water-carbon interactions 2: Calibration of potentials using contact angle data for different interaction models.” *Molecular Simulation* **30** (2004) 205–216.
- [117] F. Moulin, M. Devel, and S. Picaud, “Molecular dynamics simulations of polarizable nanotubes interaction with water.” *Physical Review B* **71** (2005) 165401.
- [118] G. Nagy, “Water structure at the graphite(0001) surface by stm measurements.” *Journal of Electroanalytical Chemistry* **409** (1996) 19–23.
- [119] D. Feller and K. D. Jordan, “Estimating the strength of the water/single-layer graphite interaction.” *Journal of Physical Chemistry A* **104** (2000) 9971–9975.
- [120] R. F. Hainsey, R. Gangwar, J. D. Shindler, and R. M. Suter, “Reentrant disordered phase in two-layer films of kr on graphite.” *Physical Review B* **44** (1991) 3365–3368.
- [121] M. Ashino, A. Schwarz, T. Behnke, and R. Wiesendanger, “Atomic-resolution dynamic force microscopy and spectroscopy of a single-walled carbon nanotube: Characterization of interatomic van derwaals forces.” *Physical Review Letters* **93** (2004) 136101.
- [122] M. Whitby, L. Cagnon, M. Thanou, and N. Quirke, “Enhanced fluid flow through nanoscale carbon pipes.” *Nano Letters* **8** (2008) 2632–2637.
- [123] M. Majumder, N. Chopra, R. Andrews, and B. J. Hinds, “Nanoscale hydrodynamics: Enhanced flow in carbon nanotubes.” *Nature* **438** (2005) 44.
- [124] T. Yamada, T. Namai, K. Hata, D. N. Futaba, K. Mizuno, J. Fan, M. Yudasaka, M. Yumura, and S. Iigima, “Size-selective growth of double-walled carbon nanotube forests from engineered iron catalysts.” *Nature Nanotechnology* **1** (2006) 131–136.
- [125] M. Whitby and N. Quirke, “Fluid flow in carbon nanotubes and nanopipes.” *Nature Nanotechnology* **2** (2007) 87–94.
- [126] S. Sinha, M. P. Rossi, D. Mattia, Y. Gogotsi, and H. H. Bau, “Induction and measurement of minute flow rates through nanopipes.” *Physics of Fluids* **19** (2007) 013603.
- [127] M. G. Schrlau, N. J. Dun, and H. H. Bau, “Cell electrophysiology with carbon nanopipettes.” *ACS Nano* **3** (2009) 563–568.
- [128] A. I. Skoulidas, D. S. Sholl, and J. K. Johnson, “Adsorption and diffusion of carbon dioxide and nitrogen through single-walled carbon nanotube membranes.” *Journal of Chemical Physics* **124** (2006) 054708.

- [129] H. Verweij, M. C. Schillo, and J. Li, “Fast mass transport through carbon nanotube membranes.” *Small* **3** (2007) 1996–2004.
- [130] V. P. Sokhan, D. Nicholson, and N. Quirke, “Fluid flow in nanopores: Accurate boundary conditions for carbon nanotubes.” *Journal of Chemical Physics* **117** (2002) 8531–8539.
- [131] P. Joseph and P. Tabeling, “Direct measurement of the apparent slip length.” *Physical Review E* **71** (2005) 035303R.
- [132] J.-L. Barrat and F. Chiaruttini, “Kapitza resistance at the liquid-solid interface.” *Molecular Physics* **101** (2003) 1605–1610.
- [133] J. Li, D. Liao, and S. Yip, “Coupling continuum to molecular-dynamics simulation: Reflecting particle method and the field estimator.” *Physical Review E* **57** (1998) 7259–7267.
- [134] S. C. Kassinos, J. H. Walther, E. M. Kotsalis, and P. Koumoutsakos, “Flow of aqueous solutions in carbon nanotubes.” In S. Attinger and P. Koumoutsakos (eds.), “Multiscale Modelling and Simulation,” Springer (2004) 220–224.
- [135] J. S. Hansen, P. J. Daivis, K. P. Travis, and B. D. Todd, “Parameterization of the nonlocal viscosity kernel for an atomic fluid.” *Physical Review E* **76** (2007) 041121.
- [136] T. Ohara and D. Suzuki, “Intermolecular momentum transfer in a simple liquid and its contribution to shear viscosity.” *Microscale Thermophysical Engineering* **5** (2001) 117–130.
- [137] S. S. Ray, P. Chando, and A. L. Yarin, “Enhanced release of liquid from carbon nanotubes due to entrainment by an air layer.” *Nanotechnology* **20** (2009) 095711.
- [138] B. J. Hinds, N. Chopra, T. Rantell, R. Andrews, V. Gavalas, and L. G. Bachas, “Aligned multiwalled carbon nanotube membranes.” *Science* **303** (2004) 62–65.
- [139] P. Koumoutsakos, R. L. Jaffe, T. Werder, and J. H. Walther, “On the validity of the no-slip condition in nanofluidics.” *Nanotech* **1** (2003) 148–151.
- [140] D. A. McQuarrie, *Statistical Mechanics*. Viva Books Private Limited, New Delhi (2005).
- [141] S. Yongli, S. Minhua, C. Weidong, M. Congxiao, and L. Fang, “The examination of water potentials by simulating viscosity.” *Computational Materials Science* **38** (2007) 737–740.
- [142] Y. A. Cengel and J. M. Cimbala, *Fluid Mechanics: Fundamentals and Applications*. McGraw-Hill, Boston (2006).
- [143] L. A. Pozhar, “Structure and dynamics of nanofluids: Theory and simulations to calculate viscosity.” *Physical Review E* **61** (2000) 1432–1446.
- [144] J. Petracic and P. Harrowell, “On the equilibrium calculation of the friction coefficient for liquid slip against a wall.” *Journal of Chemical Physics* **127** (2007) 174706.
- [145] J. Petracic and P. Harrowell, “Erratum: On the equilibrium calculation of the friction coefficient for liquid slip against a wall.” *Journal of Chemical Physics* **128** (2008) 209901.
- [146] S. Lichter, A. Martini, R. Q. Snurr, and Q. Wang, “Liquid slip in nanoscale channels as a rate process.” *Physical Review Letters* **98** (2007) 226001.
- [147] E. S. Landry, S. Mikkilineni, M. Paharia, and A. J. H. McGaughey, “Droplet evaporation: A molecular dynamics investigation.” *Journal of Applied Physics* **102** (2007) 124301.
- [148] F. Fornasiero, H. G. Park, J. K. Holt, M. Stadermann, C. P. Grigoropoulos, A. Noy, and O. Bakajin, “Ion exclusion by sub-2-nm carbon nanotube pores.” *Proceedings of the National Academy of Sciences* **45** (2008) 17250–17255.

- [149] D. Mattia, M. P. Rossi, B. M. Kim, G. Korneva, H. H. Bau, and Y. Gogotsi, “Effect of graphitization on the wettability and electrical conductivity of CVD-carbon nanotubes and films.” *Journal of Chemical Physics B* **110** (2006) 9850–9855.
- [150] P. Joseph, C. Cottin-Bizonne, J.-M. Benoit, C. Ybert, C. Journet, P. Tabeling, and L. Bocquet, “Slippage of water past superhydrophobic carbon nanotube forests in microchannels.” *Physical Review Letters* **97** (2006) 156104.
- [151] J. Bear, *Dynamics of Fluids in Porous Media*. American Elsevier, New York (1972).
- [152] S. Joseph and N. R. Aluru, “Pumping of confined water in carbon nanotubes by rotation-translation coupling.” *Physical Review Letters* **101** (2008) 064502.
- [153] K. Koga, G. T. Gao, H. Tanaka, and X. C. Zeng, “Formation of ordered ice nanotubes inside carbon nanotubes.” *Nature* **412** (2001) 802–805.
- [154] A. Alexiadis and S. Kassinos, “Molecular simulation of water in carbon nanotubes.” *Chemical Reviews* **108** (2008) 5014–5034.
- [155] A. Kolesnikov, C.-K. Loong, N. de Souza, C. Burnham, and A. P. Moravsky, “Anomalously soft dynamics of water in carbon nanotubes.” *Physica B* **385–386** (2006) 272–274.
- [156] J. Kofinger, G. Hummer, and C. Dellago, “Macroscopically ordered water in nanopores.” *Proceedings of the National Academy of Sciences* **105** (2008) 13218.
- [157] J. Hone, M. C. Llaguno, N. M. Nemes, and A. T. Johnson, “Electrical and thermal transport properties of magnetically aligned single wall carbon nanotube films.” *Applied Physics Letters* **77** (2000) 666–668.
- [158] J. Hone, M. Whitney, C. Piskoti, and A. Zettl, “Thermal conductivity of single-walled carbon nanotubes.” *Physical Review B* **59** (1999) R2514–R2516.
- [159] D. Donadio and G. Galli, “Thermal conductivity of isolated and interacting carbon nanotubes: Comparing results from molecular dynamics and the Boltzmann transport equation.” *Physical Review Letters* **99** (2007) 255502.
- [160] J. F. Moreland, J. B. Freund, and G. Chen, “The disparate thermal conductivity of carbon nanotubes and diamond nanowires studied by atomistic simulation.” *Microscale Thermophysical Engineering* **8** (2004) 61–69.
- [161] J. Shiomi and S. Maruyama, “Non-Fourier heat conduction in a single-walled carbon nanotube: Classical molecular dynamics simulations.” *Physical Review B* **73** (2006) 205420.
- [162] S. Maruyama, “A molecular dynamics simulation of heat condition of a finite length single-walled carbon nanotube.” *Microscale Thermophysical Engineering* **7** (2003) 41–50.
- [163] S. Shenogin, A. Bodapati, L. Xue, R. Ozisik, and P. Keblinski, “Effect of chemical functionalization on thermal transport of carbon nanotube composites.” *Applied Physics Letters* **85** (2004) 2229–2231.
- [164] S. Shenogin, L. Xue, R. Ozisik, P. Keblinski, and D. G. Cahill, “Role of thermal boundary resistance on the heat flow in carbon-nanotube composites.” *Journal of Applied Physics* **95** (2004) 8136–8144.
- [165] S. Shenogin, P. Keblinski, D. Bedrov, and G. D. Smith, “Thermal relaxation mechanism and role of chemical functionalization in fullerene solutions.” *Journal of Chemical Physics* **124** (2006) 014702.

- [166] J. Hone, “Carbon nanotubes: Thermal properties.” In J. A. Schwarz, C. I. Contescu, and K. Putyera (eds.), “Dekker Encyclopedia of Nanoscience and Nanotechnology,” Marcel Dekker, New York (2004) 603–610.
- [167] L. X. Benedict, S. G. Louie, and M. L. Cohen, “Heat capacity of carbon nanotubes.” *Solid State Communications* **100** (1996) 177–180.
- [168] N. Mingo and D. A. Broido, “Length dependence of carbon nanotube thermal conductivity and the ‘problem of long waves’.” *Nano Letters* **5** (2005) 1221–1225.
- [169] N. Mingo and D. A. Broido, “Carbon nanotube ballistic thermal conductance and its limits.” *Physical Review Letters* **95** (2005) 096105.
- [170] P. Heino, “Simulations of nanoscale thermal conduction.” *Microsystem Technologies* **15** (2009) 75–81.
- [171] J. Shiomi and S. Maruyama, “Diffusive-ballistic heat conduction of carbon nanotubes and nanographene ribbons.” *Japanese Journal of Applied Physics* **47** (2008) 2005–2009.
- [172] J. R. Lukes and H. Zhong, “Thermal conductivity of individual single-wall carbon nanotubes.” *Journal of Heat Transfer* **129** (2007) 705–716.
- [173] C. W. Padgett and D. W. Brenner, “Influence of chemisorption on the thermal conductivity of single-wall carbon nanotubes.” *Nano Letters* **4** (2004) 1051–1053.
- [174] J. Hu, X. Ruan, and Y. P. Chen, “Thermal conductivity and thermal rectification in graphene nanoribbons: A molecular dynamics study.” *Nano Letters* **9** (2009) 2730–2735.
- [175] J. L. F. Abascal and C. Vega, “A general purpose model for the condensed phases of water: TIP4P/2005.” *Journal of Chemical Physics* **123** (2005) 234505.
- [176] D. Wolf, P. Kebinski, S. R. Phillpot, and J. Eggebrecht, “Exact method for the simulation of coulombic system by direct, pairwise 1/r summation.” *Journal of Chemical Physics* **110** (1999) 8254.
- [177] C. F. F. Karney, “Quaternions in molecular modeling.” *Journal of Molecular Graphics and Modeling* **25** (2007) 595–604.
- [178] A. K. Soper, “Orientational correlation function for molecular liquids: The case of liquid water.” *Journal of Chemical Physics* **101** (1994) 6888–6901.
- [179] T. Ikeshoji and B. Hafskjold, “Non-equilibrium molecular dynamics calculation of heat conduction in liquid and through liquid-gas interface.” *Molecular Physics* **81** (1994) 251–261.
- [180] E. S. Landry, M. I. Hussein, and A. J. H. McGaughey, “Complex superlattice unit cell designs for reduced thermal conductivity.” *Physical Review B* **77** (2008) 184302.
- [181] P. K. Schelling, S. R. Phillpot, and P. Kebinski, “Comparison of atomic-level simulation methods for computing thermal conductivity.” *Physical Review B* **65** (2002) 144306.
- [182] J. M. Ziman, *Electrons and Phonons: The Theory of Transport Phenomena in Solids*. Clarendon Press, Oxford (1960).
- [183] N. W. Ashcroft and N. D. Mermin, *Solid State Physics*. Saunders, Fort Worth (1976).
- [184] Y. Chen, D. Li, J. R. Lukes, Z. Ni, and M. Chen, “Minimum superlattice thermal conductivity from molecular dynamics.” *Physical Review B* **72** (2005) 174302.
- [185] A. A. Maradudin and A. E. Fein, “Scattering of neutrons by an anharmonic crystal.” *Physical Review* **128** (1962) 2589–2608.

- [186] G. P. Srivastava, “Phonon conductivity of insulators and semiconductors.” *Journal of Physics and Chemistry of Solids* **41** (1980) 357–368.
- [187] L. Lindsay, D. A. Broido, and N. Mingo, “Lattice thermal conductivity of single-walled carbon nanotubes: Beyond the relaxation time approximation and phonon-phonon scattering selection rules.” *Physical Review B* **80** (2009) 125407.
- [188] A. A. Balandin, S. Ghosh, W. Bao, I. Calizo, D. Teweldebrhan, F. Miao, and C. N. Lau, “Superior thermal conductivity of single-layer graphene.” *Nano Letters* **8** (2009) 902–907.
- [189] J. Tersoff, “Modeling solid-state chemistry: Interatomic potentials for multicomponent systems.” *Physical Review B* **39** (1989) 5566–5568.
- [190] J. E. Turney, *Predicting Phonon Properties using Anharmonic Lattice Dynamics*. PhD Thesis, Carnegie Mellon University, Pittsburgh, PA (2009).
- [191] J. A. Thomas, R. M. Iutzi, and A. J. H. McGaughey, “Thermal conductivity of a water/carbon nanotube composite systems: Insights from molecular dynamics simulations.” In “Proceedings of SHTC 2009,” ASME, 1–4.
- [192] W. Evans, J. Fish, and P. Kebinski, “Thermal conductivity of ordered molecular water.” *Journal of Chemical Physics* **126** (2007) 154504.
- [193] M. T. Dove, *Introduction to Lattice Dynamics*. Cambridge University Press, Cambridge (1993).
- [194] C. F. Carlborg, J. Shiomi, and S. Maruyama, “Thermal boundary resistance between single-walled carbon nanotubes and surrounding matrices.” *Physical Review B* **78** (2008) 205406.
- [195] A. Debernardi, S. Baroni, and E. Molinari, “Anharmonic phonon lifetimes in semiconductors from density-functional perturbation theory.” *Physical Review Letters* **75** (1995) 1819–1822.
- [196] J. E. Turney, E. S. Landry, A. J. H. McGaughey, and C. H. Amon, “Predicting phonon properties and thermal conductivity from anharmonic lattice dynamics calculations and molecular dynamics simulations.” *Physical Review B* **79** (2009) 064301.
- [197] C. Z. Wang, C. T. Chan, and K. M. Ho, “Tight-binding molecular-dynamics study of phonon anharmonic effects in silicon and diamond.” *Physical Review B* **42** (1990) 1127611283.
- [198] N. de Koker, “Thermal conductivity of MgO periclase from equilibrium first principles molecular dynamics.” *Physical Review Letters* **103** (2009) 125902.
- [199] W. Rudin, *Real and Complex Analysis*. McGraw-Hill, New York (1987).
- [200] M. Whitby, L. Cagnon, M. Thanou, and N. Quirke, “Addition/correction: Enhanced fluid flow through nanoscale carbon pipes.” *Nano Letters* **9** (2009) 2802.
- [201] <http://www.un.org/millenniumgoals>.
- [202] N. Rozanova and J. Z. Zhang, “Metal and magnetic nanostructures for cancer detection, imaging, and therapy.” *Journal of Biomedical Nanotechnology* **4** (2008) 377–399.
- [203] D. Sarker, “Engineering of nanoemulsions for drug delivery.” *Current Drug Delivery* **2** (2005) 297–310.
- [204] A. Zabet-Khosousi and A.-A. Dhirani, “Charge transport in nanoparticle assemblies.” *Chemical Reviews* **108** (2008) 40724124.
- [205] D. G. Cahill, W. K. Ford, K. E. Goodson, G. D. Mahan, A. Majumdar, H. J. Maris, R. Merlin, and S. R. Phillpot, “Nanoscale thermal transport.” *Journal of Applied Physics* **93** (2003) 793–818.

- [206] P. Y. Papalambros and D. J. Wilde, *Principles of Optimal Design, Second Edition*. Cambridge Press, New York, New York (2000).
- [207] I. Sondi and B. Salopek-Sondi, “Silver nanoparticles as antimicrobial agent: a case study on e. coli as a model for gram-negative bacteria.” *Journal of Colloid and Interface Science* **275** (2004) 177–182.
- [208] G. Oberdorster, V. Stone, and K. Donaldson, “Toxicology of nanoparticles: A historical perspective.” *Nanotoxicology* **1** (2007) 2–25.
- [209] G. C. Abell, “Empirical chemical pseudopotential theory of molecular and metallic bounding.” *Physical Review B* **31** (1965) 6184–6196.
- [210] A. Pytel and J. Kiusalaas, *Engineering Mechanics: Dynamics*. Brooks/Cole Publishing Company, Pacific Grove, CA, USA (1999).
- [211] H. Goldstein, *Classical Mechanics, Second Edition*. Addison-Wesley Press, Reading, Massachusetts (1980).
- [212] H. Anton, *Elementary Linear Algebra*. Wiley, New York (2000).
- [213] A. MacFarlane, *Vector analysis and Quaternions*. Wiley and Sons, New York, New York (1906).
- [214] M. Yoneya, H. J. C. Berendsen, and K. Hirasawa, “A non-iterative matrix method for constraint molecular dynamics simulations.” *Molecular Simulation* **13** (1994) 395–405.
- [215] H. C. Andersen, “Rattle: A velocity version of the shake algorithm for molecular dynamics calculations.” *Journal of Computational Physics* **52** (1982) 24–34.
- [216] A. J. C. Ladd, B. Moran, and W. G. Hoover, “Lattice thermal conductivity: A comparison of molecular dynamics and anharmonic lattice dynamics.” *Physical Review B* **34** (1986) 5058–5064.